Regulation of microtubule nucleation and attachment to spindle pole bodies

Kimberly K. Fong

A dissertation

submitted in partial fulfillment of the

requirements for the degree of

Doctor of Philosophy

University of Washington

2016

Reading Committee:

Trisha N. Davis, Chair

James B. Hurley

Justin M. Kollman

Program Authorized to Offer Degree:

Biochemistry

University of Washington

Abstract

Regulation of microtubule nucleation and attachment to spindle pole bodies

Kimberly K. Fong

Chair of the Supervisory Committee:

Trisha N. Davis, Professor and Chair

Department of Biochemistry

The precise regulation and coordination of the mitotic spindle is vital for accurate chromosomal segregation within a dividing cell. The centrosome is the microtubule organizing center of the cell, responsible for nucleating and organizing the microtubules of the mitotic spindle. In yeast, the centrosome functional equivalent is called the spindle pole body. The studies presented here aimed to understand how microtubules are nucleated at the spindle pole body and also studied the regulation and mechanical strength of the yeast spindle pole body *in vitro*.

In yeast, the γ-tubulin small complex, a highly conserved heterotetramer essential for microtubule nucleation, is composed of two copies of Tub4, and one copy each of Spc97 and Spc98. In this study, a comprehensive mutagenesis technique coupled with high-throughput sequencing was used to identify regions of Spc97 and Spc98 that were essential for the formation of the γ-tubulin small complex and mutations that influenced the organization of the mitotic spindle. Regions essential for structure and function of the complex were mapped onto the

protein sequence for both Spc97 and Spc98 and temperature sensitive mutants identified by the mutagenic screen were isolated and their unique nucleation phenotypes characterized.

Improvements were made to historical spindle pole body purification methods to facilitate a variety of *in vitro* biochemical and biophysical assays that had previously been hindered by technological constraints. Higher spindle pole body yields, purity, and reproducibility enabled a re-evaluation of the yeast spindle pole body cell cycle phosphoproteome. High confidence phosphorylation assignments were collected and compared to previously published data sets to reduce the ambiguity in the phosphoproteome data set while also expanding the data set to analyze the novel phosphorylation profile of the spindle pole body in G1/S. *In vivo* characterization of the high confidence phosphorylation sites revealed a combination of phosphorylation events in Spc97 that were essential for cell viability.

The adaptability of the spindle pole body purification methods also allowed for the purification of genetic mutants of the spindle pole body, which were studied by biophysical assays. The strength of the microtubule attachment to the spindle pole body was probed by a laser trapping technique to determine how mutations in spindle pole body component Spc110 affected the physical integrity of the spindle pole body. It was shown that mutations in Spc110 decreased the force at which the microtubule was pulled from the spindle pole body, providing mechanical evidence for *in vivo* phenotypes of mitotic spindle failure. Together, these experiments interrogated several aspects of the yeast spindle pole body *in vivo* and *in vitro* to better understand the requirements for and regulation of microtubule nucleation.

TABLE OF CONTENTS

LIST OF FIGURES

LIST OF TABLES

ACKNOWLEDGEMENTS

I would like to thank Trisha Davis for her guidance and mentorship during my time in graduate school. Her support and confidence in me enabled me to branch out and develop as a scientist versed in a diversity of techniques. I thank Trisha Davis, Jim Hurley, Justin Kollman, Dana Miller, and Linda Wordeman for serving on my supervisory committee and Trisha Davis, Jim Hurley, and Justin Kollman for providing feedback on my thesis dissertation. I am grateful to all of the members of the Davis lab, past and present, especially Beth Graczyk, Jerry Tien, and Alex Zelter, who contributed significantly to this work. I also thank Eric Muller, Megan Wargacki, Dan Gestaut, Neil Umbreit, Mike Riffle, Elliott Davidson, and Emily Kudalkar for insightful discussions and helpful advice throughout my time in the Davis lab. I was fortunate to be involved in many strong collaborations and would like to thank members of David Agard's lab, especially Justin Kollman and Michelle Moritz, for our longstanding collaboration studying the yeast γ-tubulin small complex, members of Mark Winey's lab, especially Shelly Jones, for assistance with the yeast phosphoproteome, and members of Chip Asbury's lab, especially Erik Yusko, Krishna Sarangapani, and Yi Deng for collaboration on the laser trap experiments.

Chapter 1
Introduction

Mitosis and the mitotic spindle

In the 1880s, Walther Flemming coined the term "mitosis", stemming from the Greek word for "thread", to describe the cellular phenomenon of chromosome segregation (Flemming, 1882). Since those early observations of condensed chromosomes in live cells, we have come to understand mitosis as a fundamental and highly conserved process by which cells evenly divide their genetic material during the cell cycle. The mitotic spindle is the macromolecular machine responsible for the accurate segregation of chromosomes. Proper organization and regulation of the mitotic spindle is imperative for precise chromosomal movement. Missegregation of genetic material results in aneuploidy, a cellular condition defined by an abnormal number of chromosomes. Aneuploidy has been associated with several diseases, including developmental diseases, neurodegenerative diseases, and cancer (Chi and Jeang, 2007; Torres *et al.*, 2008; Hanahan and Weinberg, 2011; Holland and Cleveland, 2012). Therefore, the regulation of the spindle and the strict fidelity of the mitotic process is required for organized cell division and genetic stability in daughter cells.

The mitotic spindle is comprised of centrosomes, kinetochores, microtubules, and microtubule associated proteins (Figure 1.1). The centrosome is the primary microtubule-organizing center in all eukaryotic cells, organizing microtubules during interphase and establishing the bipolar spindle during mitosis. Kinetochores attach the centromeres of chromosomes to the ends of microtubules and transmit the microtubule dynamics into chromosomal movement. The microtubules make up the bulk of the mitotic structure and carry

out several functions: kinetochore microtubules attach to the chromosomes, interpolar microtubules stabilize the spindle structure through an interdigitated antiparallel array, and astral microtubules interact with the cell cortex to position the spindle within the dividing cell. Various crosslinking proteins and motors associate with the microtubule network and assist in carrying out the spindle's function (Jacobs *et al.*, 1988; Page and Haven, 1992; Gonen *et al.*, 2012; Winey and Bloom, 2012; Biggins, 2013).

Several kinases are responsible for cell cycle-specific regulation of the mitotic spindle. Mps1, Aurora A, and Cdc28 phosphorylate spindle proteins and affect the function of the mitotic spindle (Winey *et al.*, 1991; Deshaies and Ferrell Jr., 2001; Haase *et al.*, 2001; Castillo *et al.*, 2002; Dutertre *et al.*, 2004; Kinoshita *et al.*, 2005). Phosphorylation events have been identified and characterized in several of the yeast centrosome components, including Tub4 (Vogel *et al.*, 2001; Keck *et al.*, 2011; Lin *et al.*, 2011), Spc42 (Donaldson and Kilmartin, 1996), Spc98 (Pereira *et al.*, 1998), and Spc110 (Friedman *et al.*, 1996, 2001; Stirling and Stark, 1996; Huisman *et al.*, 2007), and have demonstrated effects on cell cycle progression. It is evident that phosphoregulation of the spindle components plays a key role in the accuracy of chromosome division and warrants investigation at the poles.

The yeast spindle pole body

The budding yeast *Saccharomyces cerevisiae* serves as an attractive model organism for the study of mitosis due to its genetic tractability and the simplicity of its mitotic spindle. In yeast, the centrosomal equivalent is called the spindle pole body (SPB). While morphologically distinct from mammalian centrosomes, the yeast spindle pole body is comprised of the same

proteins and carries out the same functions as its higher eukaryotic counterpart (Kilmartin and Adams, 1984; Jaspersen and Winey, 2004; Kilmartin, 2014).

By electron microscopy, it is known that the yeast spindle pole body is a trilaminar structure embedded in the nuclear membrane throughout the cell cycle (Moens and Rapport, 1971; Byers and Goetsch, 1975; Winey *et al.*, 1995). The central plaque is embedded in the nuclear membrane, making up the core of the spindle pole body. The inner plaque is on the nuclear face of the spindle pole body and nucleates kinetochore and interpolar microtubules and the outer plaque sits on the cytoplasmic face of the spindle pole body, nucleating cytoplasmic microtubules (Figure 1.2). All of the essential centrosomal proteins found in higher eukaryotes are present in the yeast spindle pole body. The spindle pole body is made up of eighteen components, which have been divided into five rough subclasses: the γ-tubulin complex, linker proteins, core and satellite proteins, the half bridge, and membrane anchoring proteins (Rout and Kilmartin, 1990; Sobel and Snyder, 1995; Geissler *et al.*, 1996; Knop *et al.*, 1997; Knop and Schiebel, 1998; Wigge *et al.*, 1998; Adams and Kilmartin, 1999; Jaspersen and Winey, 2004; Keck *et al.*, 2011). Although the gross morphology of the spindle pole body has been observed by electron microscopy and the components of the spindle pole body have been identified and genetically characterized, atomic level structural organization and absolute protein copy numbers have not yet been determined. As a start, FRET measurements have been used to localize the N- and C-termini of core spindle pole body components and give rough estimates of copy number and protein organization (Muller *et al.*, 2005). Ongoing work is trying to obtain higher resolution structural information about the core of the spindle pole body as well as better understand the mechanism of microtubule nucleation.

Budding yeast is a powerful model organism for the study of mitosis, primarily because yeast is a more genetically tractable system and has already provided insights into conserved mechanisms, regardless of a few differences. Aside from the morphological differences of the centrosomes, one difference between yeast and higher eukaryotes is that higher eukaryotic cells undergo open mitosis while yeast cells undergo closed mitosis (Jaspersen and Winey, 2004; Kilmartin, 2014). This means that during mitosis, the mammalian nuclear envelope breaks down and the nuclear and cytoplasmic contents of the cell are no longer compartmentalized. In contrast, the nuclear envelope never breaks down in yeast, keeping the nuclear contents of the cell compartmentalized and distinct from the cytoplasm throughout the cell cycle. Another major difference between higher eukaryotes and yeast mitosis is the number of microtubules present in the mitotic spindle. In higher eukaryotic cells, each chromosome is connected to the mitotic spindle through attachments of dozens of microtubules, collectively called k-fibers (Rieder, 1982, 2005; Booth *et al.*, 2013). In contrast, yeast spindles consist of only twenty nuclear microtubules and two to three cytoplasmic microtubules emanating from each pole. Each of the sixteen chromosomes in yeast are attached to the spindle pole body by a single microtubule and four interpolar microtubules create an antiparallel array and stabilize the spindle length and structure. (Peterson and Ris, 1976; Winey *et al.*, 1995; O'Toole *et al.*, 1997; Maddox *et al.*, 2000). The minimal number of microtubules makes the system much more amenable to studies of microtubule nucleation and regulation of the spindle pole body.

Microtubule nucleation and the gamma tubulin small complex

Microtubules are made up of α- and β-tubulin heterodimers that associate through longitudinal interactions to form protofilaments, with an inherent polarity. The minus ends of

microtubules are anchored to the spindle poles and do not exhibit any dynamics. The plus ends of the microtubules emanate outwards towards the chromosomes or the cell cortex and frequently switch between periods of polymerization and depolymerization in a property referred to as dynamic instability (Mitchison and Kirschner, 1984).

In vitro, microtubules can exist as hollow tubes with twelve to sixteen protofilaments, with fourteen-protofilament structures predominating (McEwen and Edelstein, 1977; Pierson *et al*., 1978; Langford, 1980). However, *in vivo*, it has been noted that microtubules are almost all in a thirteen-protofilament structure (Tilney *et al*., 1973; Pierson *et al*., 1978; Scheele *et al*., 1982; Evans *et al*., 1985). This configuration of protofilaments results in a straight "seam" down the microtubule and enables the protofilaments to traverse the microtubule in a straight line, without spiraling. This property is exploited by the microtubule motors that walk in straight line down the microtubule (Kikkawa *et al.*, 1994; Metoz *et al.*, 1997; Nogales and Zhang, 2016). The observation of thirteen-protofilament microtubules and the biological relevance of this structure *in vivo* suggest that cells possess a regulatory mechanism that favors the nucleation of thirteen-protofilament microtubules that is missing from *in vitro* nucleation assays.

A kinetic curve illustrates the different stages of microtubule kinetics. The curve begins with an initial lag phase in which nuclei are spontaneously formed until they reach the concentration that leads to exponential growth of microtubules. In the presence of a nucleator, the curve shifts leftward, reducing the lag phase before exponential growth and elongation (Jackson and Berkowitz, 1980; Voter and Erickson, 1984; Bayley *et al.*, 1986; Hyman and Karsenti, 1998; Wieczorek *et al.*, 2015).

In the 1980s and 1990s, such a nucleator was found in γ-tubulin (Tub4 in yeast) (Oakley and Oakley, 1989; Oakley *et al.*, 1990; Stearns *et al.*, 1991; Joshi *et al.*, 1992; Sobel and Snyder,

1995; Marschall *et al.*, 1996). Gamma-tubulin was discovered to be a member of a highly conserved heterotetramer called the γ-tubulin small complex, which is essential for nucleation (Oakley *et al.*, 1990; Moritz *et al.*, 1995; Zheng *et al.*, 1995; Oegema *et al.*, 1999). In *Saccharomyces cerevisiae*, the γ-tubulin small complex is made up of two Tub4 molecules and one copy each of Spc97 and Spc98 (Geissler *et al.*, 1996; Spang *et al.*, 1996a; Knop *et al.*, 1997; Vinh *et al.*, 2002). The yeast γ-tubulin small complex localizes to both faces of the spindle pole body. The nuclear microtubules are nucleated from γ-tubulin small complexes anchored to the inner plaque of the spindle pole body via interactions with Spc110 (Knop and Schiebel, 1997, 1998; Sundberg and Davis, 1997; Nguyen *et al.*, 1998) and the cytoplasmic microtubules are anchored to the spindle pole body via interactions with Spc72 on the outer plaque of the spindle pole body (Knop and Schiebel, 1998; Souès and Adams, 1998; Usui *et al.*, 2003).

The template model of microtubule nucleation posits that γ-tubulin complexes form a three-start helix where thirteen γ-tubulin molecules make longitudinal contacts with the α-β tubulin dimers and establish the thirteen-fold symmetry of the microtubule. (Erickson, 2000). In support of this model, several studies found that the γ-tubulin was confined to the very end of the microtubule (Keating and Borisy, 2000; Moritz *et al.*, 2000; Wiese and Zheng, 2000). Microtubules emanating from spindle pole bodies were observed by electron microscopy. Close examination showed that the microtubule end proximal to the spindle pole body has a closed appearance. This closed appearance was attributed to a protein structure that capped the microtubule and closely conformed to the shape and dimensions of the microtubule (Byers *et al.*, 1978; Moritz *et al.*, 1995; Keating and Borisy, 2000; Kollman *et al.*, 2015). These pieces of data suggested that the γ-tubulin small complex localized to this protein cap, established a template

for thirteen-protofilament microtubules, anchored the microtubule to the spindle pole body, and controlled the dynamics of the microtubule minus end.

Strong convincing evidence for the template model emerged with the publication of the cryo-electron microscopy structures of the yeast γ-tubulin small complex and of the γ-tubulin ring complexes from several species (Moritz *et al.*, 1995, 2000; Oegema *et al.*, 1999; Kollman *et al.*, 2008, 2010, 2011, 2015; Choy *et al.*, 2009, Figure 1.3). In higher eukaryotes, γ-tubulin small complexes organize into a higher-order ring complex with at least four accessory proteins that create a cap-like structure with dimensions similar to the 25 nm diameter of a microtubule (Zheng *et al.*, 1995; Moritz *et al.*, 1998; Oegema *et al.*, 1999). The γ-tubulin small complex alone is sufficient for nucleation in yeast, and it was observed that yeast γ-tubulin small complexes spontaneously oligomerized *in vitro,* forming ring structures similar to those seen in higher eukaryotes (Kollman *et al.*, 2010, 2011). These ring complexes, therefore, are composed of essential microtubule nucleating proteins, localize to sites of microtubule nucleation, and establish thirteen-fold symmetry with dimensions similar to that of a microtubule.

Despite the overwhelming evidence that these γ-tubulin complexes serve as a template for nucleation, *in vitro* assays with purified complexes often failed to reproduce efficient nucleation (Oegema *et al.*, 1999; Vinh *et al.*, 2002; Kollman *et al.*, 2008, 2010). Recombinant yeast γ-tubulin small complexes and γ-tubulin small complexes purified from *Drosophila* only showed a three-fold increase in nucleation over background (Oegema *et al.*, 1999; Vinh *et al.*, 2002). Evidence started to suggest spatial organization, species-specific tubulins, and conformation of the nucleation complex were integral for efficient nucleation. While the *Drosophila* γ-tubulin small complex was a poor nucleator, the *Drosophila* γ-tubulin ring complex was approximately twenty-five times more active, suggesting that the higher order

structure was required for nucleation activity (Oegema *et al.*, 1999). When supplied with bovine brain tubulin, the yeast γ-tubulin small complex ring showed a modest increase in nucleation activity. However, nucleation off the yeast γ-tubulin small complex ring increased approximately 300 fold over background when using tubulin purified from yeast, suggesting that while tubulins are highly conserved, there is a strong effect of species specificity in the nucleation activity of the γ-tubulin small complexes (Kollman *et al.*, 2008, 2010, 2015). By inducing a conformational change in the γ-tubulin small complex ring, locking the ring into a closed conformation, nucleation with yeast tubulin rose to 600 fold above background (Kollman *et al.*, 2015). The profound effect of the induced conformational change suggested that additional regulatory processes required for nucleation *in vivo* had yet to be identified.

The structure of the γ-tubulin small complex was originally solved by cryo-electron microscopy to 8 Å resolution and has since been refined to 6.9 Å resolution (Kollman *et al.*, 2008, 2010, 2015; Choy *et al.*, 2009, Figure 1.3). Crystal structures of the yeast γ-tubulin small complex components have not yet been solved. The closest approximation is the crystal structure of GCP4, which was published at a resolution of 2.3 Å (Guillet *et al.*, 2011). GCP4 is an ancillary protein found in the human γ-tubulin ring complex. In humans, the γ-tubulin small complex is composed of γ-tubulin, GCP2 and GCP3, which are homologs of yeast Tub4, Spc97, and Spc98, respectively. GCP4 is a paralog of Spc97 and Spc98 and associates with the γ-tubulin small complex, but does not have attributed nucleation activity. However, the structure of GCP4 fits well into the electron densities of Spc97 and Spc98, creating a pseudo-atomic model of the yeast γ-tubulin small complex (Guillet *et al.*, 2011).

Close inspection of the γ-tubulin small complex ring provided a possible source for the low nucleation observed *in vitro*. The two γ-tubulin molecules within a γ-tubulin small complex

were slightly wider apart than the lateral interactions of a microtubule. It was hypothesized that a conformational change would bring the γ-tubulin ring into perfect alignment with microtubule geometry and activate the complex for nucleation. Classification of negative stain EM particle reconstruction data suggested that Spc98 may contain a flexible hinge region around which the arm of Spc98 could freely rotate (Kollman *et al.*, 2008). The observed flexibility in the hinge region of Spc98 aligned with the region of predicted flexibility in the GCP4 crystal structure (Figure 1.4). It was hypothesized that this flexibility could be involved in allosteric regulation of the γ-tubulin small complex and might accommodate the movement of γ-tubulin molecules required to form lateral contacts. This hypothesis entertained the possibility that these conformational changes in the γ-tubulin small complex could activate nucleation capacity (Kollman *et al.*, 2011). In an effort to test this hypothesis, the γ-tubulin molecules within a given small complex were crosslinked by the engineering of a disulfide bond, forcing the two molecules close enough to make lateral interactions. This closed state of the γ-tubulin complex ring matched the diameter and pitch of a microtubule exactly and exhibited high nucleation rates *in vitro* (Kollman *et al.*, 2015, Figure 1.4.d). Research in the field continues to search for biologically relevant mechanisms to induce this conformational activation of the γ-tubulin small complex, employing mutational studies, phosphorylation data, and *in vitro* nucleation assays to understand the requirements needed to recapitulate efficient nucleation *in vitro*.

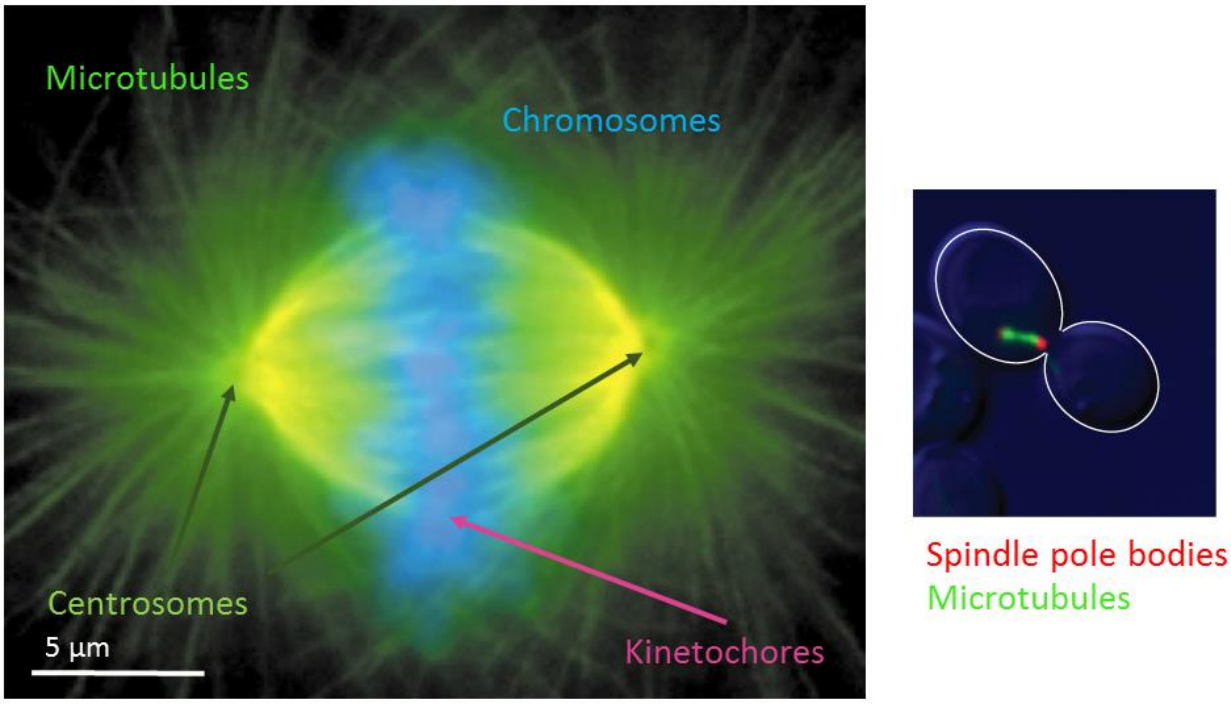

Figure 1.1. The mitotic spindle.
On the left, a mitotic spindle from a tissue-culture cell (Adapted and reprinted with permission from Nature Publishing Group: Nature Cell Biology, Wittmann *et al.*, 2001 ©2001). The centrosomes establish bipolarity and organize the microtubules (shown in green). The microtubules attach to chromosomes through protein complexes called the kinetochore. The chromosomes are shown in blue and TPX2 (a spindle pole component) is shown in red. On the right, a mitotic spindle from yeast, shown to scale. The yeast cell is outlined in white. The spindle pole bodies are labeled with Spc42-mCherry (in red) and the microtubules are labeled with GFP-Tub1 (in green).

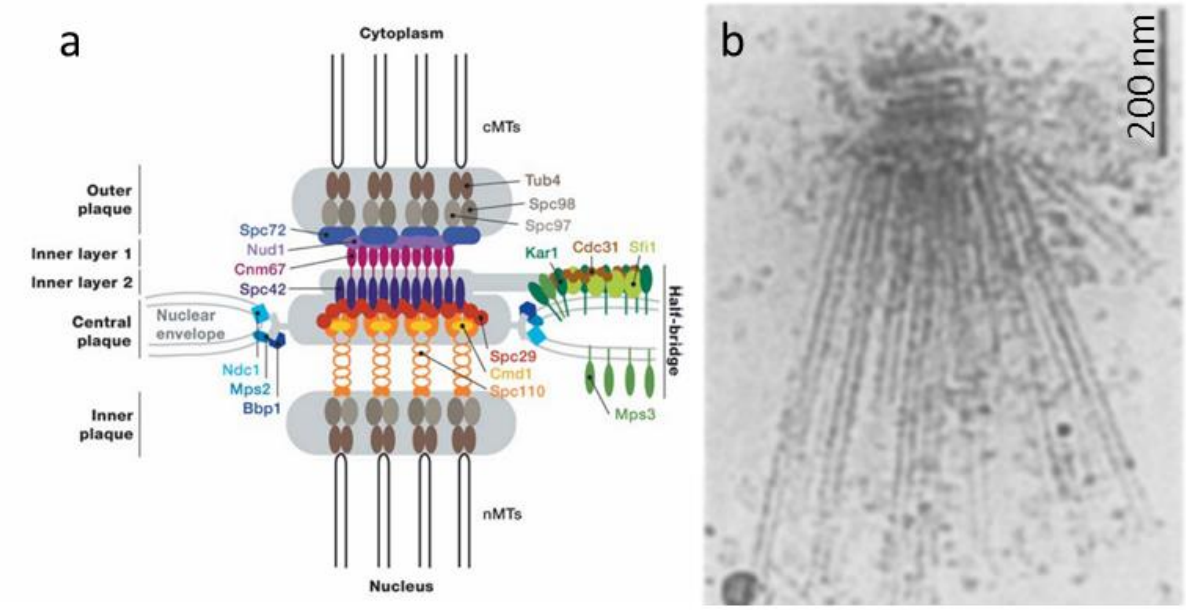

Figure 1.2. The yeast spindle pole body.
a. A schematic illustrating the components of the yeast spindle pole body and general protein organization (From Jaspersen and Winey, 2004). b. Cryo-electron micrograph of purified yeast spindle pole body (From Rout and Kilmartin, 1990).

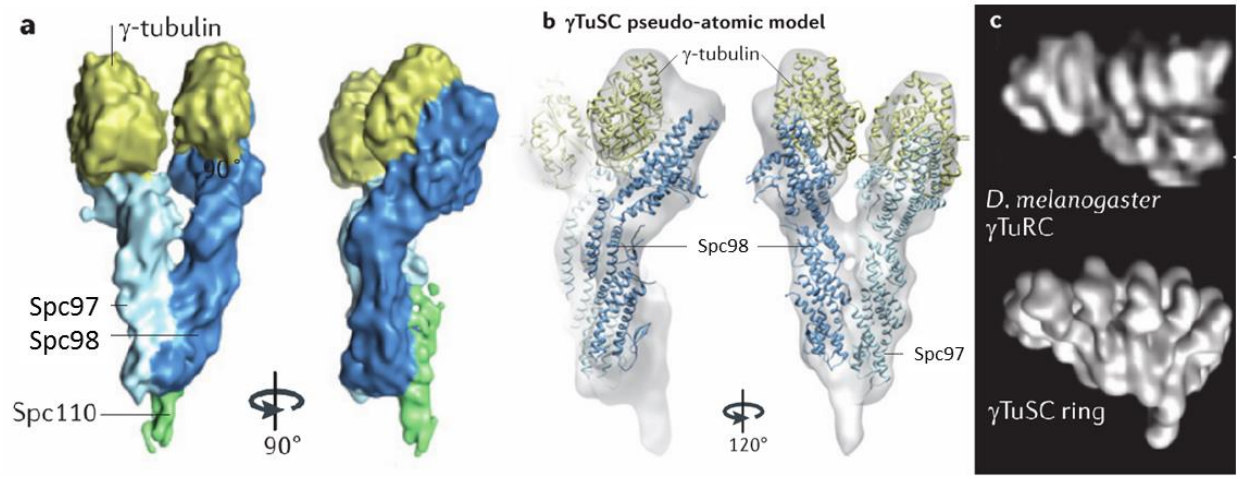

Figure 1.3. The structure of the yeast γ-tubulin small complex and higher order ring. a. An 8 Å electron structure of the yeast γ-tubulin small complex. The approximate boundaries between proteins are indicated by color. b. A pseudo-atomic model of the γ-tubulin small complex. The crystal structure of human GCP4 can be manually fit onto the EM structure of yeast Spc97 and Spc98 in the γ-tubulin small complex. The crystal structure of human γ-tubulin can be fit onto the yeast Tub4 molecules of the γ-tubulin small complex. c. The cryo-electron structure of *Drosophila* γ-tubulin ring complex (top) and the yeast γ-tubulin small complex ring (bottom). (Figure adapted and reprinted with permissions from Nature Publishing Group: Nature Reviews Molecular Cell Biology, Kollman *et al.*, 2011 © 2011).

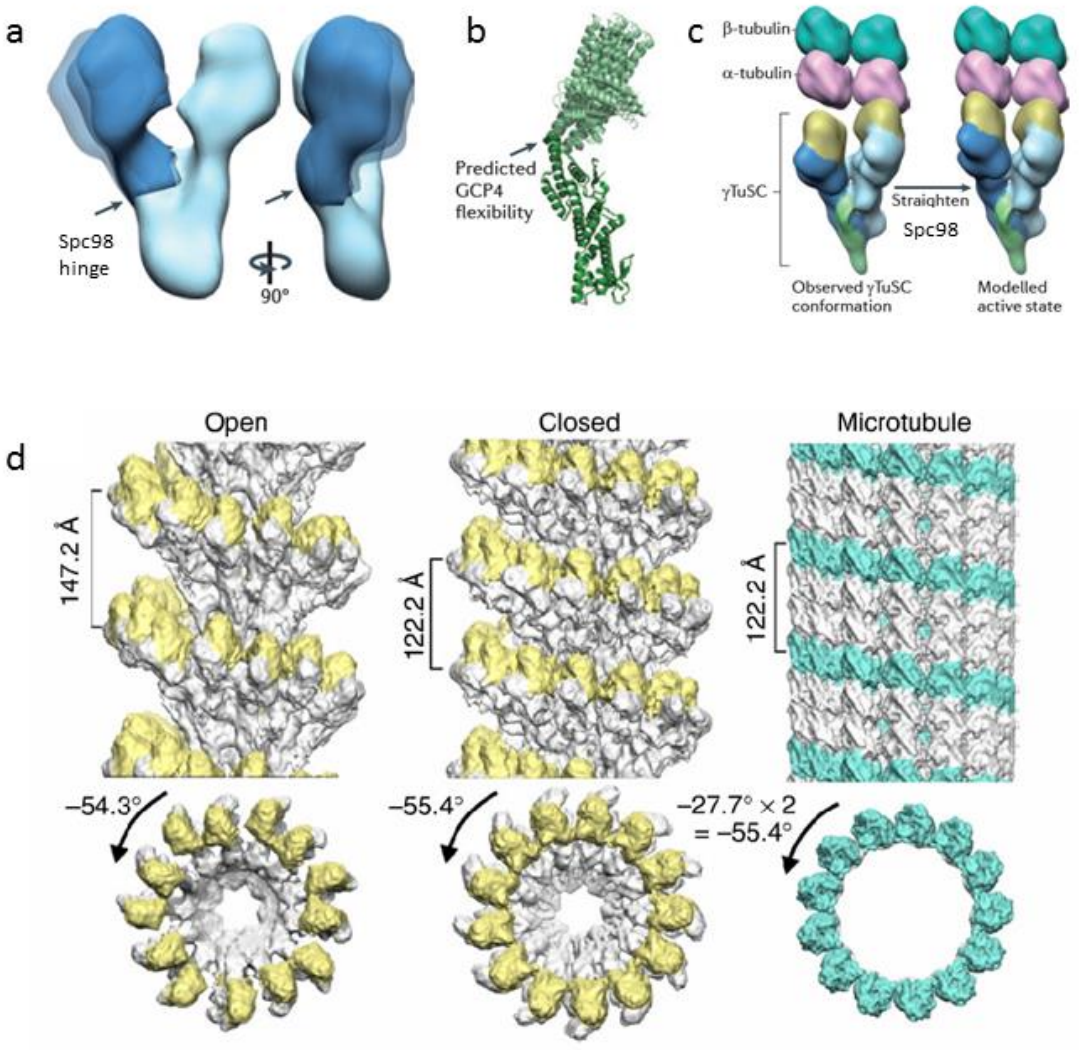

Figure 1.4. Conformational changes activate the γ-tubulin small complex for nucleation. a. Classifications of negative stain electron microscopy particle reconstruction revealed a hinge region in Spc98. b. The GCP4 crystal structure exhibits a region of predicted flexibility that aligns with the hinge region observed in Spc98. c. A model for the activation of the γ-tubulin small complex. A conformational change would straighten Spc98 around the hinge region to bring γ-tubulin molecules into the correct orientation to make contacts with a nucleated microtubule. d. A disulfide bond was engineered into γ-tubulin to lock the γ-tubulin small complex ring in a closed conformation, which has the same dimensions found in a microtubule lattice. (Figure adapted and reprinted with permissions from Nature Publishing Group: Nature Reviews Molecular Cell Biology and Nature Structural & Molecular Biology, from Kollman *et al.*, 2011, 2015 ©2011, 2015).

Chapter 2

Purification of fluorescently labeled *Saccharomyces cerevisiae* spindle pole bodies

Introduction

The mitotic spindle ensures accurate segregation of genetic material in a dividing cell. The centrosome is a crucial component of this macromolecular machine, nucleating and organizing microtubules. Because components of the mitotic spindle are highly conserved throughout eukaryotes, the yeast spindle serves as an excellent model.

In yeast, the centrosome equivalent is the spindle pole body. The spindle pole body is a highly organized laminar structure, consisting of three plaques. The core spindle pole body components form the central plaque, which is embedded in the nuclear envelope throughout the cell cycle (Moens and Rapport, 1971; Byers and Goetsch, 1975). The inner plaque sits on the nuclear side of the central plaque and is the site of nuclear microtubule nucleation. The inner plaque contains the γ -tubulin small complex, which is essential for microtubule nucleation, and Spc110, a linker protein that binds the γ -tubulin small complex to the core of the spindle pole body (Rout and Kilmartin, 1990; Knop and Schiebel, 1997; Nguyen *et al.*, 1998). The outer plaque is on the cytoplasmic side of the central plaque. This structure also contains the γ-tubulin small complex, which is bound to the spindle pole body via interactions with Spc72 (Knop and Schiebel, 1998).

Yeast spindle pole bodies have historically been studied by thin section electron microscopy of yeast cells (Moens and Rapport, 1971; Byers and Goetsch, 1975; Winey *et al.*, 1995) or purified to identify components, determine structure, and examine function of the

spindle pole body *in vitro* (Peterson and Ris, 1976; Byers *et al.*, 1978; Hyams and Borisy, 1978; Rout and Kilmartin, 1990; Bullitt *et al.*, 1997). A method to purify spindle pole bodies out of the lesser characterized yeast *S. uvarum* generated high yields of purified spindle pole bodies, but was limited in the ability to perform genetic analyses and the spindle pole bodies could only be visualized by electron microscopy (Rout and Kilmartin, 1990). More recently, spindle pole bodies were co-purified from *S. cerevisiae* with a TAP-tagged nuclear pore component, Mlp2 (Niepel *et al.*, 2005). Expanding on this method, we discovered that TAP-tagging Spc97, a component of the spindle pole body, increases yield. Adding fluorescent tags to spindle pole body components helps to both visualize the spindle pole bodies and quantify yields. Here we offer a detailed purification protocol for growing, harvesting, and lysing cells to purify spindle pole bodies by TAP-tag purification followed by velocity sedimentation.

Materials

Growing, harvesting, and lysing cells

1. *S. cerevisiae* strain expressing *SPC97-TAP::kanMX* with *SPC42-mCherry::hphMX or S. cerevisiae* strain expressing *SPC97-TAP::kanMX* with *SPC42-mCherry::hphMX* and *TUB4-GFP::kanMX* (Table 2.1)
2. YPD media: 1% yeast extract, 2% peptone, 2% glucose
3. Resuspension buffer: 20 mM sodium-HEPES buffer (pH 7.4), 1.2% polyvinylpyrrolidone (average MW 40,000), 1 mM dithiothreitol, 1 mM phenylmethanesulfonyl fluoride, 4 µg/ml aprotinin, 4 µg/ml chymostatin, 4 µg/ml leupeptin, 4 µg/ml pepstatin, 10 mM sodium fluoride, 1 mM sodium pyrophosphate, 1 mM β-glycerophosphate
4. PM 100 ball mill grinder (Retsch)
5. Stainless steel 125 ml planetary ball mill grinding jar with 20 mm diameter mill grinding balls (Retsch)
6. Liquid nitrogen
7. 18G needle

Spindle pole body purification

1. Extraction Buffer with 300 mM NaCl (EB1 w/ 300 mM NaCl): 20 mM sodium-HEPES buffer (pH 7.4), 300 mM NaCl, 0.5% Triton X-100, 2 mM $MgCl_2$, 100 µM GTP, 1 mM ATP, 1 mM dithiothreitol, 1 mM phenylmethanesulfonyl fluoride, 4 µg/ml aprotinin, 4 µg/ml chymostatin, 4 µg/ml leupeptin, 4 µg/ml pepstatin, 10 mM

sodium fluoride, 1 mM sodium pyrophosphate, 1 mM β-glycerophosphate, 5% glycerol

2. Extraction Buffer with 200 mM NaCl (EB1 w/ 200 mM NaCl): 20 mM sodium-HEPES buffer (pH 7.4), 200 mM NaCl 0.5% Triton X-100, 2 mM $MgCl_2$, 100 µM GTP, 1 mM ATP, 1 mM dithiothreitol, 1 mM phenylmethanesulfonyl fluoride, 4 µg/ml aprotinin, 4 µg/ml chymostatin, 4 µg/ml leupeptin, 4 µg/ml pepstatin, 10 mM sodium fluoride, 1 mM sodium pyrophosphate, 1 mM β-glycerophosphate, 5% glycerol
3. TEV cleavage buffer: 40 mM sodium-HEPES buffer (pH 7.4), 200 mM NaCl, 2 mM $MgCl_2$, 1 mM GTP, 1 mM ATP, 1 mM EDTA (pH 8), 1 mM dithiothreitol, 5% glycerol
4. PCU-2-110 Homogenizer (Kinematica)
5. M-270 Epoxy Dynabeads (Invitrogen) conjugated to rabbit IgG (MP Biomedicals) according to manufacturer's protocol
6. Magnetic stands for 50 ml Falcon tube and 1.7 ml microcentrifuge tubes
7. TEV protease (stored in 50 mM Tris buffer (pH 7.5), 1 mM EDTA, 5 mM DTT, 50% glycerol, 0.1% Triton X-100)

Velocity sedimentation

1. Sucrose solutions: 10%, 20%, 30%, 40%, and 2.5 M sucrose in 10 mM Bis-Tris buffer (adjust to pH 6.5 with HCl), 0.1 mM $MgCl_2$
2. Thick wall polycarbonate tubes: 11 x 34 mm (Beckman Coulter)
3. Ultracentrifuge Rotor TLS-55 (Beckman Coulter)

Methods

Growing, harvesting, and lysing cells

This protocol has been adapted from Michael Rout's lab (http://lab.rockefeller.edu/rout/protocols). The lysis technique with the Retsch PM 100 ball mill grinder increases the percent of cells lysed and decreases protein degradation, resulting in higher yields.

1. Grow 10 ml YPD culture of cells overnight and maintain in log phase growth to inoculate 2 L culture.
2. Grow 2 L YPD culture of cells overnight to 4.5 x 10^7 cells/ml (still in log phase)
3. Pellet cells at 4000xg for 10 minutes at 4°C in 1 L bottles.
4. Resuspend cell pellet in 25 ml cold dH_2O on ice. Transfer cells to 50 ml Falcon tubes and pellet cells at 2600xg for 5 minutes at 4°C.
5. Combine 2 cell pellets and resuspend in 15 ml cold dH_2O. Spin down at 2600xg for 5 minutes at 4°C.
6. Resuspend pellet in 15 ml cold resuspension buffer. Pellet at 2600xg for 15 minutes at 4°C. Decant the supernatant.
7. Pellet again at 2600xg for 15 minutes at 4°C to remove excess buffer. At this point, the pellet should be a relatively dry, thick paste.
8. Cool a 50 ml Falcon tube and fill with liquid nitrogen. Using an 18G needle, poke holes in the tube lid to allow liquid nitrogen vapor to escape.
9. With a spatula, scoop out the cell paste and transfer to a 20 ml syringe. Press the cell paste into the liquid nitrogen in the Falcon tube, creating noodles.

10. When all cells have been frozen, loosely cap tube to allow liquid nitrogen to escape. Store at -80°C.
11. To lyse cells, cool a 125 ml stainless steel grinding jar and stainless steel grinding balls in liquid nitrogen.
12. Empty the contents of one 50 ml Falcon tube of frozen cell noodles into the grinding jar and fill the jar with grinding balls.
13. Ensure the counterweight is properly set.
14. Start grinding program: 3 x 1 min grinding cycles at 400 rpm, reversing directions with each cycle.
15. At the end of the grinding program, cool the grinding jar in liquid nitrogen.
16. Repeat the grinding program and cooling 7 more times, or until you get satisfactory lysis.
17. When lysis is complete, scoop out the lysed cell dust and transfer to the cooled 50 ml Falcon tube (see **Note 1**). Store lysed cells at -80°C.

Spindle pole body purification

Previous purification protocols were modified to increase the yield and stability of purified spindle pole bodies. Prior techniques were laborious and time-intensive, whereas this protocol has reduced the purification to a few hours.

1. Resuspend 4 g of lysed cells in 20 ml of cold lysis buffer.
2. Homogenize for 30 seconds at speed 5 using PCU-2-110 Homogenizer (Kinematica).
3. Clear lysate at 2000xg for 10 minutes at 4°C.

4. While clearing the lysate, prepare IgG magnetic beads. In a 1.7 ml microcentrifuge tube, take 250 µl of Dynabeads conjugated to rabbit IgG, and place in a magnetic stand to magnetize and collect the beads. Remove the supernatant and resuspend in 250 µl EB1 w/ 300 mM NaCl. Magnetize and repeat wash twice. (We do our own conjugations by following the manufacturer's instructions.)
5. Transfer cleared cell lysate to a clean 50 ml Falcon tube. Add 250 µl of IgG conjugated Dynabeads.
6. Incubate on a Nutator (Clay Adams) to prevent beads from settling for 30 minutes at 4°C.
7. Magnetize beads and resuspend in 100 µl EB1 w/ 200 mM NaCl and transfer to 1.7 ml low retention microcentrifuge tube.
8. Incubate 2 minutes on a Nutator. Magnetize beads and repeat wash with EB1 w/ 200 mM NaCl twice.
9. Wash once with 100 µl TEV cleavage buffer. Magnetize beads and resuspend in 50 µl TEV cleavage buffer. Add 1 µg TEV.
10. Incubate on a rotator for 2 hours at 4°C (see **Note 2**).
11. Magnetize beads and take supernatant. Store supernatant on ice until velocity sedimentation (see **Note 3**).

Velocity sedimentation

The soluble pool of γ-tubulin small complex and other spindle pole body components exist in the higher fractions of the sucrose gradient (fractions 1-7). Spindle pole bodies, as determined by western blot analysis and verified by mass spectrometry, migrate near the 2.0 M/2.5 M sucrose

interface. Intact spindle pole bodies reproducibly fall in fractions 9-11 (out of 12). The velocity sedimentation effectively separates the soluble pool of spindle pole body components from the intact spindle pole bodies, resulting in a more homogeneous sample.

1. Using a wide-bore tip, load 200 µl of 2.5 M sucrose into a 1 ml thick wall polycarbonate tube for the TLS-55 rotor.
2. Carefully, to avoid mixing, use wide-bore tips to layer 40%, 30%, 20%, and 10% sucrose solutions in tube.
3. Let sit at 4°C for 2 hours to allow the gradient to equilibrate.
4. Load purified sample onto the sucrose gradient with a wide-bore tip and centrifuge at 50,000 rpm for 5 hours at 4°C in a TLS-55 swinging bucket rotor.
5. Stepwise remove 90 µl fractions from the top of the gradient using a wide-bore tip.
6. To identify which fractions of the sucrose gradient contain spindle pole bodies, spindle pole body components Spc110 and Spc97 can be probed via western blot analysis (see Figure 2.1).
7. Flash freeze 5 µl aliquots of the spindle pole body-containing fractions in liquid nitrogen and store at -80°C.

Notes

1. The ease by which the lysed cells are removed from the grinding jar varies greatly. It helps to fill the jar entirely, with a full 50 ml Falcon tube of cell noodles, as well as thoroughly cool the jar between grinding programs. This will result in a loose powder that can easily be scooped out and transferred to a 50 ml Falcon tube for storage. Insufficient cooling between grinding programs can cause the cell dust to cake on the grinding jar walls, requiring substantial effort to scrape off.
2. At this step, incubation on a rotator is preferred over a Nutator. With the smaller volume during TEV cleavage, the Nutator is insufficient for preventing the Dynabeads from settling to the bottom of the tube.
3. At this step in the purification, you have spindle pole bodies at a high concentration, but contaminated with nucleoli, fragments of the nucleus and soluble g-tubulin small complex. If spindle pole body concentration is of more importance than purity, the TEV eluate from this step can be used in downstream experiments. If purity is of high importance, the TEV eluate can be further purified by velocity sedimentation, however, the concentration of spindle pole bodies will decrease.

Conclusions

The spindle pole bodies purified by the method have been characterized by fluorescence microscopy, mass spectrometry and optical trapping, as described in the following chapters.

Acknowledgements

This work was initiated and further developed in close collaboration with Beth Graczyk and was published in Fong et al, 2016.

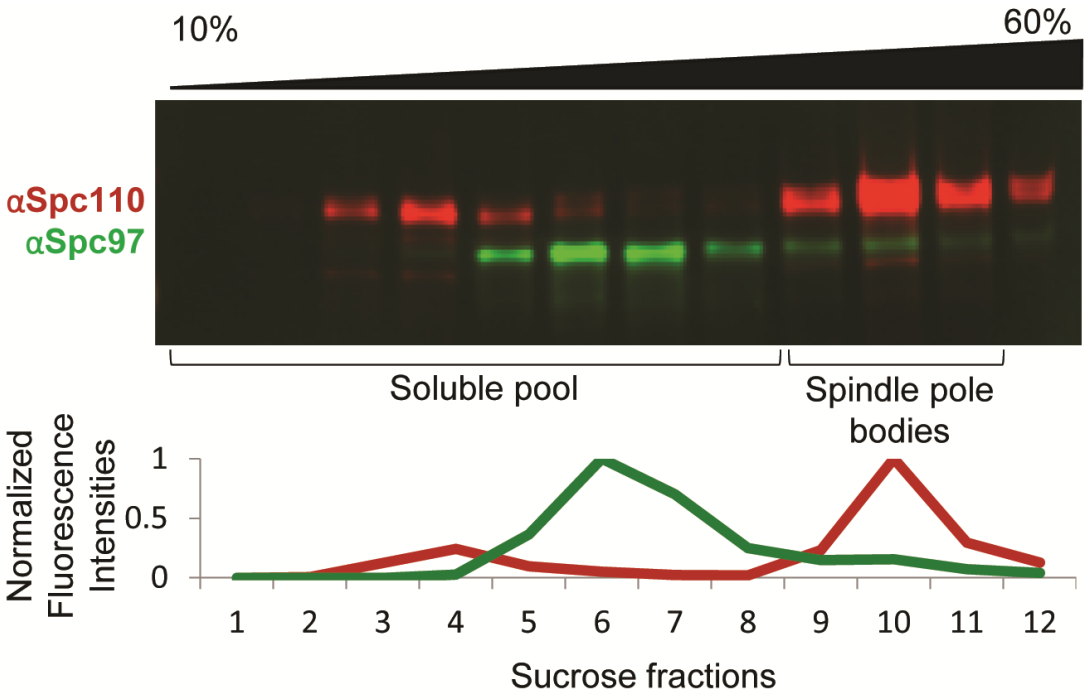

Figure 2.1. Western blot analysis of sucrose gradient fractions.
Twelve fractions (90 µl each) were taken from the top of the sucrose gradient, with sucrose concentration increasing from left (10%) to right (60%). Sucrose fractions were probed for Spc110 (in red) and Spc97 (in green) by western blot analysis. Integrated intensities were normalized to the peak intensity. The soluble pool of spindle pole body components migrate in fractions 1-7 while fully formed spindle pole bodies migrate in fractions 9-11. The presence of all spindle pole body components in fractions 9-11 was further confirmed by mass spectrometry. Note that the antibody against Spc110 is much more sensitive than the antibody against Spc97.

Table 2.1. Strains used in this study.

Strain	Genotype	Reference
W303	*ade2-1oc can1-100 his3-11,15 leu2-3,112 trp1-1 ura3-1*	
BGY72-8A	*MATa SPC42-mCherry::hphMX SPC97-TAP::kanMX*	This study
BGY74-17B	*MATα SPC42-mCherry::hphMX SPC97-TAP::kanMX Tub4-GFP::kanMX*	This study

Chapter 3

Mutagenesis of yeast microtubule nucleation proteins

Introduction

Mitosis is a universal process where cells faithfully segregate two sets of chromosomes between the mother and daughter cells during cell division. The mitotic spindle is a highly regulated macromolecular machine that organizes and regulates this chromosomal movement. During metaphase, chromosomes align along the spindle equator. At the onset of anaphase, the chromosomes are separated to opposite ends of the spindle, ensuring that each cell contains one complete set of chromosomes. Misregulation or defects in the mitotic spindle cause aberrant chromosome segregation, which can lead to aneuploidy or genomic instability in an organism. The budding yeast spindle pole body organizes microtubules in the mitotic spindle to carry out chromosomal segregation. Microtubules play several key roles during mitosis; kinetochore microtubules regulate the movements of the chromosomes, interpolar microtubules stabilize the spindle structure, and cytoplasmic microtubules position the spindle and nucleus within the dividing cell (Jacobs *et al.*, 1988). Although microtubules are critical for accurate chromosome segregation, it is still unknown how microtubules are nucleated *in vivo*.

Microtubules are filamentous polymers composed of α- and β-tubulin heterodimers that associate end-to-end to form long protofilaments. *In vitro*, microtubules exist as hollow tubes with twelve to sixteen protofilaments, with fourteen-protofilament structures predominating (McEwen and Edelstein, 1977; Pierson *et al.*, 1978; Langford, 1980). However, *in vivo*, it has been noted that microtubules almost always exist in a thirteen-protofilament structure (Tilney *et al.*, 1973; Pierson *et al.*, 1978; Scheele *et al.*, 1982; Evans *et al.*, 1985; Bechstedt and Brouhard,

2012). These observations suggest that cells possess a regulatory mechanism that favors the nucleation of thirteen-protofilament microtubules that is missing from *in vitro* nucleation assays.

The discovery of a novel tubulin paralog, γ-tubulin (Tub4 in yeast), marked the first identification of a protein essential for microtubule nucleation (Oakley and Oakley, 1989; Oakley *et al.*, 1990; Stearns *et al.*, 1991; Joshi *et al.*, 1992; Sobel and Snyder, 1995; Marschall *et al.*, 1996). Further investigation revealed that γ-tubulin is a component of a highly conserved heterotetramer, the γ-tubulin small complex, which is essential for microtubule nucleation (Oakley *et al.*, 1990; Moritz *et al.*, 1995; Zheng *et al.*, 1995; Geissler *et al.*, 1996; Spang *et al.*, 1996a; Knop *et al.*, 1997; Oegema *et al.*, 1999; Vinh *et al.*, 2002). In *Saccharomyces cerevisiae*, the γ-tubulin small complex is comprised of two Tub4 molecules and one copy each of Spc97 and Spc98. This stable complex localizes to both sides of the spindle pole body. The kinetochore microtubules and the interpolar microtubules emanate from γ-tubulin small complexes anchored to the nuclear side of the spindle pole body via interactions with Spc110 (Knop and Schiebel, 1997, 1998; Sundberg and Davis, 1997; Nguyen *et al.*, 1998). Cytoplasmic microtubules are anchored to the spindle pole body via interactions with Spc72 on the cytoplasmic face of the spindle pole body (Knop and Schiebel, 1998; Souès and Adams, 1998; Usui *et al.*, 2003).

Although all components of the γ-tubulin small complex have been identified, *in vitro* assays with purified components have often failed to reproduce efficient nucleation (Oegema *et al.*, 1999; Vinh *et al.*, 2002; Kollman *et al.*, 2008, 2010). Recombinant yeast γ-tubulin small complex purified from insect cells only exhibited a three-fold increase in nucleation over background (Vinh *et al.*, 2002). Similarly, γ-tubulin small complexes isolated from *Drosophila* only showed a two to three fold increase over background (Oegema *et al.*, 1999). In higher

eukaryotes, a higher order ring structure has been observed and purified. These complexes are called γ-tubulin ring complexes and consist of several copies of γ-tubulin small complexes as well as at least four ancillary proteins (Zheng *et al.*, 1995; Moritz *et al.*, 1998; Oegema *et al.*, 1999). The γ-tubulin ring complex in *Drosophila* was approximately twenty-five times more active than the γ-tubulin small complex, suggesting that the higher order structure is required for nucleation activity (Oegema *et al.*, 1999). Homologs of the γ-tubulin ring complex accessory proteins do not exist in yeast. However, it was observed that yeast γ-tubulin small complexes spontaneously oligomerize *in vitro,* forming ring structures similar to those seen in higher eukaryotes (Kollman *et al.*, 2010). Unfortunately, while these purified oligomers were shown to be more active than individual γ-tubulin small complexes, the oligomers were still poor nucleators *in vitro*—only a three-fold increase over background was observed (Kollman *et al.*, 2008, 2010). Recently, it was found that while nucleation had historically been poor with the yeast γ-tubulin small complex ring, this may have been an artifact of using bovine brain tubulin instead of tubulin purified from yeast. With yeast tubulin, the yeast γ-tubulin small complex ring nucleated at a rate approximately 300 fold over background (Kollman *et al.*, 2015).

It was hypothesized that conformational changes in the γ-tubulin small complex would activate the complex for nucleation. Close examination of the γ-tubulin small complex ring electron microscopy structure revealed a discrepancy between the ring and the geometry of a microtubule. The inter-γ-tubulin distance in the ring structure was wider than the distance between two laterally-contacting tubulin molecules in the microtubule. There was also a slight difference in the diameter of the ring and the pitch of the helix when compared to a microtubule. The introduction of two cysteines into Tub4 allowed for the formation of a disulfide bond between the Tub4 molecules, bringing the two molecules together, and eliminating the

discrepancy between the structure of the γ-tubulin ring complex and the structure of a microtubule. In addition to exhibiting conformational changes, the crosslinked ring complex became a potent microtubule nucleator, nucleation 600 fold above background with yeast tubulin (Kollman *et al.*, 2015).

Given the results of the *in vitro* nucleation assays, we hypothesized that additional regulation or activation of the microtubule nucleating proteins was required for efficient nucleation. While crosslinking of the γ-tubulin ring complex ectopically activated the nucleator, the conformational changes and activation of the complex must be regulated differently *in vivo*. Little is known about the atomic structure of Spc110 or the functional domains of Spc97 and Spc98, but genetic approaches can identify candidate regions for the regulation of nucleation. Here, we present several mutational approaches, both targeted and comprehensive, to understand how the structures and conformations of Spc97, Spc98, and Tub4 facilitate microtubule nucleation *in vivo.*

Materials and methods

Strains, plasmids, and media

The yeast strains used in this study were all derived from W303 and are listed in Table 2.1. To make red/white plasmid shuffle strain KFY5-5A, the endogenous copy of *SPC98* was deleted by homologous recombination of a PCR amplified *kanMX* deletion cassette from pFA6a-GFP(S65T)-kanMX6 (Bähler *et al.*, 1998) and verified by PCR. The diploid was transformed with the *ADE3* plasmid pKF12 (*ADE3 LYS2 SPC98)* and selected on SD-lys media. The transformants were sporulated and dissected for the haploid KFY5-5A. *SPC98* mutations were integrated into the genome by transformation of mutant alleles on *URA3* yeast integrating plasmids into KFY5-5A. Red and white sectoring transformants were selected on SD-ura low ade media and struck out again on SD-ura low ade to isolate white colonies, which contained the mutant allele as the only copy of *SPC98.* The same method was used for mutant alleles of *SPC97* (using red/white strains TNY65-2B for plasmid shuffle screens and KFY38-5C for fluorescence microscopy), *SPC98* (using another red/white strain KFY37-4C for fluorescence microscopy), and *TUB4* (using red/white strains BGY56-2C for plasmid shuffle screens, and BGY63-5C and KFY220-1A for fluorescence microscopy).

The plasmids used in this study are listed in Table 2.2. QuikChange Lightning Multi Site-Directed Mutagenesis (Stratagene) was used to construct plasmids containing point mutations. C-terminally GFP-tagged proteins were created by PCR amplifying the *GFP-kanMX* cassette from the plasmid pFA6a-GFP(S65T)-kanMX6 with primers containing homology around stop codon of the gene of interest (Bähler *et al.*, 1998). N-terminally GFP-tagged Spc98 was created by PCR amplification of the *GFP-kanMX* cassette from pYGFPgN with primers

sharing homology around the start codon of *SPC98* (Prein *et al.*, 2000). The cassettes were then transformed into yeast and transformants were selected for on YPD+G418 plates.

YPD and SD media were as previously described (Burke *et al.*, 2000). YPD+G418 is YPD with 200 μg/ml G418 sulfate. SD-ura low ade and SD-lys were previously described (Sundberg *et al.*, 1996; Tien *et al.*, 2013).

Linker scanning mutagenesis

Two target plasmids were constructed containing the ampicillin resistance gene for selection in bacteria, and *URA3* for selection in yeast, and either *SPC97* or *SPC98* (pKF56 and pKF35, respectively). Also critical, all *NotI* restriction sites were removed from the plasmids. The transposon contained a kanamycin resistance gene and was flanked on either side by *NotI* restriction sites. The transposon was introduced into the target plasmid by incubating the target plasmid and transposon with the transposase MuA (Finnzymes) at a low transformation efficiency to ensure one insertion per plasmid. MuA does not have sequence specificity, so the transposon was randomly incorporated into the plasmid. The reaction was transformed into *E. coli* and successful transposition events were isolated by growing under ampicillin and kanamycin selection. All of the colonies were pooled and the plasmid DNA was harvested. To remove the kanamycin cassette, the pooled plasmids were digested with *NotI* restriction endonuclease then re-ligated. The resulting "transposition library" contained plasmids that each contained a fifteen base pair insertion in a random location. Each fifteen base pair insertion contained a five base pair duplication and the eight base pair *NotI* recognition site.

Red/white plasmid shuffle screen

The transposition library was transformed into a yeast strain to screen for lethal mutations by a red/white plasmid shuffle screen. The yeast strain constructed for the screen had the following genotype: *ade2-1oc ade3Δ lys2Δ spc97Δ::TRP1 (or spc98Δ::kanMX)*. Both *SPC97* and *SPC98* are essential, so the strains survived on wild type copies of the genes expressed off 2 μm *ADE3* plasmids (pKF12 and pTN25). The presence of the *ADE3* plasmid in a genomic background *ade2-1oc ade3Δ-100* led to the accumulation of red pigment in the cell, therefore yeast colonies that contained the *ADE3* plasmid appeared bright red (Bender and Pringle, 1991). The linker scanning mutagenesis transposition libraries for *SPC97* and *SPC98* were transformed into the respective red yeast strains and grown on selective SD-ura low ade plates at 37 °C to isolate the yeast colonies that were successfully transformed with a transposition library plasmid. Mutations that had no effect on cell viability allowed the cell to survive with the mutated gene, making the red plasmid extraneous. These colonies had a sectored appearance—red in the center and white around the edges as the colonies lost the *ADE3* plasmid. Lethal mutations abolished function of the mutant protein and only the cells that retained the *ADE3* plasmid with the wild type copy of the gene survived. Therefore, lethal mutations were identified as unsectored red colonies. These colonies were isolated and the plasmid DNA was purified for Illumina sequencing.

The unsectored red colonies were isolated from the screen and regrown on plates at 25°C and 37°C. Some colonies sectored when grown at 25°C. These were conditional lethal temperature sensitive mutants. These mutants were grown at the permissive temperature of 25°C and shifted to the restrictive temperature of 37°C to determine phenotypic changes. Plasmid

DNA was purified from the temperature sensitive mutants and traditional Sanger sequencing was used to identify insertion positions.

Illumina sequencing

For each gene, two samples were prepared for Illumina sequencing. The first sample was the transposition library that was transformed into yeast for screening in order to determine the coverage of the gene. The second sample contained the plasmids from lethal mutants that were isolated from the plasmid shuffle screen and pooled. Sequencing of the lethal mutant sample mapped to essential regions of the gene. Primers were designed to specifically amplify the mutant allele off of the mutant library plasmid and not the wild type copy off of the *ADE3* plasmid. The PCR product was sheared to an average size of 500 base pairs by sonication and the ends of the products were repaired with End-It Repair Kit (Epicentre), and A-tailed for ligation of adaptors. The products were size-selected (250-350 base pairs) on an agarose gel and enriched by PCR. Each library pool was labeled with flow cell adaptors containing unique 6 base pair indices to enable multiplexed Illumina sequencing. Thirty-six base pair reads were collected and mapped onto the gene sequence (Integrative Genomics Viewer). Custom programs were used to analyze the FASTQ Illumina sequencing files (Alex Zelter). The custom programs identified *NotI* sites within the sequencing, and flanking sequences were aligned to *SPC97* or *SPC98* using mrsFAST (Hach *et al.*, 2010) to identify insertion positions within the gene. Read coverage was determined by aligning all reads to *SPC97* and *SPC98* using mrsFAST.

Fluorescence microscopy

All images were acquired using a DeltaVision system (Applied Precision) with an IX70 inverted microscope (Olympus), a U Plan Apo 100x objective (1.35 NA) and a CoolSnap HQ

digital camera (Photometrics). Exposures were 0.4 s for mCherry and GFP. Images were processed as previously described (Shimogawa *et al.*, 2009) using custom Matlab programs to identify GFP and mCherry foci and quantify the fluorescence intensities. For live-cell imaging, cells were mounted on an agarose pad as previously described (Muller *et al.*, 2005).

Insect cell protein expression and purification

Recombinant proteins were expressed in Sf9 cells using the Bac-to-Bac Baculovirus Expression System (ThermoFisher Scientific). The yeast genes were PCR amplified and inserted into pFastBac (see Table 3.2 for plasmids). Baculoviruses were produced in Sf9 cells according to manufacturer protocols. Sf9 cells were grown in suspension (1-10 x 10^6 cells) and co-infected with baculoviruses for forty-eight to seventy-two hours. To harvest cells, cultures were spun at 600 × g for 10 minutes. Cell pellets were washed with phosphate-buffered saline and 1 mM PMSF and repelleted. Pellets were stored at -80°C.

For purifications, HisPur Ni-NTA magnetic beads (Thermo Scientific) were used with modifications to manufacturer protocols. Insect cell pellets were resuspended in HB100 buffer, pH 7.5 with protease inhibitors (40 mM HEPES, pH 7.5; 100 mM NaCl; 0.1 mM EGTA, pH 8; 0.1 mM GTP, pH 8; 25 mM imidazole; 1% NP40; 2 μg/ml aprotinin, pepstatin, leupeptin, chymostatin; 1 mM PMSF) and sonicated to lyse cells. The cell lysate was added to Ni-NTA magnetic beads (that had been equilibrated in HB100 buffer (40 mM HEPES, pH 7.5; 100 mM NaCl; 0.1 mM EGTA, pH 8; 0.1 mM GTP, pH 8; 25 mM imidazole)) and incubated for thirty minutes on a rotator at 4°C. The beads were magnetized and washed with HB100. The protein was eluted with 1 M imidazole in HB100, rotating for fifteen minutes at 4°C.

TAP purification and velocity sedimentation of spindle pole bodies

Spindle pole bodies were purified by a TAP-tag on Spc97, as previously described (Chapter 2). Sucrose gradients were generated by allowing five steps of sucrose solutions (200 µl each of 10%, 20%, 30%, 40%, 2.5 M sucrose) to equilibrate at 4°C for 2 hours. The TEV eluate was then applied to the sucrose gradient and spun at 50000 rpm for 5 hours at 4°C in a TLS55 rotor (Beckman Coulter). Fractions (90 µl) were removed from the top of the gradient with wide-bore tips. The presence of spindle pole bodies was determined by western blot analysis, probing for Spc110 and Spc97. Western blot analysis showed the separation of intact spindle pole bodies (fractions 9-11) from the soluble pool of spindle pole body components (fractions 1-8).

In vitro nucleation assays

To test *in vitro* nucleation off of purified spindle pole bodies, a flow cell was constructed with KOH cleaned glass coverslips. Spindle pole bodies were diluted with 5X BRB80/BSA (400 mM K-PIPES, pH 6.9, 5 mM $MgCl_2$, 5 mM EGTA, 40 mg/ml BSA) and KCl to a final concentration of BRB80 (80 mM K-PIPES, pH 6.9, 1 mM $MgCl_2$, 1 mM EGTA), 8 mg.ml BSA and 500 mM KCl. The diluted spindle pole bodies were flowed into the flow cell and allowed to nonspecifically adhere to the coverslip for thirty minutes. Free tubulin was flowed into the flow cell in the tubulin buffer (BRB80, 6 µg/ml BSA, 1.5 µg/ml κ-casein, 20 µM Alexa647-labeled tubulin (cleared by spinning at 90 krpm, 10 minutes, 4°C), 1 mM GTP). If nucleation was occurring in the presence of taxol, 2 µM taxol was added to the tubulin buffer. Free tubulin was incubated at 37°C for fifteen minutes before washing with BRB80/BSA and 10 µM taxol and sealing the flow cell and fluorescent imaging.

Results

Linker scanning mutagenesis of Spc97 and Spc98

Linker scanning mutagenesis is an efficient method to comprehensively cover a gene with random insertions and provide information about a protein's structure and function. Coupled with a plasmid shuffle screen and high-throughput sequencing, this approach used a transposon mutagenesis system (Finnzymes) to introduce a fifteen base pair insertion randomly throughout *SPC97* and *SPC98*. The first step of this mutagenesis approach was the generation of the transposition library (Figure 3.1). Each plasmid in the transposition library contained a single random fifteen base pair insertion in the plasmid. This fifteen base pair insertion was composed of a five base pair duplication of the target DNA site and the eight base pair *NotI* recognition site. If the insertion fell in the translated protein, the fifteen base pair insertion would result in an in-frame five amino acid insertion. By virtue of the transposon mutagenesis system, this five amino acid insertion would never result in the inclusion of a frame shift or stop codon.

For *SPC97,* the transposition library was composed of approximately 75,000 plasmids, and for *SPC98,* the library contained approximately 56,000 plasmids. Given that the *SPC97* plasmid was 7.9 kb and the *SPC97* gene was 2.5 kb, Poisson statistics suggested 100% confidence of coverage of each base pair of the gene. Similarly, with *SPC98* plasmid was 8.1 kb and the *SPC97* gene was 2.5 kb, suggesting 100% coverage within the transposition library.

This transposition library was prepared for Illumina sequencing to determine the actual coverage of the genes (Figure 3.3; Table 3.3). Identification of *NotI* recognition sequences and subsequent sequence alignment to the genome determined that there were 2,194 unique insertion

events in *SPC97* and 2,105 unique insertion positions in *SPC98*, which means 98.3% of the codons in *SPC97* and 97.3% of the codons in *SPC98* were affected by a transpositional event. The distribution of these events was even across the genes, with an average of 17.6 insertion events per twenty base pair window for *SPC97* and 16.8 insertions events per twenty base pair window for *SPC98* (Figure 3.4). In addition, the types of insertions were evenly represented. The fifteen base pair insertion can be made in any of the three reading frames of the gene. In *SPC97*, 28.0% of the insertions were in frame one, 25.3% of the insertions were in frame two, and 46.7% of the insertions were in frame three. In *SPC98*, 27.2% of the insertions were in frame one, 25.5% of the insertions were in frame two, and 47.2% of the insertions were in frame three.

The transposition library was then transformed into *Saccharomyces cerevisiae* for a plasmid shuffle screen to identify lethal mutations in *SPC97* and *SPC98* (Figure 3.2). In this screen, yeast colonies that were transformed with a library plasmid containing a lethal mutation would be red. For *SPC97*, 31,881 yeast colonies were screened and 1,188 (3.7%) were found to contain a lethal mutation. For *SPC98*, 57,582 yeast colonies were screened and 2,486 (4.3%) contained a lethal mutation. The mutated plasmids were extracted from the red colonies and pooled for Illumina sequencing.

The DNA from the red colonies were sequenced (Table 3.4), and 607 unique sites were identified in *SPC97*, corresponding to 24.6% of base pairs. Similarly, in *SPC98*, 578 unique sites were identified, corresponding to 22.8% of base pairs. For each pool of lethal mutations, the distribution across the three reading frames was relatively equal (31.2%, 28.1%, and 40.7% for *SPC97* and 27.9%, 31.4%, and 40.6% for *SPC98*), suggesting that it was the position of the insertion, and not the identity of the insertion, that conferred lethality.

Unlike the transposition library, the distribution of the lethal insertions were clustered (Figure 3.4). Some regions, such as the first 500 base pairs of *SPC98* appeared relatively tolerant of fifteen base pair insertions with low representation in the lethal mutation pool, while other regions, like base pairs 1780-2000 of *SPC98* were enriched for lethal mutations. The clustering of lethal mutations is even more apparent when mapping the lethal insertion densities onto the pseudo-atomic model of Spc97 and Spc98 (Figure 3.5).

Characterization of representative lethal mutations

Representative lethal mutations were selected from each cluster of lethal insertions for further analysis. Five lethal mutations (ins207, ins349, ins854, ins1755, and ins1901) were selected for *SPC97* and seven (ins568, ins886, ins1025, ins1222, ins1432, ins1827, and ins2470) were chosen for *SPC98*, where "ins207" indicates that the first base pair of the insertion is at base pair position 207. Each selected mutation represented the lethal insertion with the highest number of *NotI* reads in the lethal insertion clusters. The representative lethal insertions were mapped onto the pseudo-atomic structure of Spc97 and Spc98 (Figure 3.5). The lethality of these representative mutants were verified by integration of the lethal insertion into the plasmid shuffle strains KFY5-5A and TNY65-2B.

The integrity of γ-tubulin small complexes containing lethal mutations and the strength of the mutant γ-tubulin small complex interaction with spindle pole body linker proteins Spc110 and Spc72 were determined by expressing the proteins in insect cells. Only stable γ-tubulin small complex can be purified from insect cells. For six of the Spc98 lethal mutant proteins, the mutant Spc98 protein was co-expressed with Spc97 and Tub4-His. In addition, the γ-tubulin small complex was co-expressed with calmodulin and either Spc110-GST or Spc72-Spc110-GST

chimera. Full length Spc72-GST was difficult to express solubly in insect cells, so the N-terminus of Spc72 was fused to the C-terminus of Spc110 to improve solubility (Knop and Schiebel, 1998). In comparison to wild type γ-tubulin small complexes, none of the Spc98 lethal mutations formed stable complexes when co-purified with Spc110. The mutant γ-tubulin small complexes were more stable when co-expressed with Spc72, but with the exception of Spc98 ins1432, were less stable than wild type complexes (Figure 3.6). Unfortunately, this experiment could not distinguish between the stability of the γ-tubulin small complex and the interaction between the γ-tubulin small complex and either Spc110 or Spc72.

Complex formation was also examined in yeast strains. Spc98 lethal mutations labeled with GFP were integrated in the *URA3* locus in strains expressing Spc97-TAP and Spc42-mCherry. Spc97 lethal mutations labeled with GFP were integrated into the *URA3* locus in strains expressing PaPreCa-Spc98. TAP purifications of the spindle pole body were performed to determine if the GFP-tagged lethal mutant was incorporated into the spindle pole body. The purified spindle pole bodies were probed with α-Spc98 antibody to monitor the Spc98 lethal mutations or α-Spc97 antibody to monitor the Spc97 lethal mutations. Preliminary results suggested that the endogenous untagged copy of the protein could be differentiated from the GFP-tagged lethal mutant copy by western blot, but technical difficulties with the antibodies precluded the gathering of definitive data regarding the localization of the lethal mutants.

Alternatively, to determine the localization of lethal γ-tubulin small complexes, the mutant proteins were transformed into fluorescent strains. In these strains, Spc42 was labeled with mCherry to identify the spindle pole body. Because this study was with lethal mutants, the endogenous copy of Spc97 or Spc98 was retained. The lethal mutants were tagged with GFP and integrated at the *URA3* locus. Localization of the lethal mutant to the spindle pole body was

determined by measuring co-localization of Spc42-mCherry and the GFP tagged mutant fluorescent signals (Figure 3.7). When compared to wild type, Spc97 ins207 showed about half as much co-localization, while the remaining four lethal mutants weakly localized to the spindle pole body, if at all. With the Spc98 mutants, only Spc98 ins1025 localized to the spindle pole body at levels comparable to wild type Spc98. The remaining six mutants either localized poorly, or did not localize at all.

Characterization of temperature sensitive mutations

Linker scanning mutagenesis also identified temperature sensitive mutants. The red colonies isolated from the screen were regrown at 25°C and screened again for sectoring. Of the 1,188 colonies re-screened for *SPC97*, nine were temperature sensitive. For *SPC98*, nineteen of the 2,486 red colonies were temperature sensitive. Plasmids were isolated from these strains and sequenced by traditional Sanger sequencing to determine the position of the temperature sensitive insertion (Tables 3.5 and 3.6 and Figure 3.8).

The temperature sensitive strains were analyzed by fluorescence microscopy to determine if there were any changes to mitotic spindle morphology or microtubule nucleation. Spc98 temperature sensitive mutants were integrated into KFY37-4C and Spc97 temperature sensitive mutants were transformed into KFY38-5C on a *CEN* plasmid. These fluorescent strains contained Spc42-mCherry to identify the spindle poles and GFP-Tub1 to analyzed microtubule architecture throughout the cell. Asynchronous cultures of each temperature sensitive mutant was shifted to the restrictive temperature of 37°C for thirty minutes before imaging. Of the twenty-eight temperature sensitive mutants, three mutants in Spc98 were found to have abnormal spindle morphology (Figure 3.9).

The first observed phenotype was an increase in the number and length of cytoplasmic microtubules in Spc98 ins35. In wild type cells, there are normally one to three cytoplasmic microtubules responsible for positioning the nucleus throughout the cell cycle. In this temperature sensitive mutant, there were many more cytoplasmic microtubules that were longer and more disorganized. The second novel phenotype was the presence of tubulin accumulations in the cytoplasm of Spc98 ins561. In wild type cells, all microtubules are nucleated from the spindle pole body, so the accumulations occurring away from the spindle pole body is a novel phenotype. In addition, these accumulations did not appear to have extended microtubule formation, so the organization of the tubulin in these accumulations might differ from traditional microtubule nucleation. The third phenotype observed was short and broken metaphase spindles, as seen in Spc98 ins557. This is a well characterized phenotype, suggestive of nucleation deficiency. The mitotic spindle relies on interpolar microtubules and the associated motors to stabilize the spindle structure. In a nucleation deficient mutant, the spindles are no longer stable and collapse.

All three of these temperature sensitive mutations occur in the N-terminus of Spc98. This region of the protein is not represented in the pseudo-atomic model of the γ-tubulin small complex, but it is thought to be involved in binding of the γ-tubulin small complex to both the nuclear face and cytoplasmic face of the spindle pole body through interactions with Spc110 and Spc72, respectively. The location of the insertions also suggests possible involvement in γ-tubulin small complex assembly and inter- and intra-complex lateral attachments. To determine if these phenotypes were related to the interaction between the γ-tubulin small complex and Spc110 and Spc72, the temperature sensitive mutants were expressed in insect cells. Like the lethal mutations, the Spc98 temperature sensitive mutant proteins were co-expressed with Spc97

and Tub4-His. Either Spc110-GST or the chimeric Spc72-Spc110-GST was also co-expressed with calmodulin. For both Spc110 and Spc72, interaction with the γ-tubulin small complex was reduced for all mutants, to varying degrees (Figure 3.10). Spc98 ins557, the mutant with the broken spindles had weaker interaction with Spc110 and Spc72, as predicted by the nucleation deficient phenotype. Both Spc98 ins35 and Spc98 ins561 phenotypes were suggestive of hyper nucleating states, but an increased interaction between the γ-tubulin small complex and Spc110 and Spc72 for both mutants was not observed, suggesting a mechanism of activation other than increased γ-tubulin small complex localization to the spindle pole body.

The phenotypes of Spc98 lethal mutations Spc98 ins35 and Spc98 ins561 suggested the possibility that these mutations caused increases in nucleation activity of the γ-tubulin small complex. To test this *in vivo,* spindle pole bodies expressing Spc98 ins35 and Spc98 ins561 mutant proteins were purified as previously described from KFY177-30B and KFY179-53D, respectively (according to the protocol described in Chapter 2). Nucleation was tested for wild type spindle pole bodies and each of the two mutant spindle pole bodies in an *in vitro* nucleation assay on a coverslip (Figure 3.11). In the absence of taxol, wild type spindle pole bodies and Spc98 ins35 were poor nucleators. Spc98 ins561 exhibited higher nucleation in the absence of taxol, although not necessarily at spindle pole body fluorescent foci. In the presence of taxol, Spc98 ins35 had nucleation similar to wild type, with perhaps more bundling and more interconnected microtubule networks. Spc98 ins561 also showed higher nucleation in the presence of taxol, but was also marked by the appearance of numerous short microtubules nucleating away from the spindle pole bodies. These *in vitro* results were consistent with the *in vivo* phenotypes observed for these two mutants.

Designed mutants of Spc97 and Spc98

The crystal structure of GCP4 has been docked into the electron microscopy structure of the yeast γ-tubulin small complex as a pseudo-atomic model of the complex (Kollman *et al.*, 2010, 2015; Guillet *et al.*, 2011). However, there are EM densities in Spc97 and Spc98 that are not approximated by the GCP4 crystal structure (Figure 3.12). Deletions were made in Spc97 and Spc98 to remove these regions of the proteins and determine the effect on cell viability. Most of the regions that were deleted fell in the loop regions of the GCP4 crystal structure. For both proteins, the N-termini are poorly characterized by the GCP4 structure. Two N-terminal deletions were made for each of the proteins. One deletion (1-55 aa in Spc97 and 1-160 aa in Spc98) deleted the region of the protein that is not present in GCP4. N-terminal deletions (1-96 aa in Spc97 and 1-221 aa in Spc98) deleted region with a predicted alpha helix and two predicted beta strands that could be important for interaction with Spc110. Plasmids containing these deletions were made and transformed into TNY65-2B (for Spc97 mutations) and KFY5-5A (for Spc98 mutations). These two strains are red/white plasmid shuffle strains (described in Methods and Materials). Transformants that are red and unsectored contain mutant proteins that are not sufficient for cell viability and must retain the *ADE3* plasmid with a wild type copy of the gene. If the mutation in the protein can sustain cell growth, the colonies will lose the *ADE3* plasmid and red coloration will begin to sector white as the plasmid is lost. In Spc97, deletion 198-238 aa and deletion 491-550 aa sectored weakly, suggesting that while they affect cell growth but they are sufficient for viability. Deletions 1-55 aa, 1-96 aa, and 714-754 aa did not sector, suggesting that these regions are essential for cell viability. In Spc98, all of the deletions (1-160 aa, 1-221 aa, 671-718 aa, 744-761 aa) were all essential for viability and none of these strains sectored in the plasmid shuffle screen.

The flexibility of Spc98 has been observed by electron microscopy, so specific point mutants were designed in the hinge region of Spc98 based on the GCP4 crystal structure, with the hypothesis that the mutations may straighten the conformation of Spc98 and activate the nucleating complex (Kollman *et al.*, 2008). The hinge region of Spc98 is largely hydrophobic, possibly accounting for the flexibility of the region. Based on alignments of the GCP4 crystal structure, Spc97, and Spc98, residues in Spc98 were mutated to more closely match residues in Spc97, which does not exhibit the same flexibility in the region. These mutations were integrated into KFY37-4C (strains KFY66-KFY74; Table 3.1). All mutants were viable and imaged by fluorescence microscopy, where Spc42-mCherry identified the spindle pole bodies and GFP-Tub1 imaged the microtubules. No abnormal microtubule or spindle morphologies were identified for any of these mutants.

Mutations in Tub4

Gamma-tubulin has been identified as essential for microtubule nucleation (Oakley and Oakley, 1989; Oakley *et al.*, 1990; Stearns *et al.*, 1991; Joshi *et al.*, 1992; Sobel and Snyder, 1995; Marschall *et al.*, 1996). As such, it has been the subject of several mutational studies (Vogel *et al.*, 2001; Keck *et al.*, 2011; Lin *et al.*, 2011). Here, we present data for additional studies of novel point mutations in Tub4.

The original published structure of the yeast γ-tubulin small complex ring exhibited dimensions similar to a microtubule, but did not match exactly (Kollman *et al.*, 2010). This was considered to be the open conformation of the ring. Two cysteine residues were introduced into Tub4 such that under oxidizing conditions, the γ-tubulin small complex would be trapped in a closed conformation that would more perfectly match the diameter and pitch of a microtubule.

The Tub4 mutations, S58C and G288C, referred to as γTUSC^{cc}, allowed for the formation of a disulfide bond between Tub4 molecules in the same γ-tubulin small complex. These mutations induced the closed conformation of the γ-tubulin small complex ring, perfectly matching the geometry of a microtubule, and enhancing the nucleation activity of the purified complex (Kollman *et al.*, 2015). However, *in vivo*, the mutations did not have an effect on cell viability (Figure 3.13). The γTUSC^{cc} was transformed into a strain with an oxidizing environment, due to *GLR1* deletion. *GLR1* encodes glutathione reductase, so *glr1*Δ cells were used to maximize the chance that the γTuSC^{CC} disulfides would be oxidized. The tubulin distribution and the kinetochore distribution in the mitotic spindle were measured by fluorescence microscopy with Spc42 tagged by mCherry to visualize the spindle pole bodies (Figure 3.13.a). The distribution of tubulin fluorescence across a mitotic spindle was measured by GFP-Tub1 across various lengths (Figure 3.13.c). In comparison to cells expressing wild type γ-tubulin complex and cells expressing wild type γ-tubulin complex in the presence of *glr1Δ*, γTuSC^{CC} did not affect tubulin distribution at any spindle length. The distribution of kinetochore fluorescence was measured by Nuf2-GFP across various spindle lengths (Figure 3.13.d). Metaphase spindles (1.28- 1.59 μm), showed no difference in kinetochore distribution, although shorter spindles showed kinetochores clustering closer to the spindle pole bodies.

With the publication of the yeast phosphoproteome, several phosphorylation sites were reported for Tub4 (Keck *et al.*, 2011). One site of interest was T130. In humans, S131 is phosphorylated by SadB kinase. Expression of S131D increased centrosome numbers and S131A showed problems with centrosome duplication (Alvarado-Kristensson *et al.*, 2009). However, T130A and T130D mutations did not show the same phenotypes when mutated in yeast; all mitotic cells had two spindle pole bodies. The effects of these mutations on the mitotic

spindle were much subtler. Tub4 T130A and T130D were integrated into fluorescent strains with Spc42-mCherry to identify spindle pole bodies and either GFP-Tub1 to monitor tubulin distribution or Nuf2-GFP to monitor kinetochore distribution (Figure 3.14.a). The tubulin distributions of both mutants were similar to wild type, but the kinetochore distributions showed greater changes. Tub4 T130A mutation resulted in kinetochore clustering closer to the spindle pole body while T130D resulted in kinetochore clustering closer to the midpoint of the spindle.

Another residue of interest in Tub4 was T239, this is a residue conserved in the tubulin family. A mutant of β-tubulin, tub2-150, was isolated in yeast and exhibited benomyl dependence for mitotic growth at 34°C, due to hyperstable microtubules, both *in vivo* and *in vitro* (Stearns *et al.*, 1990; Machin *et al.*, 1995, 1996; Geyer *et al.*, 2015). Tub2-150 contains a T238A mutation, a mutation that is buried in the core of the protein and part of a helix that has large conformational changes as free tubulin dimers become incorporated into microtubules. Tub4 also contains a threonine at amino acid position 239. Tub4 T239A, T239S, and T239V were transformed into fluorescent strains with Spc42-mCherry to identify spindle pole bodies and either GFP-Tub1 or Nuf2-GFP to visualize tubulin and kinetochore distributions (Figure 3.14.b). The tubulin distributions of T239S and T239V were very similar to wild type, but the T239A mutation resulted in a broadening of the tubulin distribution across the metaphase spindle. The kinetochore distributions changed widely among all three mutants. T239S had kinetochore distributions similar to wild type Tub4, with slightly more kinetochore fluorescence at the spindle midzone. T239A caused kinetochores to cluster closer to the spindle midpoint and have a broader distribution. T239V showed even more broadening of the kinetochore cluster.

Discussion

Linker scanning mutagenesis identifies regions essential for function or structure of Spc97 and Spc98

Previous applications of linker scanning mutagenesis have been successfully used to study the complex formation and functional regions of both the cohesion complex and the Ndc80 complex, map protein-protein interfaces, and analyze Cre recombinase activity (Petyuk *et al.*, 2004; Milutinovich *et al.*, 2007; Pajunen *et al.*, 2007, 2009; Tien *et al.*, 2013). Here, the essential regions of Spc97 and Spc98 were mapped using a combination of linker scanning mutagenesis, a plasmid shuffle screen in yeast, and next-generation high-throughput DNA sequencing. The transposition library of the linker scanning mutagenesis was comprehensive, covering 88.8% of the base pairs in *SPC97* and 82.3% of the base pairs in *SPC98* with a fifteen base pair insertion. In the plasmid shuffle screen, only 4% of the yeast colonies screened contained a lethal insertion, which mapped to 24.6% and 22.8% of *SPC97* and *SPC98* base pairs, respectively. This suggests that the majority of the protein can tolerate a five amino acid insertion. Out of this screen, lethal mutations and temperature sensitive mutations were identified for further characterization.

Lethal mutations in Spc97 and Spc98 disrupt complex formation and spindle pole body localization

Five representative lethal mutations (ins207, ins349, ins854, ins1755, and ins1901) were selected for *SPC97* and seven (ins568, ins886, ins1025, ins1222, ins1432, ins1827, and ins2470) were chosen for *SPC98* based on the clustering of lethal insertion sites in three dimensional structure of the protein. Complex formation with the Spc98 lethal mutants were studied by

recombinant protein co-expression of the mutant γ-tubulin small complexes and the spindle pole body linker proteins Spc110 or Spc72. Purification of the γ-tubulin small complex by a His-tag on Tub4 showed the complex was not stable and did not purify well when co-expressed with Spc110. When co-expressed with Spc72, more of the γ-tubulin small complex was purified, suggesting that while the complex was still not entirely stable, the presence of Spc72 was able to stabilize it better than interactions with Spc110. Of note, Spc98 ins1432 mutant complex was as stable as wild type complex when co-expressed with Spc72.

The correct cellular localization of the lethal mutants of Spc97 and Spc98 were studied in fluorescently labeled yeast strains. In these strains, Spc42-mCherry indicated the spindle pole body and GFP-labeled lethal mutants of either Spc97 or Spc98 were expressed over the endogenous unlabeled Spc97 or Spc98. Colocalization of mCherry and GFP signal was interpreted as the correct localization of the mutant γ-tubulin small complex to the spindle pole body. For Spc97, only Spc97 ins207 showed appreciable localization to the spindle pole body and for Spc98, only Spc98 ins1025 localized to the spindle pole body at levels similar to wild type. The other ten mutant complexes could not localize to the spindle pole body or were outcompeted by the endogenous γ-tubulin small complex.

Based on the localization of these lethal mutations on the pseudo-atomic model, we can hypothesize about the interactions that are disrupted by each of the mutations. Several of the lethal mutations (Spc97 ins207, ins349, and Spc98 ins568, ins886) clustered in the N-termini of Spc97 and Spc98. The positions of these mutations suggested that they may affect lateral interaction within a γ-tubulin small complex or between two γ-tubulin small complexes. The locations of these insertions also suggest an effect on γ-tubulin small complex interaction with linker proteins Spc110 and Spc72. Many other lethal mutations are hypothesized to affect the

interaction site between γ-tubulin and either Spc97 and Spc98 (Spc97 ins1755, and ins1901 and Spc98 ins1432, ins1827, and ins2470). The binding of γ-tubulin is essential for the formation of the complex and the γ-tubulin binding domain is well conserved, suggesting that disruption of this interface is sufficient to induce lethality. The remaining lethal insertions localized to the middle of Spc97 and Spc98, according to the pseudo-atomic model. The effects of these insertions cannot be hypothesized based on location, but may play a role in the conformational changes or regulation of the flexibility in Spc98.

Temperature sensitive mutants in Spc98 display novel nucleation phenotypes

Temperature sensitive mutants were identified in linker scanning mutagenesis by growing colonies containing lethal mutations at 25°C and rescreening for lethality. In this screen, nine mutations in *SPC97* were viable at the lower temperature and nineteen mutations were viable in *SPC98*, suggesting that these were conditional lethal temperature sensitive mutations. These temperature sensitive mutations were transformed into fluorescent yeast strains and screened for microtubule-related phenotypes. Three temperature sensitive mutants of Spc98 exhibited unique microtubule phenotypes and were characterized further.

The first temperature sensitive mutant contained an insertion at base pair 35, and was characterized by an increase in the number and length of cytoplasmic microtubules. Spc98 anchors the γ-tubulin small complex to the spindle pole body via N-terminal interactions with Spc110 on the nuclear side and Spc72 on the cytoplasmic side. The location of the insertion at the N-terminus of Spc98 suggested that this mutation may affect N-terminal protein interactions. One possibility was that this mutant may have an increased affinity for Spc72, localizing more γ-tubulin small complexes to the cytoplasmic face and increasing nucleation. The compact nature

of the yeast mitotic spindle made it difficult to determine if the increase in microtubule numbers also occurred in the nucleus, so we could not determine if this was specific to the interaction with Spc72. When expressed recombinantly in insect cells, less Spc98 ins35 mutant γ-tubulin small complex co-purified with both Spc110 and Spc72 in comparison to wild type γ-tubulin small complexes. Therefore, the phenotype was most likely not due to stronger interaction with Spc72. Another possible explanation was that the mutation could also have induced a conformational change, locking the γ-tubulin complex in a highly activated nucleating form, or promoted assembly of the γ-tubulin small complex into higher order rings. Under this condition, the increased number and length of microtubules could be due to a hypernucleating state. *In vitro* nucleation assays showed that spindle pole bodies containing the Spc98 ins35 mutation had nucleation similar to wild type spindle pole bodies. However, the microtubules were qualitatively different than wild type, exhibiting more bundling and branching in the microtubule network, suggesting that more microtubules were being nucleated off of each spindle pole body. Electron microscopy of the Spc98 ins35 mutant γ-tubulin small complex would be able to discern whether this mutation affects the conformation of the entire γ-tubulin small complex to more closely match microtubule dimensions and induced a hypernucleation state.

The second temperature sensitive mutant phenotype was the accumulation of tubulin in the cytoplasm. In this mutant, Spc98 ins561, the tubulin accumulations were restricted to short microtubules, and the γ-tubulin small complex may exhibit a novel organization other than traditionally seen at the spindle pole body. *In vitro* nucleation assays have shown that the γ-tubulin small complex alone is a poor nucleator (Oegema *et al.*, 1999; Vinh *et al.*, 2002; Kollman *et al.*, 2008, 2010). The N-terminus of Spc110 was found to stabilize the formation of γ-tubulin small complex filaments, suggesting that the anchoring of the γ-tubulin small complex to the

spindle pole body may affect nucleation activity (Kollman *et al.*, 2010). The position of insertion ins561 on the pseudo-atomic structure of Spc98 suggests that it may influence the interaction between Spc98 and Spc97 of a neighboring complex. This may lock the oligomer of γ-tubulin small complexes into a stable hypernucleating state that does not require the presence of Spc110 or has reduced interactions with Spc110 and Spc72. In support of the reduced affinity for Spc110 and Spc72, recombinant Spc98 ins561 γ-tubulin small complex purified out of insect cells showed the weakest association with Spc110 and Spc72 of the three temperature sensitive mutants, when compared to wild type. In addition, *in vitro* nucleation assays with spindle pole bodies containing Spc98 ins561 showed markedly different nucleation compared to wild type. Spc98 ins561 spindle pole bodies showed more nucleation than wild type spindle pole bodies in the absence of microtubule-stabilizing taxol, but most of the nucleation was short microtubules away from the spindle pole bodies. The qualitative difference in nucleation was also apparent in the presence of taxol, with short microtubules formed away from spindle pole bodies, reminiscent of the tubulin accumulations observed *in vivo.*

The third temperature sensitive phenotype was short and broken metaphase spindles. Short metaphase spindles may be indicative of nuclear microtubule deficiencies. Studies with Tub4 mutants have used thin section EM to show that in cells with short metaphase spindles, interpolar microtubules do not form the antiparallel array that would stabilize and maintain spindle length (Lin *et al.*, 2011). This mutant contains an insertion at Spc98 base pair 557. The position on the pseudo-atomic model suggests that it may affect Spc98 interactions with Spc97 of a neighboring γ-tubulin small complex. Interestingly, this Spc98 mutant protein contains an insertion at amino acid K186, only one amino acid away from Spc98 ins561 mutation in Y187. The proximity of these two mutations emphasize that this region must be important for Spc98

interaction with Spc97 from the adjacent small complex. However, while Spc98 ins557 showed deficiencies in microtubule organization, the mutant Spc98 ins561 suggests there may be an increase in nucleation activity. Further investigation of this region and the tunable nature of this region may elucidate how higher order oligomers of the γ-tubulin small complex form and how they facilitate nucleation.

Tub4 mutations affect nucleation activity and kinetochore distributions

Gamma-tubulin is highly conserved and essential for microtubule nucleation, making it a prime candidate for mutation for the study of microtubules and spindle morphology (Oakley and Oakley, 1989; Stearns *et al.*, 1991; Spang *et al.*, 1996a; Jung *et al.*, 2001; Vogel *et al.*, 2001; Keck *et al.*, 2011; Lin *et al.*, 2011). Mutating Tub4 S58 and G288 to cysteines resulted in a mutant referred to as γTUSC^{cc}. These mutations formed a disulfide bond between γ-tubulins in the same γ-tubulin small complex under oxidizing conditions. The disulfide bond between the γ-tubulin molecules induced the closed conformation of the γ-tubulin small complex ring, resulting in diameter and pitch geometry that perfectly matched a microtubule. Gamma-tubulin small complex rings containing the γTUSC^{cc} mutation were also shown to have increased nucleation activity *in vitro* (Kollman *et al.*, 2015). While γTUSC^{cc} had a profound effect on the structure of the ring and the nucleation activity *in vitro*, the mutations did not affect cell viability and had minimal effect on spindle morphology. Expression of γTUSC^{cc} under oxidative cellular environments, did not affect the distribution of tubulin across mitotic spindles varying in length from 0.6 to 1.6 μm. Metaphase spindles (1.28-1.59 μm), showed no difference in kinetochore distribution in the γTUSC^{cc} oxidized strain. However, shorter spindles had kinetochores clustering closer to the poles.

A phosphorylation mutation of Tub4 was selected for study based on mutational studies conducted with human γ-tubulin. In human γ-tubulin, S131 plays an important role in centrosome duplication. It was shown that S131 is phosphorylated by SadB kinase. Phosphomimetic mutations resulted in increased centrosome numbers and phosphoblocking mutations resulted in deficiencies in centrosome duplication (Alvarado-Kristensson *et al.*, 2009). When the corresponding residue, T130, was mutated in yeast Tub4, the dramatic changes in centrosome number were not observed. However, there were subtle changes in spindle morphology. While changes in tubulin distribution were minor, T130A shifted the kinetochore cluster closer to the poles and T130D shifted the kinetochore cluster closer to the spindle midzone. T130 falls on the lateral interface of Tub4, near the exterior surface of the microtubule. On the adjacent Tub4, the residues closest to T130 are R341 and K337. The addition of the phosphate charge in this region may stabilize the lateral interaction between Tub4 molecules, and may promote a closed state, similar to that seen with γTUSC^{cc}. Changes in nucleation activity and microtubule stability may account for the differences observed in kinetochore distributions.

The third group of Tub4 mutants studied here was T239 mutations, chosen because a comparable mutation in β-tubulin (Tub2 in yeast) showed dramatic changes in microtubule dynamics and polymerization. The analogous Tub2 mutation, T238A, was found to possess hyperstable microtubules, both *in vivo* and *in vitro* (Stearns *et al.*, 1990; Machin *et al.*, 1995, 1996; Geyer *et al.*, 2015). This mutation that is buried in the core of the protein, so this mutation most likely does not affect protein interaction interfaces. Previous work has also shown that this mutation is part of a helix that has large conformational changes as the tubulin dimer becomes incorporated into a microtubule (Geyer *et al.*, 2015). *In vivo,* mutation of Tub4 T239 does

appear to dramatically affect the organization of the mitotic spindle. While T239S and T239V do not affect tubulin distribution across the spindle, T239A shows a broadening of the tubulin distribution. The changes seen in kinetochore distributions are subtler, with slight shifts in kinetochore clustering towards the midzone of the spindle. These phenotypes could suggest that microtubules are more stable and longer in mutant strains, pushing the kinetochores further from the spindle pole bodies, and widening the distribution of tubulin throughout the spindle.

Conclusions

This series of mutational analyses of Spc97, Spc98, and Tub4 have provided several insights into regions of the three proteins that are important for the proper regulation of microtubule nucleation. Further work is still needed to fully characterize promising mutants. Specifically, the three temperature sensitive mutants of Spc98 require further attention to ascertain how these mutations affect the γ-tubulin structure and function. Electron microscopy structures of γ-tubulin small complexes expressing these mutations will determine if there are any induced conformational changes. Further fluorescence microscopy experiments can study specific cell cycle states as well as sensitivity to microtubule drugs like benomyl. In addition, further work can be done with the representative lethal mutations to better understand the cause of lethality. Of highest importance would be Spc97 ins207 and Spc98 ins1025 which both localized to the spindle pole body. These results suggest that these two mutants can still be incorporated into the γ-tubulin small complex and can still localize correctly. Therefore, the cause of lethality may be due to nucleation-specific deficiencies. *In vitro* nucleation assays could determine nucleation activity and electron microscopy structures could identify any structural changes to the small complex. In all, this work has produced several mutants that will be useful in future studies of spindle morphology, microtubule nucleation, and γ-tubulin small complex regulation.

Acknowledgements

Development of the linker scanning mutagenesis approach was done in close collaboration with Jerry Tien, published in Tien *et al.*, 2013. Illumina sequencing was performed in collaboration with Maitreya Dunham's and Jay Shendure's labs (Department of Genome Sciences), with primary guidance from Celia Payen and Charlie Lee. Custom programs for Illumina sequencing analysis were provided by Alex Zelter. Deletions and point mutations in Spc98 were designed by Justin Kollman. Point mutations in Tub4 were proposed by Justin Kollman and Luke Rice. The γTUSC^{cc} *in vivo* analysis was published in Kollman *et al.*, 2015.

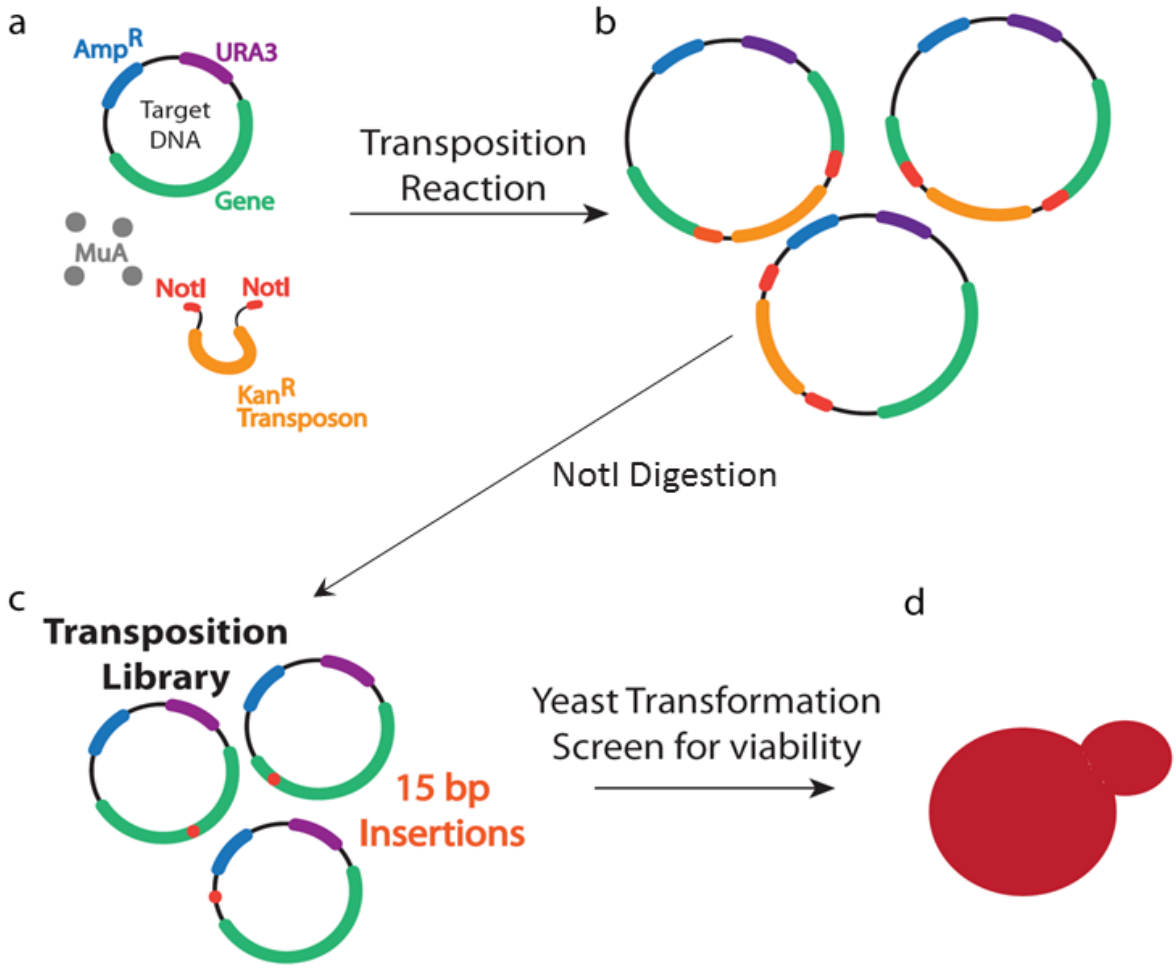

Figure 3.1. Linker scanning mutagenesis.
a. The *in vitro* transposition reaction incubates the target DNA with the transposon and the MuA transposase. b. The results of this reaction are plasmids with the transposon inserted randomly throughout the sequence. Digestion with *NotI* cleaves on either side of the transposon, removing it from the plasmid. c. The resulting plasmids can be isolated on an agarose gel and re-ligated, leaving only a fifteen base pair insertion, including the *NotI* restriction site, where the transposon was inserted. These plasmids are the Transposition Library, which are then d. transformed into yeast to screen for viability.

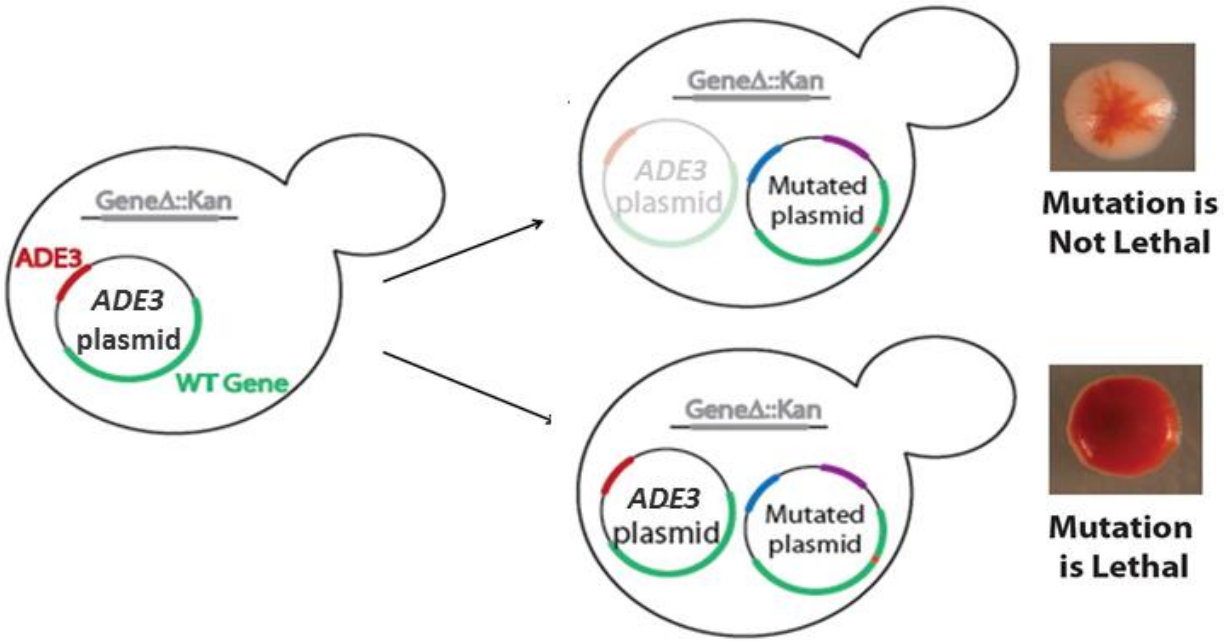

Figure 3.2. Yeast red/white screen.
Strains have the genomic copy of the gene of interest deleted (shown in grey). The *ADE3* plasmid contains a wild type copy of the gene (shown in green) and the *ADE3* gene (shown in red). The mutant library is transformed into the yeast strain. The mutant library plasmids contain the gene (shown in green), ampicillin resistance (shown in blue) and *URA3* (shown in purple) for selection in yeast. There is a small insertion (shown in orange) randomly throughout the plasmid. If the mutated plasmid encodes a viable allele, the *ADE3* plasmid is extraneous. Cells stochastically lose the *ADE3* plasmids remain viable, leading to a sectored colony (top right). If the mutated plasmid encodes a lethal allele, the *ADE3* plasmid expressing the wild type copy of the gene is maintained and the yeast colonies are red (bottom right).

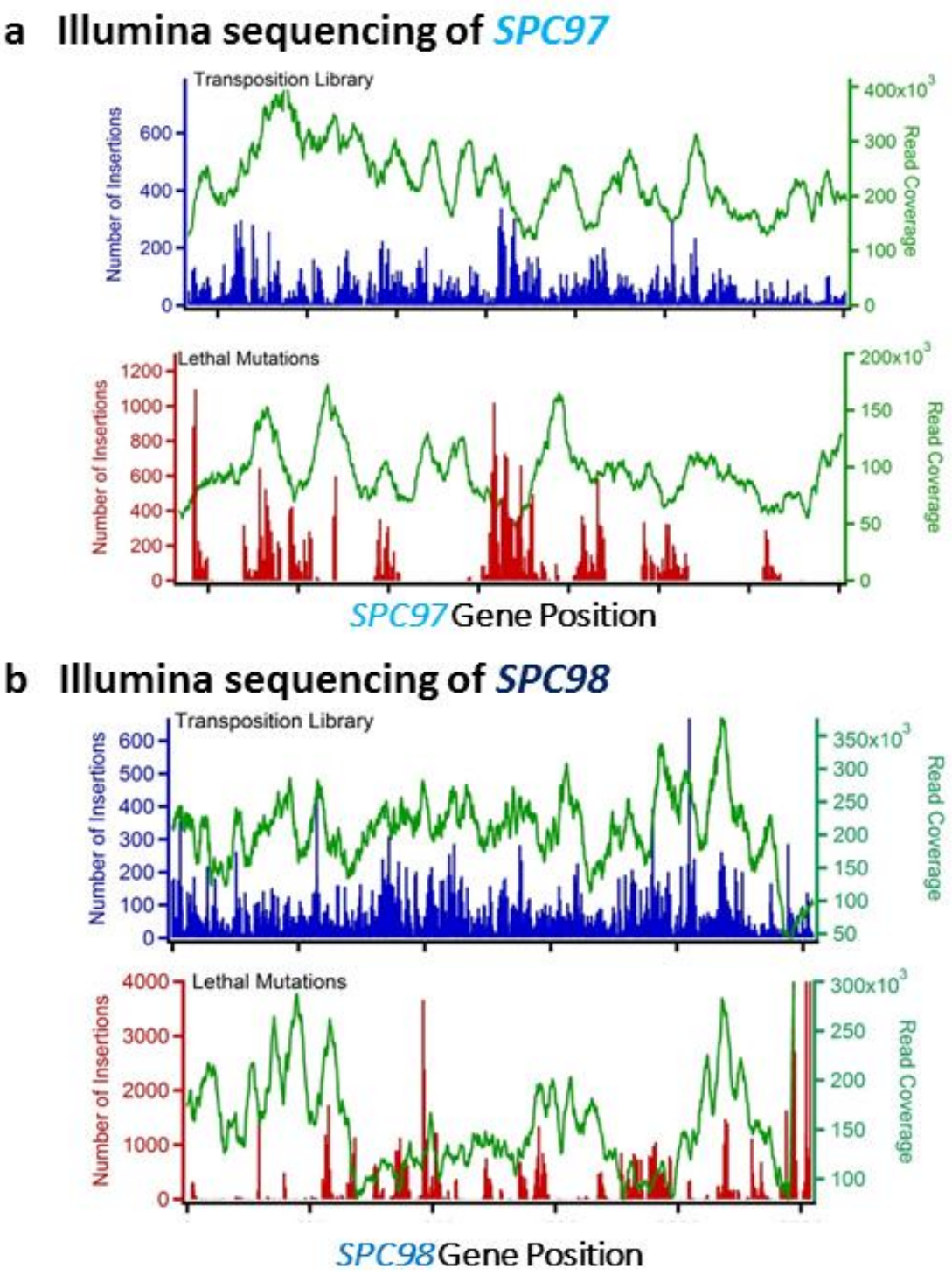

Figure 3.3. Illumina sequencing of transposition library and lethal mutations.
The initial transposition libraries, shown in blue, and the pools of lethal mutations, shown in red, for both a. *SPC97* and b. *SPC98* were sequenced using the Illumina platform. Green traces show read coverage for each sample.

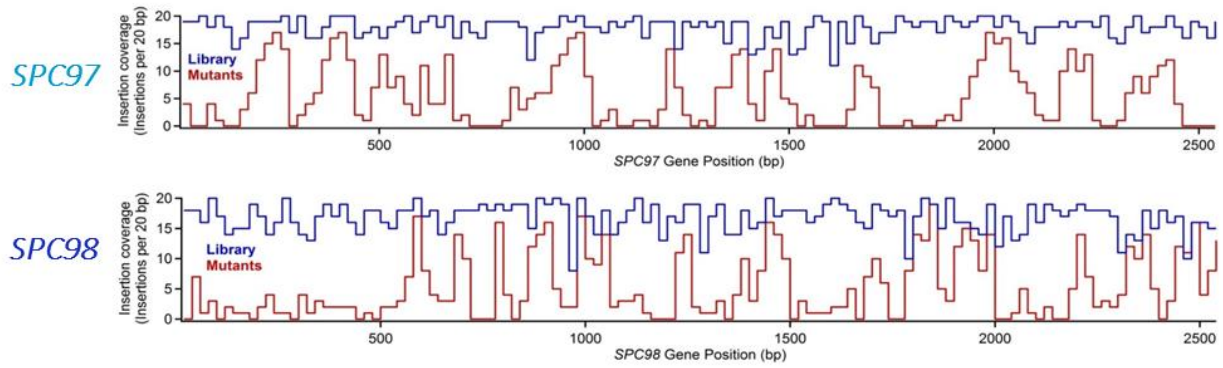

Figure 3.4. Density of insertion sites.
The density of insertions in twenty base pair windows reveal regions of the gene that were represented similarly in the transposition libraries (in blue) and the lethal mutations (in red) for both *SPC97* and *SPC98*.

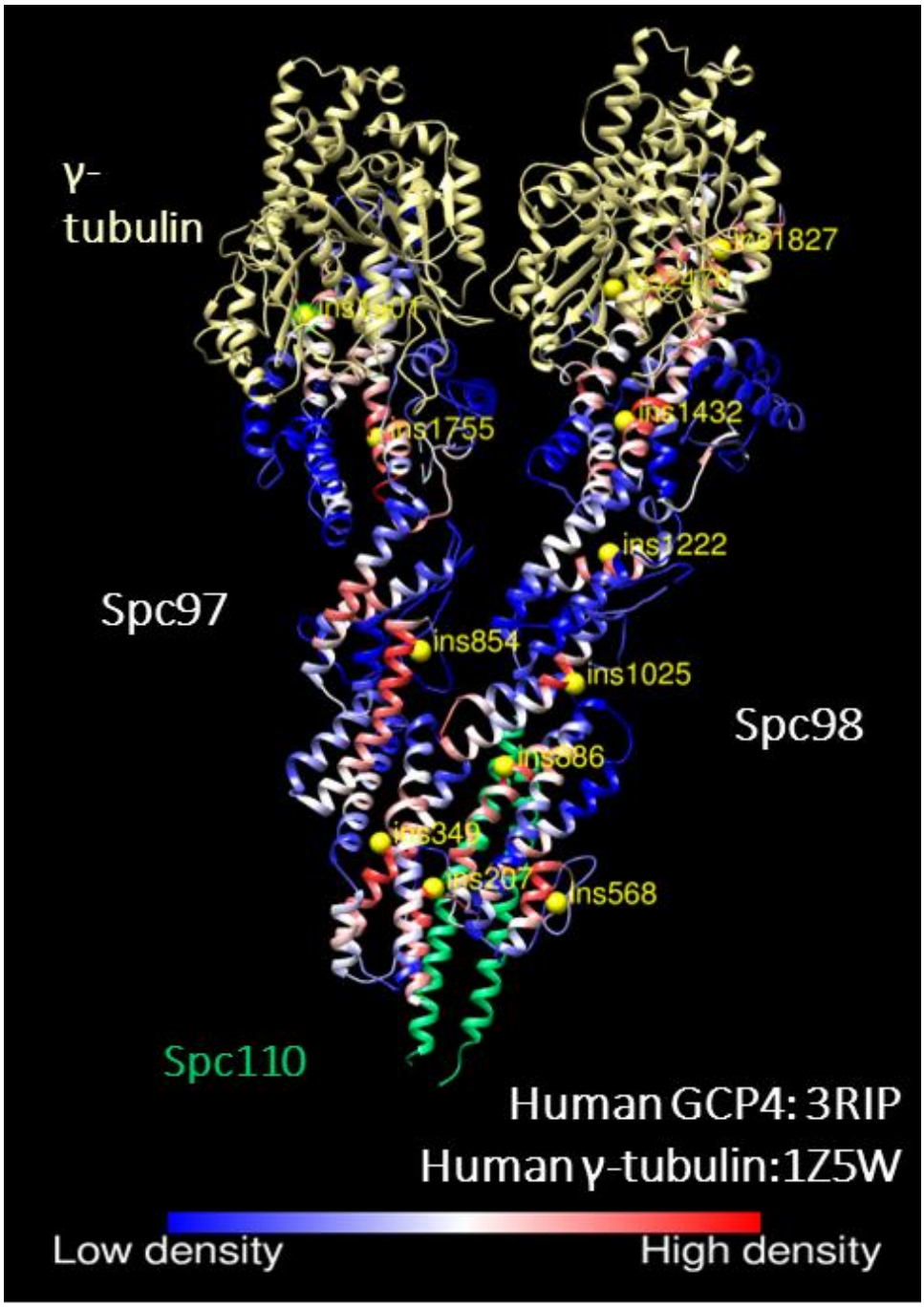

Figure 3.5. Density of lethal insertion sites mapped onto a pseudo-atomic model of the yeast γ-tubulin small complex.
Regions of the proteins with low density of lethal insertions are shaded blue while regions with high density of lethal insertions are shaded red. Five representative lethal mutations were chosen in Spc97. Seven representative lethal mutations were chosen in Spc98. Yellow spheres indicate representative lethal insertions selected for analysis. γ-tubulin structure adapted from Aldaz *et al.*, 2005; GCP4 structure adapted from Guillet *et al.*, 2011.

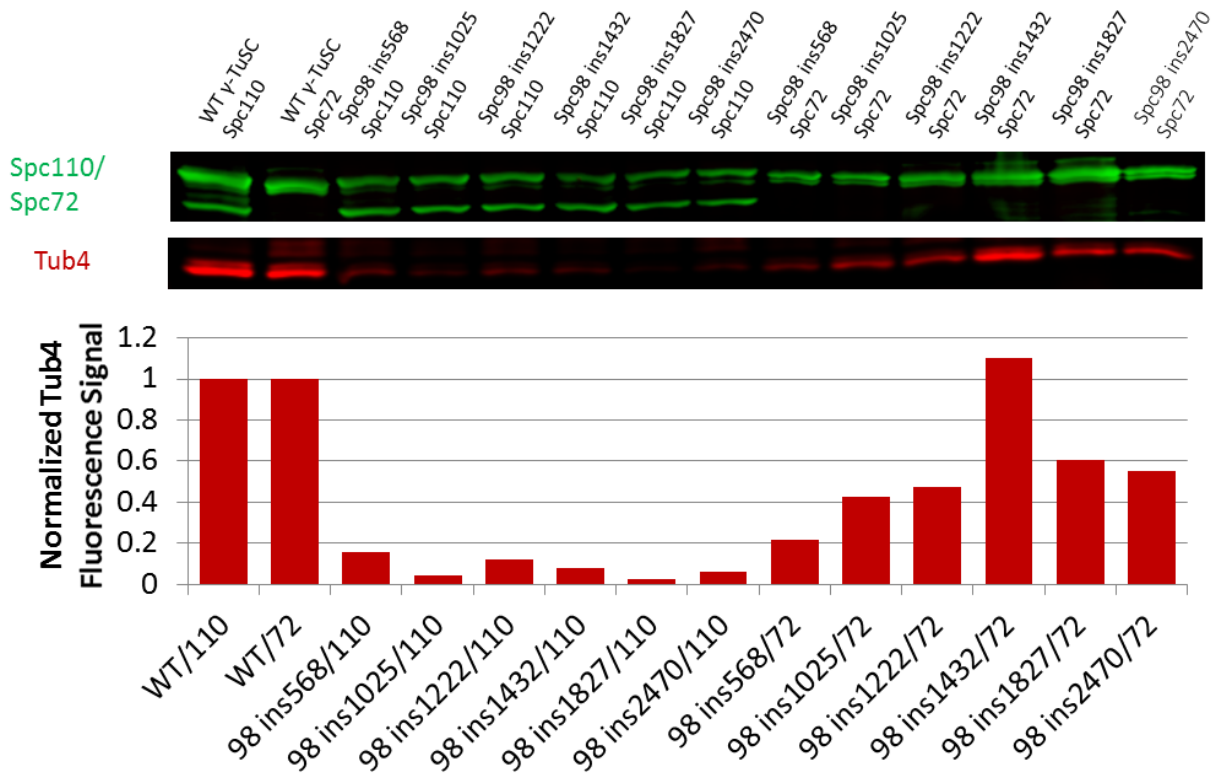

Figure 3.6. Spc98 lethal mutants do not form stable γ-tubulin small complexes with Spc110.
Small complexes were co-expressed in insect cells and purified with Spc110 or Spc72. The fluorescence intensities of the lethal mutant complexes were normalized to the corresponding wild type control.

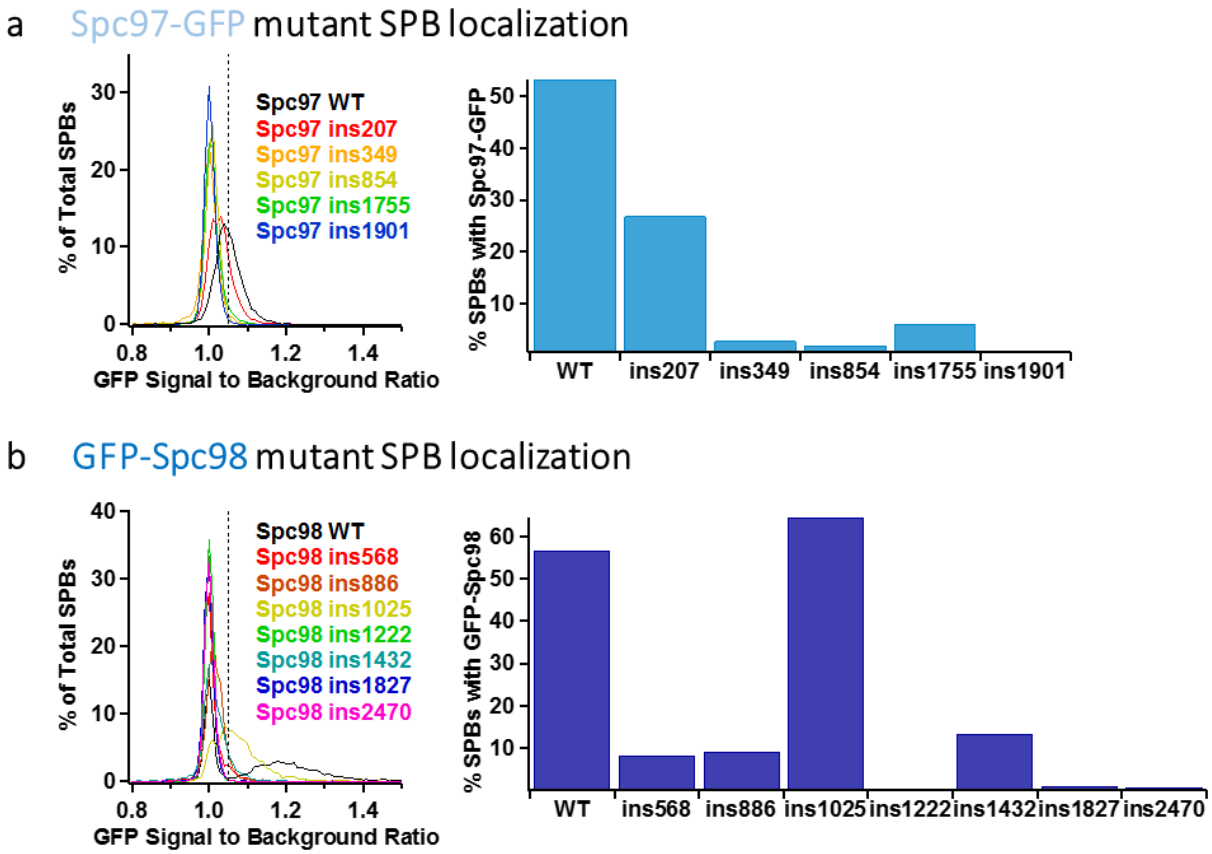

Figure 3.7. Two lethal mutants localize to the spindle pole body.
GFP-tagged lethal mutant proteins were integrated into strains with Spc42-mCherry. Localization of the mutant γ-tubulin small complex to the spindle pole body was determined by measuring GFP fluorescence intensity at mCherry spindle pole body foci. The percent of spindle pole bodies containing GFP-tagged mutants was determined by a signal to noise threshold of 1.05.

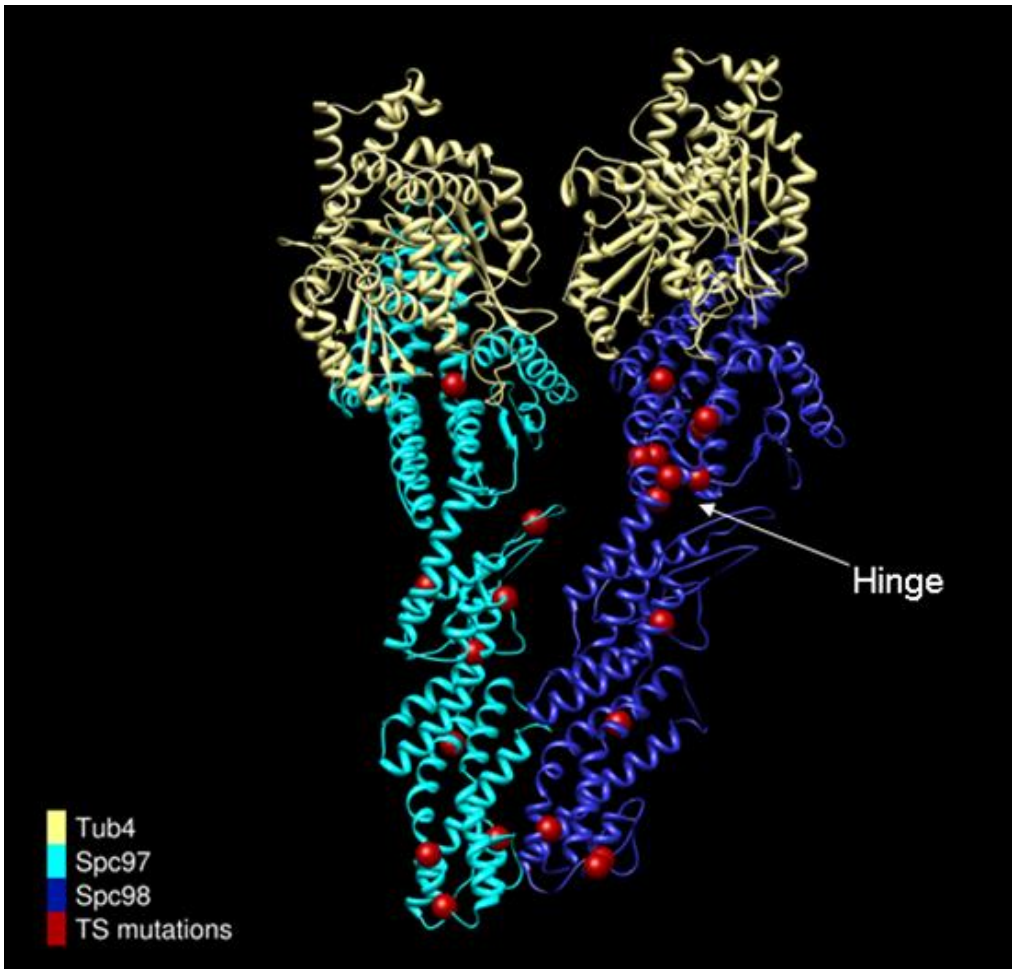

Figure 3.8. Temperature sensitive mutants.
Temperature sensitive mutations (in red) have been mapped onto the pseudo-atomic structures of Spc97 and Spc98 as approximated by the crystal structure of GCP4. The observed hinge in Spc98 is indicated by an arrow. γ-tubulin structure adapted from Aldaz *et al.*, 2005; GCP4 structure adapted from Guillet *et al.*, 2011.

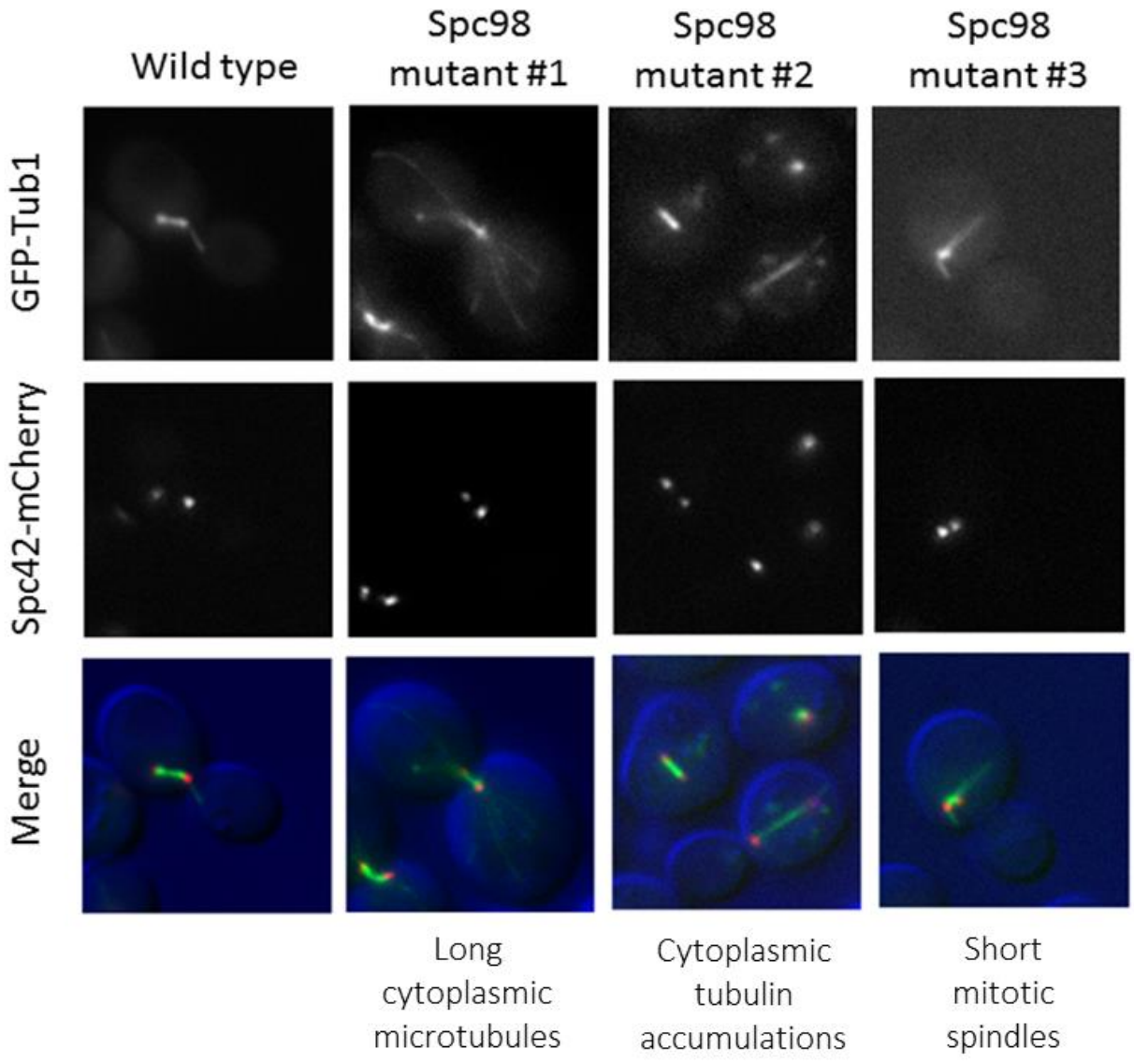

Figure 3.9. Temperature sensitive phenotypes.
Temperature sensitive alleles were isolated from three Spc98 strains and integrated into fluorescent strains containing markers for the spindle pole bodies (Spc42-mCherry, in red) and microtubules (GFP-Tub1, in green). Spc98 mutant #1: ins35; increase in the number, intensity and length of cytoplasmic microtubules. Spc98 mutant #2: ins561; cytoplasmic accumulations of tubulin. Spc98 mutant #3: ins557; short metaphase spindles.

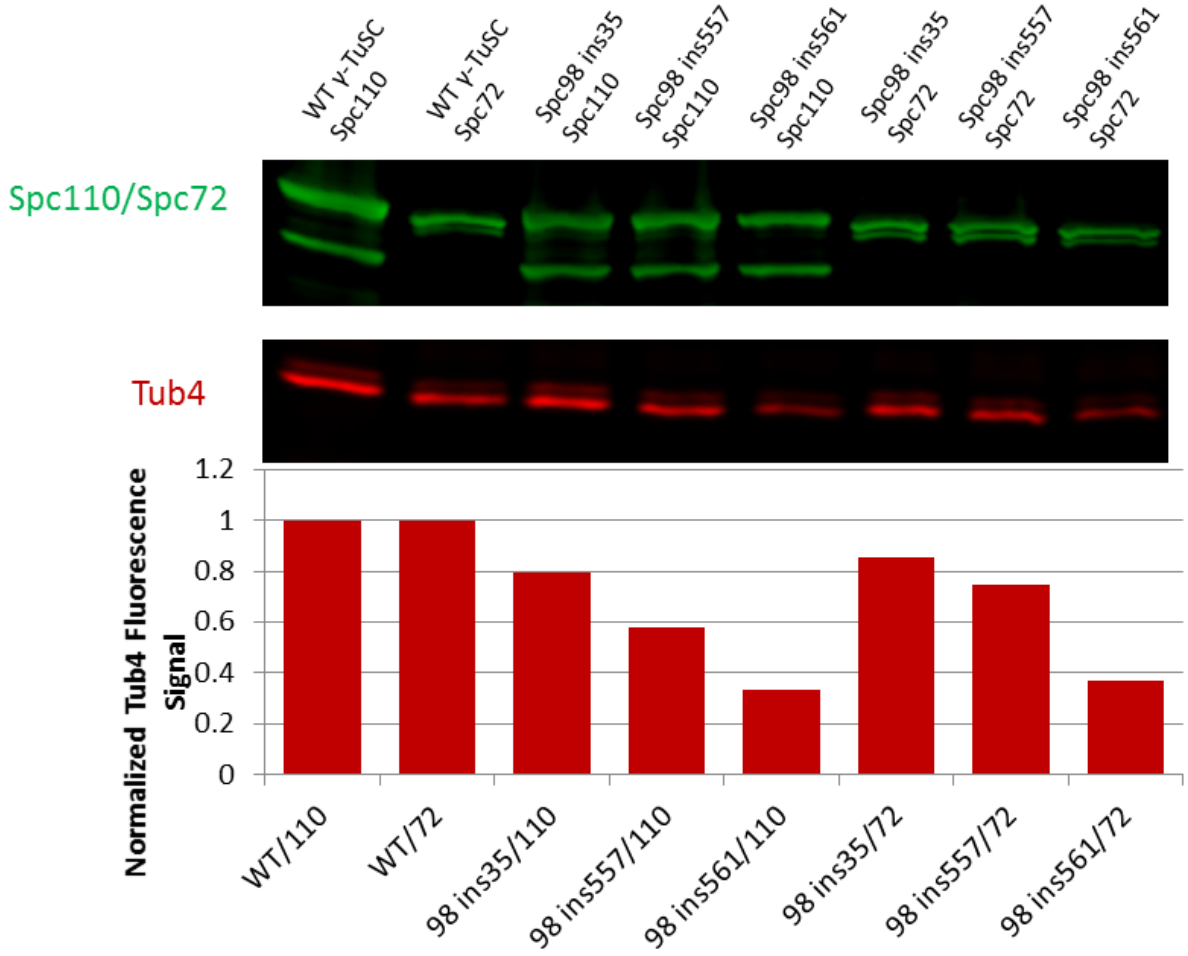

Figure 3.10. Spc98 temperature sensitive mutants purified from insect cells form less stable γ-tubulin small complexes.
Small complexes were co-expressed in insect cells and purified with Spc110 or Spc72. The fluorescence intensities of the temperature sensitive mutant complexes were normalized to the corresponding wild type control.

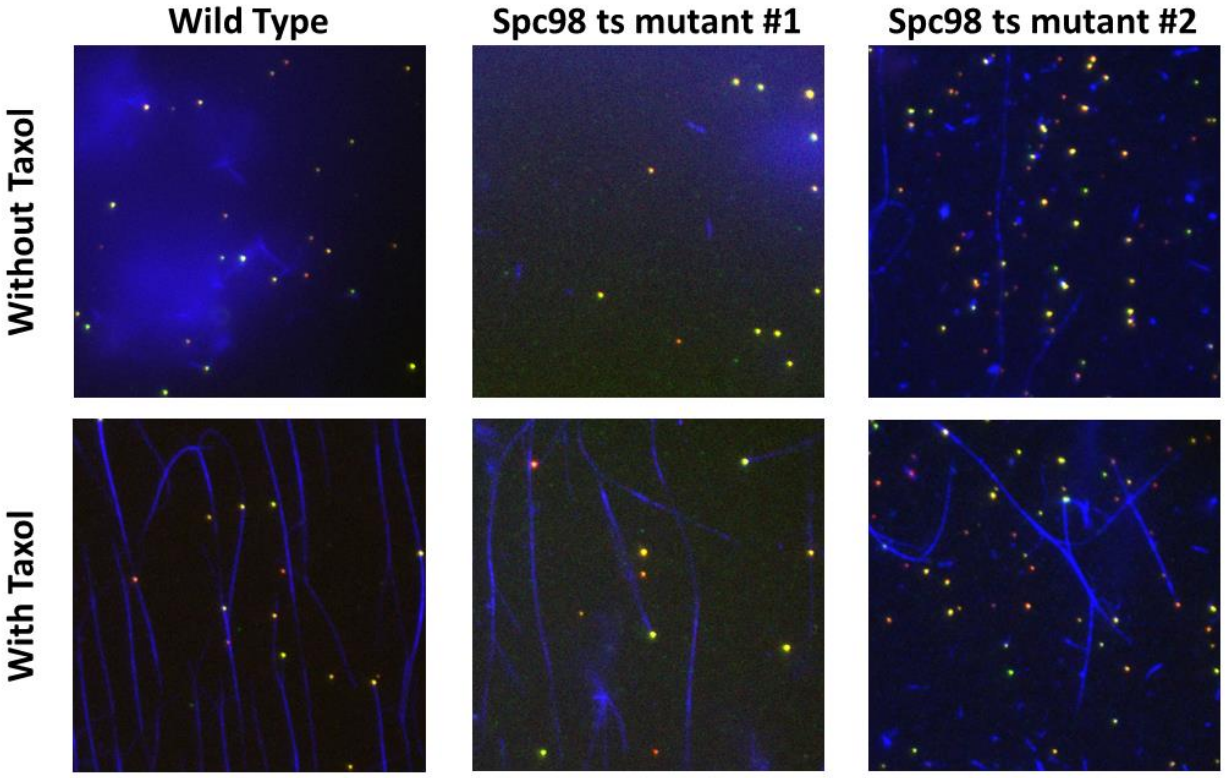

Figure 3.11. Nucleation assays with Spc98 temperature sensitive mutants.
Spindle pole bodies, tagged with Spc42-mCherry (in red) and Tub4-GFP (in green) were purified for *in vitro* nucleation assays. Alexa647-labeled tubulin (in blue) was allowed to nucleate off of spindle pole bodies either in the presence or absence of stabilizing taxol.

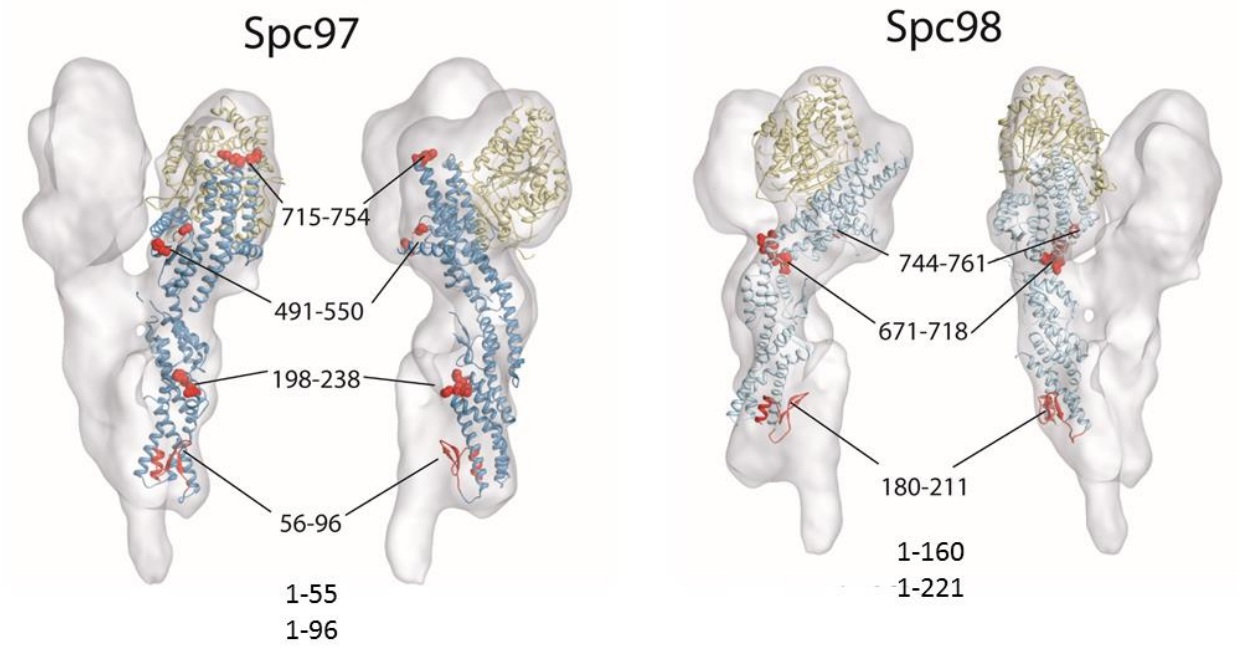

Figure 3.12. Internal deletions of Spc97 and Spc98.
Internal deletions were designed to investigate the regions of Spc97 and Spc98 that were not approximated by the crystal structure of GCP4. Figure adapted from Justin Kollman.

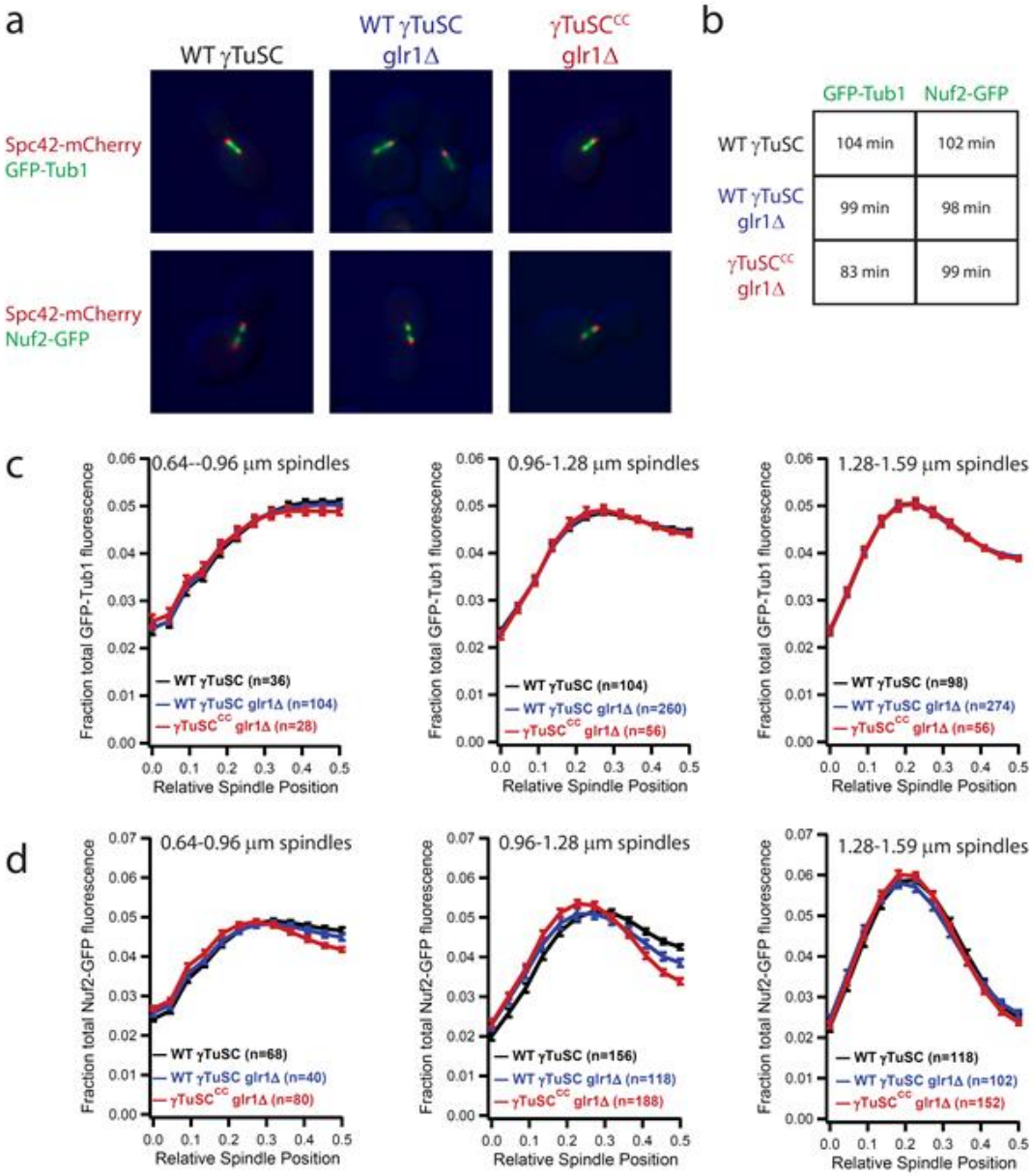

Figure 3.13. γTuSC^{CC} does not affect cell viability.
a. Representative images of WT, *glr1*Δ, and γTuSC^{CC} *glr1*Δ fluorescent strains. Cells in the top row have the spindle pole bodies marked by Spc42-mCherry and the microtubules marked by GFP-Tub1. Cells in the bottom row have the spindle pole bodies marked by Spc42- mCherry and the kinetochores marked by Nuf2-GFP. b. The doubling times of WT and γTuSCCC strains. c. Average GFP-Tub1 fluorescence distributions show that γTuSC^{CC} has no effect on tubulin distribution across three spindle length classifications. d. Average Nuf2-GFP fluorescence distributions show that γTuSC^{CC} has no effect on kinetochore clustering in metaphase spindles (1.28- 1.59 μm), while shorter spindles show kinetochores cluster slightly closer to the spindle pole bodies. Error bars represent the standard error of the mean. From Kollman *et al.*, 2015.

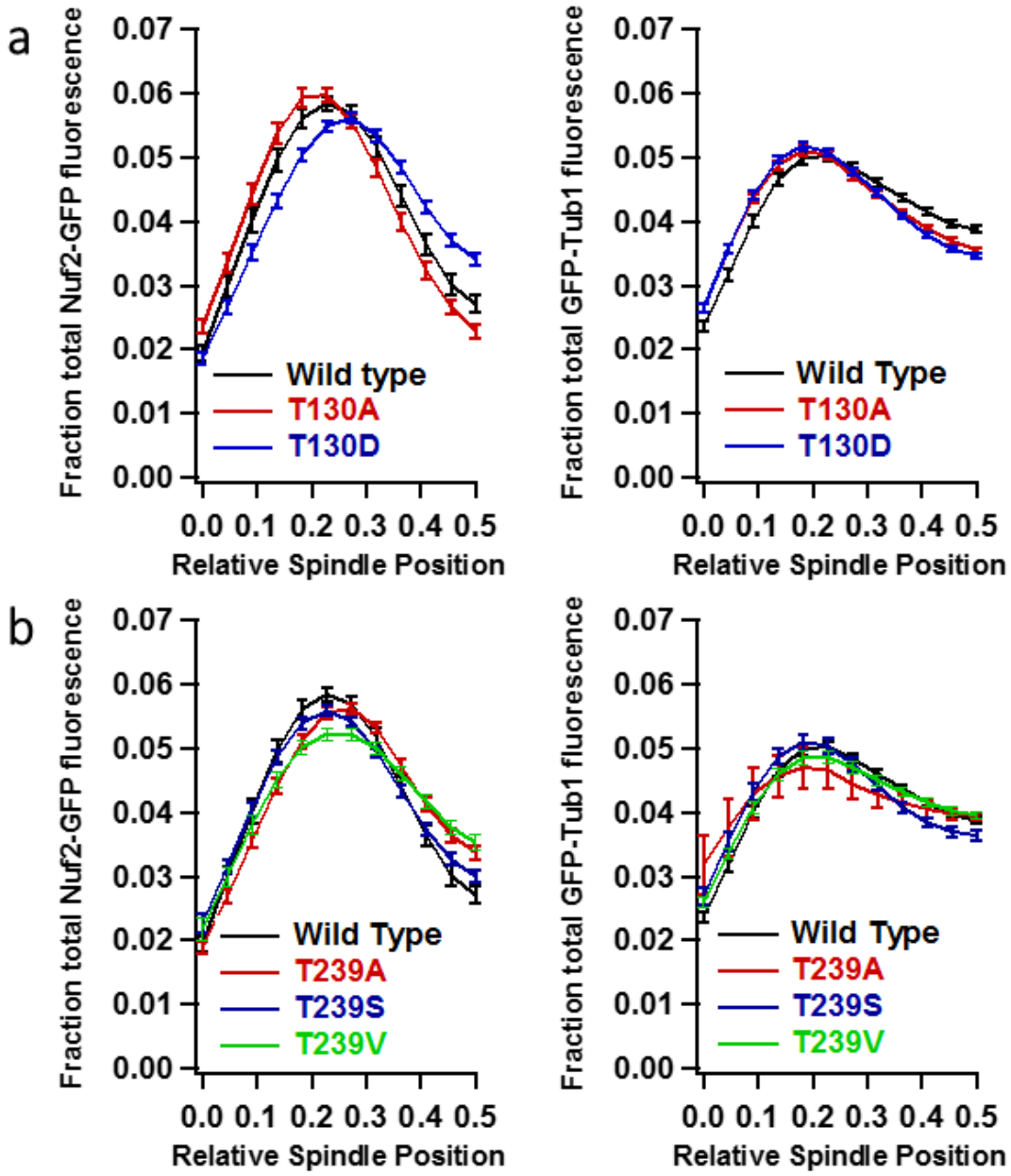

Figure 3.14. Fluorescence analysis of Tub4 mutations.
a. Average Nuf2-GFP and GFP-Tub1 fluorescence distributions show T130A and T130D affect kinetochore distribution across metaphase spindles (20-25 pixels). b. Average Nuf2-GFP and GFP-Tub1 fluorescence distributions show T239A, T239S, and T239V affect kinetochore distribution and tubulin distribution across metaphase spindles (20-25 pixels). Error bars represent the standard error of the mean.

Table 3.1. Strains used in this study.

Strain	Genotype	Reference
W303	*ade2-1oc can1-100 his3-11,15 leu2-3,112 trp1-1 ura3-1*	
BGY56-2C	*MATa ade3Δ-100 lys2Δ::HIS3 tub4Δ::kanMX* pLA6	Beth Graczyk
BGY63-5C	*MATa ade3Δ-100 lys2Δ::HIS3 tub4Δ::kanMX NUF2-GFP::HISMX SPC110-mCherry::hphMX* pLA6	Beth Graczyk
HSY2-1C	*MAT@ ade3Δ-100 lys2Δ::HIS3 spc110Δ::TRP1* pHS26	Geiser *et al.*, 1993
KFY5-5A	*MATa ade3Δ-100 lys2Δ::HIS3 spc98Δ::kanMX* pKF12	This study
KFY14-18C	*MATa ade3Δ-100 LEU2::GFP-TUB1 lys2Δ::HIS3 SPC110-mCherry::hphMX tub4Δ::kanMX* pLA6	This study
KFY16	*MATa ade3Δ-100 lys2Δ::HIS3 spc98(M404R/D722A)*	This study
KFY36-13C	MATα ade3Δ-100 LEU2::GFP-TUB1 lys2Δ::HIS3 SPC42-mCherry::hphMX	This study
KFY37-4C	*MATa ade3Δ-100 LEU2::GFP-TUB1 lys2Δ::HIS3 SPC42-mCherry::hphMX spc98Δ::kanMX* pKF12	This study
KFY38-5C	*MATa ade3Δ-100 LEU2::GFP-TUB1 lys2Δ:: SPC42-mCherry::hphMX spc97Δ::TRP1* pTN25	This study
KFY42-1C	*MATa ade3Δ-100 LEU2::GFP-TUB1 lys2Δ::HIS3 glr1Δ::TRP1 SPC42-mCherry::hphMX*	This study
KFY43	*MATa ade3Δ-100 lys2Δ::HIS3 NUF2-GFP::HISMX SPC110-mCherry::hphMX tub4(T130A)*	This study
KFY44	*MATa ade3Δ-100 LEU2::GFP-TUB1 lys2Δ::HIS3 SPC110-mCherry::hphMX tub4(T130A)*	This study
KFY45	*MATa ade3Δ-100 lys2Δ::HIS3 NUF2-GFP::HISMX SPC110-mCherry::hphMX tub4(T130D)*	This study
KFY46	*MATa ade3Δ-100 LEU2::GFP-TUB1 lys2Δ::HIS3 SPC110-mCherry::hphMX tub4(T130D)*	This study
KFY47	*MATa ade3Δ-100 LEU2::GFP-TUB1 lys2Δ::HIS3 SPC42-mCherry::hphMX ins35 spc98*	This study
KFY48	*MATa ade3Δ-100 LEU2::GFP-TUB1 lys2Δ::HIS3 SPC42-mCherry::hphMX ins557 spc98*	This study
KFY49	*MATa ade3Δ-100 LEU2::GFP-TUB1 lys2Δ::HIS3 SPC42-mCherry::hphMX ins561 spc98*	This study
KFY50	*MATa ade3Δ-100 LEU2::GFP-TUB1 lys2Δ::HIS3 SPC42-mCherry::hphMX ins573 spc98*	This study
KFY51	*MATa ade3Δ-100 LEU2::GFP-TUB1 lys2Δ::HIS3 SPC42-mCherry::hphMX ins769 spc98*	This study
KFY52	*MATa ade3Δ-100 LEU2::GFP-TUB1 lys2Δ::HIS3 SPC42-mCherry::hphMX ins848 spc98*	This study
KFY53	*MATa ade3Δ-100 LEU2::GFP-TUB1 lys2Δ::HIS3 SPC42-mCherry::hphMX ins1033 spc98*	This study

KFY54	*MATa ade3Δ-100 LEU2::GFP-TUB1 lys2Δ::HIS3 SPC42-mCherry::hphMX ins1035 spc98*	This study
KFY55	*MATa ade3Δ-100 LEU2::GFP-TUB1 lys2Δ::HIS3 SPC42-mCherry::hphMX ins1038 spc98*	This study
KFY56	*MATa ade3Δ-100 LEU2::GFP-TUB1 lys2Δ::HIS3 SPC42-mCherry::hphMX ins1384 spc98*	This study
KFY57	*MATa ade3Δ-100 LEU2::GFP-TUB1 lys2Δ::HIS3 SPC42-mCherry::hphMX ins1415 spc98*	This study
KFY58	*MATa ade3Δ-100 LEU2::GFP-TUB1 lys2Δ::HIS3 SPC42-mCherry::hphMX ins1421 spc98*	This study
KFY59	*MATa ade3Δ-100 LEU2::GFP-TUB1 lys2Δ::HIS3 SPC42-mCherry::hphMX ins1713 spc98*	This study
KFY60	*MATa ade3Δ-100 LEU2::GFP-TUB1 lys2Δ::HIS3 SPC42-mCherry::hphMX ins1974 spc98*	This study
KFY61	*MATa ade3Δ-100 LEU2::GFP-TUB1 lys2Δ::HIS3 SPC42-mCherry::hphMX ins2180 spc98*	This study
KFY62	*MATa ade3Δ-100 LEU2::GFP-TUB1 lys2Δ::HIS3 SPC42-mCherry::hphMX ins2181 spc98*	This study
KFY63	*MATa ade3Δ-100 LEU2::GFP-TUB1 lys2Δ::HIS3 SPC42-mCherry::hphMX ins2182 spc98*	This study
KFY64	*MATa ade3Δ-100 LEU2::GFP-TUB1 lys2Δ::HIS3 SPC42-mCherry::hphMX ins2187 spc98*	This study
KFY65	*MATa ade3Δ-100 LEU2::GFP-TUB1 lys2Δ::HIS3 SPC42-mCherry::hphMX ins2278 spc98*	This study
KFY66	*MATa ade3Δ-100 LEU2::GFP-TUB1 lys2Δ::HIS3 SPC42-mCherry::hphMX spc98(M404R/D722A)*	This study
KFY67	*MATa ade3Δ-100 LEU2::GFP-TUB1 lys2Δ::HIS3 SPC42-mCherry::hphMX spc98(K414A)*	This study
KFY68	*MATa ade3Δ-100 LEU2::GFP-TUB1 lys2Δ::HIS3 SPC42-mCherry::hphMX spc98(V457N/N720A/D722A)*	This study
KFY69	*MATa ade3Δ-100 LEU2::GFP-TUB1 lys2Δ::HIS3 SPC42-mCherry::hphMX spc98(N720A)*	This study
KFY70	*MATa ade3Δ-100 LEU2::GFP-TUB1 lys2Δ::HIS3 SPC42-mCherry::hphMX spc98(D722A)*	This study
KFY71	*MATa ade3Δ-100 LEU2::GFP-TUB1 lys2Δ::HIS3 SPC42-mCherry::hphMX spc98(V457N)*	This study
KFY72	*MATa ade3Δ-100 LEU2::GFP-TUB1 lys2Δ::HIS3 SPC42-mCherry::hphMX spc98(M404R)*	This study
KFY73	*MATa ade3Δ-100 LEU2::GFP-TUB1 lys2Δ::HIS3 SPC42-mCherry::hphMX spc98(K417A/E418E/Q420A/N423A/E424A)*	This study
KFY74	*MATa ade3Δ-100 LEU2::GFP-TUB1 lys2Δ::HIS3 SPC42-mCherry::hphMX spc98(N423A/E424A)*	This study
KFY91	*MATa ade3Δ-100 LEU2::GFP-TUB1 lys2Δ::HIS3 glr1Δ::TRP1 SPC42-mCherry::hphMX tub4(S58C/G288C)*	This study

KFY135-8B	*MATa ade3Δ-100 lys2Δ::HIS3 tub4(S58C/G288C)::URA3 glr1Δ::TRP1 SPC42-mCherry::hphMX NUF2-GFP::kanMX*	This study
KFY138-5A	*MATa ade3Δ-100 NUF2-GFP::kanMX SPC42-mCherry::hphMX*	This study
KFY177-30B	*MATa ade3Δ-100 SPC42-mCherry::hphMX SPC97-TAP::kanMX ins35 spc98 TUB4-GFP::kanMX*	This study
KFY179-53D	*MATa ade3Δ-100 SPC42-mCherry::hphMX SPC97-TAP::kanMX ins561 spc98 TUB4-GFP::kanMX*	This study
KFY220-1A	*MATα ade3Δ-100 LEU2::GFP-TUB1 lys2Δ::HIS3 SPC42-mCherry::hphMX tub4Δ::kanMX* pLA6	This study
KFY241	*MATa ade3Δ-100 SPC42-mCherry::hphMX URA3::SPC97-GFP*	This study
KFY242	*MATa ade3Δ-100 SPC42-mCherry::hphMX URA3::ins207 spc97-GFP*	This study
KFY243	*MATa ade3Δ-100 SPC42-mCherry::hphMX URA3::ins349 spc97-GFP*	This study
KFY244	*MATa ade3Δ-100 SPC42-mCherry::hphMX URA3::ins854 spc97-GFP*	This study
KFY245	*MATa ade3Δ-100 SPC42-mCherry::hphMX URA3::ins1755 spc97-GFP*	This study
KFY246	*MATa ade3Δ-100 SPC42-mCherry::hphMX URA3::ins1901 spc97-GFP*	This study
KFY248	*MATa ade3Δ-100 SPC42-mCherry::hphMX URA3::GFP-SPC98*	This study
KFY249	*MATa ade3Δ-100 SPC42-mCherry::hphMX URA3::GFP-ins568 spc98*	This study
KFY250	*MATa ade3Δ-100 SPC42-mCherry::hphMX URA3::GFP-ins886 spc98*	This study
KFY251	*MATa ade3Δ-100 SPC42-mCherry::hphMX URA3::GFP-ins1025 spc98*	This study
KFY252	*MATa ade3Δ-100 SPC42-mCherry::hphMX URA3::GFP-ins1222 spc98*	This study
KFY253	*MATa ade3Δ-100 SPC42-mCherry::hphMX URA3::GFP-ins1432 spc98*	This study
KFY254	*MATa ade3Δ-100 SPC42-mCherry::hphMX URA3::GFP-ins1827 spc98*	This study
KFY255	*MATa ade3Δ-100 SPC42-mCherry::hphMX URA3::GFP-ins2470 spc98*	This study
KFY256	*MATa ade3Δ-100 PaPreCa-SPC98 URA3::SPC97-GFP*	This study
KFY257	*MATa ade3Δ-100 PaPreCa-SPC98 URA3::ins207 spc97-GFP*	This study
KFY258	*MATa ade3Δ-100 PaPreCa-SPC98 URA3::ins359 spc97-GFP*	This study
KFY259	*MATa ade3Δ-100 PaPreCa-SPC98 URA3::ins854 spc97-GFP*	This study

KFY260	*MATa ade3Δ-100 PaPreCa-SPC98 URA3::ins1755 spc97-GFP*	This study
KFY261	*MATa ade3Δ-100 PaPreCa-SPC98 URA3::ins1901 spc97-GFP*	This study
KFY262	*MATa ade3Δ-100 SPC42-mCherry::hphMX SPC97-TAP::kanMX URA3::GFP-SPC98*	This study
KFY263	*MATa ade3Δ-100 SPC42-mCherry::hphMX SPC97-TAP::kanMX URA3::GFP-ins568 spc98*	This study
KFY264	*MATa ade3Δ-100 SPC42-mCherry::hphMX SPC97-TAP::kanMX URA3::GFP-ins886 spc98*	This study
KFY265	*MATa ade3Δ-100 SPC42-mCherry::hphMX SPC97-TAP::kanMX URA3::GFP-ins1025 spc98*	This study
KFY266	*MATa ade3Δ-100 SPC42-mCherry::hphMX SPC97-TAP::kanMX URA3::GFP-ins1222 spc98*	This study
KFY267	*MATa ade3Δ-100 SPC42-mCherry::hphMX SPC97-TAP::kanMX URA3::GFP-ins1432 spc98*	This study
KFY268	*MATa ade3Δ-100 SPC42-mCherry::hphMX SPC97-TAP::kanMX URA3::GFP-ins1827 spc98*	This study
KFY269	*MATa ade3Δ-100 SPC42-mCherry::hphMX SPC97-TAP::kanMX URA3::GFP-ins2470 spc98*	This study
KFY270	*MATa ade3Δ-100 lys2Δ::HIS3 NUF2-GFP::HIS SPC110-mCherry::hphMX tub4(T239A)::URA3*	This study
KFY271	*MATa ade3Δ-100 lys2Δ::HIS3 NUF2-GFP::HIS SPC110-mCherry::hphMX tub4(T239S)::URA3*	This study
KFY272	*MATa ade3Δ-100 lys2Δ::HIS3 NUF2-GFP::HIS SPC110-mCherry::hphMX tub4(T239V)::URA3*	This study
KFY273	*MATa ade3Δ-100 LEU2::GFP-TUB1 lys2Δ::HIS3 SPC110-mCherry::hphMX tub4(T239A)::URA3*	This study
KFY274	*MATa ade3Δ-100 LEU2::GFP-TUB1 lys2Δ::HIS3 SPC110-mCherry::hphMX tub4(T239S)::URA3*	This study
KFY275	*MATa ade3Δ-100 LEU2::GFP-TUB1 lys2Δ::HIS3 SPC110-mCherry::hphMX tub4(T239V)::URA3*	This study
TNY65-2B	*MATa ade3Δ-100 lys2Δ::HIS3 spc97Δ::TRP1* pTN25	Thu Nguyen

Table 3.2. Plasmids used in the study.

Plasmid	Relevant Markers	Reference
pRS315	*CEN6 ARSH4 LEU2 Amp^r* f1 origin	Sikorski and Hieter, 1989
pRS316	*CEN6 ARSH4 URA3 Amp^r* f1 origin	Sikorski and Hieter, 1989
pRS306	*URA3* f1 origin	Sikorski and Hieter, 1989
pFastBac		Invitrogen™
pFA6a-GFP(S65T)-kanMX6	*GFP(S65T) Kan^r*	Bähler *et al.*, 1998
pAZ37	*TUB4* in pFastBac	Vinh *et al.*, 2000
pAZ136	*ins35 spc98* in pFastBac	Alex Zelter
pAZ137	*ins557 spc98* in pFastBac	Alex Zelter
pAZ138	*ins561 spc98* in pFastBac	Alex Zelter
pAZ142	*SPC72-SPC110-GST* in pFastBac	Alex Zelter
pDV36	*SPC98* in pFastBac	Vinh *et al.*, 2000
pDV41	*CMD1* in pFastBac	Vinh *et al.*, 2000
pDV44	*SPC110-GST* in pFastBac	Vinh *et al.*, 2000
pDV45	*SPC97* in pFastBac	Vinh *et al.*, 2000
pHS26	*SPC110 ADE3 LYS2* 2μm origin	Geiser *et al.*, 1993
pKF8	*spc97(1-55Δ)* in pRS316	This study
pKF9	*spc97(1-96Δ)* in pRS316	This study
pKF12	*SPC98 ADE3 LYS2* 2μm origin	This study
pKF17	*spc97(491-550Δ)* in pRS316	This study
pKF22	*spc97(714-754Δ)* in pRS316	This study
pKF28	*spc97(198-238Δ)* in pRS316	This study
pKF29	*spc98(1-221Δ)* in pRS316	This study
pKF30	*spc98(1-160Δ)* in pRS316	This study
pKF31	*spc98(671-718Δ)* in pRS316	This study
pKF32	*spc98(744-761Δ)* in pRS316	This study
pKF33	*SPC98* in pRS306	This study
pKF35	*SPC98* in pRS316	This study
pKF36	*spc98(M404R/D722A)* in pRS316	This study
pKF37	*spc98(K414A)* in pRS316	This study
pKF38	*spc98(V457N/N720A/D722A)* in pRS316	This study
pKF39	*spc98(N720A)* in pRS316	This study
pKF40	*spc98(D722A)* in pRS316	This study
pKF41	*spc98(V457N)* in pRS316	This study
pKF42	*spc98(M404R)* in pRS316	This study
pKF43	*spc98(M404R/D722A)* in pRS306	This study
pKF44	*spc98(K414A)* in pRS306	This study

pKF45	*spc98(V457N/N720A/D722A)* in pRS306	This study
pKF46	*spc98(N720A)* in pRS306	This study
pKF47	*spc98(D722A)* in pRS306	This study
pKF48	*spc98(V457N)* in pRS306	This study
pKF49	*spc98(M404R)* in pRS306	This study
pKF50	*spc97(491-550Δ)* in pRS306	This study
pKF51	*spc97(198-238Δ)* in pRS306	This study
pKF52	*spc110(E16A/F17A/T18A/P19A)* in pRS316	This study
pKF53	*spc110(E16A/F17A/T18E/P19A)* in pRS316	This study
pKF56	*SPC97* in pRS316	This study
pKF57	*spc98(1-160Δ)* in pRS306	This study
pKF58	*spc98(1-221Δ)* in pRS306	This study
pKF59	*spc110(E16A/F17A/T18A/P19A)* in pRS306	This study
pKF60	*spc110(E16A/F17A/T18E/P19A)* in pRS306	This study
pKF76	*tub4(T130A)* in pRS306	This study
pKF77	*tub4(T130D)* in pRS306	This study
pKF78	*spc98(K417A/E418A/Q420A/N423A/E424A)* in pRS316	This study
pKF99	*ins35 spc98* in pRS306	This study
pKF100	*ins557 spc98* in pRS306	This study
pKF101	*ins561 spc98* in pRS306	This study
pKF102	*ins573 spc98* in pRS306	This study
pKF103	*ins769 spc98* in pRS306	This study
pKF104	*ins848 spc98* in pRS306	This study
pKF105	*ins1033 spc98* in pRS306	This study
pKF106	*ins1035 spc98* in pRS306	This study
pKF107	*ins1038 spc98* in pRS306	This study
pKF108	*ins1384 spc98* in pRS306	This study
pKF109	*ins1415 spc98* in pRS306	This study
pKF110	*ins1421 spc98* in pRS306	This study
pKF111	*ins1713 spc98* in pRS306	This study
pKF112	*ins1974 spc98* in pRS306	This study
pKF113	*ins2180 spc98* in pRS306	This study
pKF114	*ins2181 spc98* in pRS306	This study
pKF115	*ins2182 spc98* in pRS306	This study
pKF116	*ins2187 spc98* in pRS306	This study
pKF117	*ins2278 spc98* in pRS306	This study
pKF118	*spc98(K417A/E418A/Q420A/N423A/E424A)* in pRS306	This study
pKF141	*ins510 spc97* in pRS316	This study
pKF142	*ins527 spc97* in pRS316	This study
pKF143	*ins583 spc97* in pRS316	This study
pKF144	*ins838 spc97* in pRS316	This study
pKF145	*ins871 spc97* in pRS316	This study
pKF146	*ins1034 spc97* in pRS316	This study

pKF147	*ins1038 spc97* in pRS316	This study
pKF148	*ins1076 spc97* in pRS316	This study
pKF149	*ins1284 spc97* in pRS316	This study
pKF174	*SPC97* in pRS306	This study
pKF177	*SPC97-GFP* in pRS316	This study
pKF178	*GFP-SPC98* in pRS316	This study
pKF179	*ins207 spc97-GFP* in pRS316	This study
pKF180	*ins349 spc97-GFP* in pRS316	This study
pKF181	*Ins854 spc97-GFP* in pRS316	This study
pKF182	*ins1755 spc97-GFP* in pRS316	This study
pKF183	*ins1901 spc97-GFP* in pRS316	This study
pKF184	*ins568 GFP-spc98* in pRS316	This study
pKF185	*ins886 GFP-spc98* in pRS316	This study
pKF186	*ins1025 GFP-spc98* in pRS316	This study
pKF187	*ins1222 GFP-spc98* in pRS316	This study
pKF188	*ins1432 GFP-spc98* in pRS316	This study
pKF189	*ins1827 GFP-spc98* in pRS316	This study
pKF190	*ins2470 GFP-spc98* in pRS316	This study
pKF204	*(S208A/S209A) spc97-GFP* in pRS316	This study
pKF205	*SPC97-GFP* in pRS306	This study
pKF206	*GFP-SPC98* in pRS306	This study
pKF207	*ins207 spc97-GFP* in pRS306	This study
pKF208	*ins349 spc97-GFP* in pRS306	This study
pKF209	*Ins854 spc97-GFP* in pRS306	This study
pKF210	*ins1755 spc97-GFP* in pRS306	This study
pKF211	*ins1901 spc97-GFP* in pRS306	This study
pKF212	*ins568 GFP-spc98* in pRS306	This study
pKF213	*ins886 GFP-spc98* in pRS306	This study
pKF214	*ins1025 GFP-spc98* in pRS306	This study
pKF215	*ins1222 GFP-spc98* in pRS306	This study
pKF216	*ins1432 GFP-spc98* in pRS306	This study
pKF217	*ins1827 GFP-spc98* in pRS306	This study
pKF218	*ins2470 GFP-spc98* in pRS306	This study
pKF219	*(S208A/S209A) spc97-GFP* in pRS306	This study
pKF220	*tub4(T239A) in pRS306*	This study
pKF221	*tub4(T239S) in pRS306*	This study
pKF222	*tub4(T239V) in pRS306*	This study
pKF227	*ins568 GFP-spc98* in pFastBac	This study
pKF228	*ins886 GFP-spc98* in pFastBac	This study
pKF229	*ins1025 GFP-spc98* in pFastBac	This study
pKF230	*ins1222 GFP-spc98* in pFastBac	This study
pKF231	*ins1432 GFP-spc98* in pFastBac	This study
pKF232	*ins1827 GFP-spc98* in pFastBac	This study
pKF233	*ins2470 GFP-spc98* in pFastBac	This study
pLA6	*TUB4 ADE3 LYS2* 2μm origin	Luther Arms

pTN25	*SPC97 ADE3* 2μm origin	Thu Nguyen
pYGFPgN	*GFP-kanMX*	Prein *et al.*, 2000

Table 3.3. Illumina sequencing of the transposition library.

	SPC97	***SPC98***
Total Illumina reads	15,703,128	17,066,525
Total reads containing *NotI*	96,542	99,991
Unique insertion events	2,194	2,105
Base pair coverage	88.8%	82.3%
Codon coverage	98.3%	97.3%

Table 3.4. Illumina sequencing of the lethal mutations.

	SPC97	***SPC98***
Total Illumina reads	7,210,851	17,818,279
Total reads containing *NotI*	82,191	152,334
Unique insertion events	607	578
Base pair coverage	24.6%	22.8%

Table 3.5. **Spc97 temperature sensitive insertions.**

Insertion Position	**15 base pair insertion**	**Inserted residues**
ins510	*TGCGGCCGCATCTAT*	CGRIY
ins527	*TGCGGCCGCAACAAA*	MRPQQ
ins583	*TGCGGCCGCAATGAA*	CGRNE
ins838	*TGCGGCCGCAACTAT*	CGRNY
ins871	*TGCGGCCGCAAGGGT*	CGRKG
ins1034	*TGCGGCCGCAACTAT*	LRPGL
ins1038	*TGCGGCCGCATTCAA*	NAAAF
ins1076	*TGCGGCCGCATCGAG*	VRPHR
ins1284	*TGCGGCCGCACTTGG*	GAAAL

Table 3.6. Spc98 temperature sensitive insertions.

Insertion Position	15 base pair insertion	Inserted residues
ins35	*TGCGGCCGCAAATAG*	VRPQI
ins557	*TGCGGCCGCACCTAA*	MRPHL
ins561	*TGCGGCCGCAAAATA*	YAAAK
ins573	*TGCGGCCGCATATAC*	TAAAY
ins769	*TGCGGCCGCATAGAA*	CGRIE
ins848	*TGCGGCCGCAATCGT*	LRPQS
ins1033	*TGCGGCCGCAATGAG*	CGRNE
ins1035	*TGCGGCCGCAGAGTA*	YAAAE
ins1038	*TGCGGCCGCAATCAT*	CGRNH
ins1384	*TGCGGCCGCACTAAT*	CGRTN
ins1415	*TGCGGCCGCACAGAG*	VRPHR
ins1421	*TGCGGCCGCACGTGG*	VRPHV
ins1713	*TGCGGCCGCATTAGT*	VAAAL
ins1974	*TGCGGCCGCAATAGA*	DAAAI
ins2180	*TGCGGCCGCAAGTGT*	VAAAS
ins2181	*TGCGGCCGCAGTGTA*	CGRSV
ins2182	*TGCGGCCGCATGTAC*	LRPHV
ins2187	*TGCGGCCGCACATAA*	NAAAH
ins2278	*TGCGGCCGCAACCCA*	CGRNP

Chapter 4

Optimized purification of budding yeast spindle pole bodies yields a high resolution cell cycle phosphoproteome

Introduction

The centrosome is the microtubule organizing center of the cell, responsible for nucleating microtubules and establishing a bioriented spindle during mitosis. In budding yeast, the spindle pole body is the functional equivalent of centrosomes in higher eukaryotes and most of the spindle pole body components in yeast have homologs in human centrosomes. While morphologically distinct from higher eukaryotic centrosomes, the yeast spindle pole body has been used to determine highly conserved mechanisms of centrosomal regulation. The genetic tractability and the simplicity of the yeast mitotic spindle make it an attractive model organism for the study of mitosis, microtubule nucleation, and the regulation of these processes.

The yeast spindle pole body has been extensively characterized *in vivo* through thin section electron microscopy (Moens and Rapport, 1971; Byers and Goetsch, 1975; Winey *et al.*, 1995), genetic and mutational screens (Winey *et al.*, 1991; Geissler *et al.*, 1996; Spang *et al.*, 1996a; Knop *et al.*, 1997), and fluorescence microscopy (Burns *et al.*, 2015). The difficulty of spindle pole body purifications has limited the *in vitro* analysis of this structure. Historical methods purified spindle pole bodies out of *S. uvarum* (Rout and Kilmartin, 1990; Bullitt *et al.*, 1997), an organism limited in genetic and mutational analyses compared *S. cerevisiae.* Improvement to purification protocols out of *S. cerevisiae* have enabled us to study spindle pole body mutants and fluorescently characterize spindle pole bodes *in vitro* (Niepel *et al.*, 2005; Fong *et al.*, 2016). Here, we use an optimized purification protocol, described in Chapter 2, to

purify spindle pole bodies for *in vitro* fluorescence analysis and high resolution mass spectrometric phosphoproteomic analysis of spindle pole body components.

Centrosomes have been shown to serve as a signaling platforms, integrating cell signals to regulate progression through the cell cycle and localization of spindle proteins (Rieder *et al.*, 2001; Lange, 2002; Cha *et al.*, 2004; Jaspersen and Winey, 2004; Casenghi *et al.*, 2005; Jiang *et al.*, 2006; Basto and Pines, 2007; Winey and Bloom, 2012; Burns *et al.*, 2015). One widely studied cell signal has been phosphorylation of spindle pole body proteins. Several kinases, including the Mps1, Aurora A, and Cdc28 kinase families, have been implicated in the regulation of cell cycle transitions (Winey *et al.*, 1991; Deshaies and Ferrell Jr., 2001; Castillo *et al.*, 2002; Dutertre *et al.*, 2004; Kinoshita *et al.*, 2005). More specifically, individual phosphorylation sites have been mutated in Tub4 (Vogel *et al.*, 2001; Keck *et al.*, 2011; Lin *et al.*, 2011), Spc42 (Donaldson and Kilmartin, 1996), Spc98 (Pereira *et al.*, 1998), and Spc110 (Friedman *et al.*, 1996, 2001; Stirling and Stark, 1996; Huisman *et al.*, 2007) and have been shown to have effects on cell cycle progression.

Previous attempts to determine the yeast centrosomal phosphoproteome were limited by the technology and software of the time (Keck *et al.*, 2011). Ambiguous phosphorylation assignments and low resolution instruments limited the precision of phosphorylation site assignments. A previous phosphoproteome study reported 298 phosphorylation sites in the 18 spindle pole body components throughout the cell cycle (Keck *et al.*, 2011). For site specific mutagenesis studies of individual phosphorylation sites, 298 sites is an unwieldy data set for the yeast centrosome community. In order to narrow down the most confident sites, we report here a higher resolution cell cycle phosphoproteome of the yeast centrosome. In recent years, great strides have been made in the resolution and sensitivity of mass spectrometers and new software

packages impose stringent quality cutoffs. These technological advances have resulted in more precise, higher resolution phosphorylation assignments resulting in our most confident and focused data set of phosphorylation sites.

Materials and methods

Strains, plasmids, and media

The yeast strains used in this study were all derived from W303 and are listed in Table 4.1. C-terminally TAP tagged proteins were created by PCR amplifying the *TAP-kanMX* cassette from the plasmid TAP-2xPA using primers that shared homology with the flanking sequences of the stop codon in the gene of interest. Cnm67 was N-terminally TAP tagged by PCR amplification of the *TAP-kanMX* cassette from the plasmid PaTEVCa, using primers that shared homology with the flanking DNA of the start codon of *CNM67*. C-terminal mCherry and GFP protein fusions were created by PCR amplification of the *mCherry-hphMX3* and the *GFP-kanMX* cassettes from pBS35 and pFA6-GFP(S65T)::kanMX plasmids, respectively (gifts from the Yeast Resource Center, University of Washington, Seattle, WA). The cassettes for the fluorescent proteins shared homology with the flanking sequence around the stop codon of the genes of interest. For the Cdc20-AID strain, the auxin degron IAA7 was PCR amplified from pSB2065 (gift from Sue Biggins, Fred Hutchinson Cancer Research Center, Seattle, WA) with primers that shared homology with the flanking DNA of the stop codon of *CDC20*. The above cassettes were integrated into a diploid strain, KGY315, and verified by PCR.

The plasmids used in this study are listed in Table 4.2. QuikChange Lightning Multi Site-Directed Mutagenesis (Stratagene) was used to construct plasmids containing point mutations. Spc97 mutant plasmids were transformed into KFY38-5C, Spc98 mutant plasmids were transformed into KFY37-4C, and Tub4 mutant plasmids were transformed into KFY220-1A to screen for viability via a plasmid shuffle screen. These three strains all contained GFP-Tub1 for imaging of microtubules and Spc42-mCherry to visualize spindle pole bodies.

YPD media is as described (Burke *et al.*, 2000). SD-ura low ade and SD-lys were previously described (Sundberg *et al.*, 1996; Tien *et al.*, 2013).

TAP purification and velocity sedimentation

Spindle pole bodies were purified using a TAP-tag on Spc97, as previously described (Chapter 2). Sucrose gradients were generated by allowing five steps of sucrose solutions (200 µl each of 10%, 20%, 30%, 40%, 2.5 M sucrose) to equilibrate at 4°C for 2 hours. For fluorescence analysis, the sucrose solutions were made in 10 mM Bis-Tris, pH 6.5, 0.1 mM $MgCl_2$. For mass spectrometry analysis, the sucrose solutions were made in 40 mM HEPES, pH 7.4, 150 mM NaCl. The TEV eluate was then applied to the sucrose gradient and spun at 50000 rpm for 5 hours at 4°C in a TLS55 rotor (Beckman Coulter). Fractions (90 µl) were removed from the top of the gradient with wide-bore tips. The presence of SPBs was determined by western blot analysis, probing for Spc110 and Spc97. Western blot analysis showed the separation of intact spindle pole bodies (fractions 9-11) from the soluble pool of spindle pole body components (fractions 1-8).

For Cdc20-AID spindle pole bodies, cells were grown to 80 Klett units in YPD. Auxin (indole-3-acetic acid; IAA) in DMSO was added to a final concentration of 1 mM. Cdc20 was depleted for 1.5 generations before cells were harvested. In Cdc20 depleted cells, ≥98% of cells arrested with large buds. *Cdc4-1* spindle pole bodies were grown at 25°C to 60 Klett units, then shifted to the restrictive temperature of 36°C for two generations before harvesting cells. *Cdc4-1* cells arrested with 95% elongated buds and 5% large budded cells. Spindle pole bodies were then purified as previously described (Chapter 2).

Fluorescence microscopy

All images were acquired using a DeltaVision system (Applied Precision) with an IX70 inverted microscope (Olympus), an U Plan Apo 100x objective (1.35 NA) and a CoolSnap HQ digital camera (Photometrics). Exposures were 0.4 s for mCherry and GFP. Images were processed as previously described (Shimogawa *et al.*, 2009) using custom Matlab programs to identify GFP and mCherry foci and quantify the fluorescence intensities. For live-cell imaging, cells were mounted on an agarose pad a previously described (Muller *et al.*, 2005). Metaphase spindles were identified as spindles with 20-25 pixels between spindle poles.

For *in vitro* spindle pole body imaging, a flow cell was constructed with KOH cleaned glass coverslips. Spindle pole bodies were diluted with 5X BRB80/BSA (400 mM K-PIPES, pH 6.9, 5 mM $MgCl_2$, 5 mM EGTA, 40 mg/ml BSA) and KCl to a final concentration of BRB80, 8 mg/ml BSA and 500 mM KCl. The diluted spindle pole bodies were flowed into the flow cell and allowed to nonspecifically adhere to the coverslip for 30 minutes before imaging.

For immunofluorescence analysis, spindle pole bodies were diluted with 5X BRB80/BSA (400 mM K-PIPES, pH 6.9, 5 mM $MgCl_2$, 5 mM EGTA, 40 mg/ml BSA) and KCl to a final concentration of BRB80, 8 mg/ml BSA and 500 mM KCl. The diluted spindle pole bodies were flowed into the flow cell, and incubated for 30 minutes. The spindle pole bodies were washed with BRB80 and 8 mg/ml BSA then fixed with 2% glutaraldehyde. The spindle pole bodies were probed for α-tubulin with 1:100 DM1α-FITC (Sigma Aldrich) for 20 minutes at 37^{o}C. The SPBs were washed with BRB80 and 8 mg/ml BSA, then imaged. Exposures were 0.25 seconds for both mCherry and GFP, and images were analyzed by custom Matlab software.

Mass spectrometry sample preparation and digestion

Purified spindle pole body fractions in 40-50% sucrose, 40 mM HEPES, pH 7.4, and 150 mM NaCl, were combined such that samples were approximately 2 to 30 µg total protein in 0.5 to 1.5 mL of buffer plus approximately 45% sucrose. Samples were diluted 1:1 using 25 mM ammonium bicarbonate (ABC) and concentrated down to 30 µL using Amicon® Ultra 0.5 mL Centrifugal Filters with a 10,000 NMWL (Merc Millipore Ltd.) according to the manufacturer's instructions. 500 µL of 25 mM ammonium bicarbonate was added to the top of the filter unit and spun through. This was repeated a total of three times. Sample volume was made up to 100 µL of 25 mM ABC and reduced in the filter unit with 10 mM dithiothreitol (DTT) at 37ºC for 30 minutes followed by a 30-minute alkylation at room temperature with 15 mM iodoacetamide. 1 µL of 0.8 µg/µL Sequencing Grade Modified Trypsin (Promega Corporation) was used to digest the samples in the filter units at 37ºC for 4 hours at 1,200 rpm in an Eppendorf Thermomixer. After digestion spun through the filter units into a new Amicon Eppendorf tube. 100 µL of 25 mM ABC was added to the top of the filter unit and spun through into the same tube. The remaining digested sample was transferred from the filter unit into the Eppendorf tube by pipette. The digested sample was reduced to about 50 µL in a speedvac. Sample pH was adjusted to 2 with 5M HCl prior to storage at -80°C until MS analysis.

Mass spectrometry

Mass spectrometry was performed on either a Q-Exactive or Q-Exactive HF (Thermo Fisher Scientific). 3 µL of sample digest was loaded by autosampler onto a 150-µm Kasil fritted trap packed with Jupiter C12 90 Å material (Phenomenex) to a bed length of 2 cm at a flow rate of 2 µL/min. After loading and desalting using a total volume of 8 µL of 0.1% formic acid plus

2% acetonitrile, the trap was brought on-line with either a pulled fused-silica capillary tip (75-µm i.d.) or an empty Pico-Frit column (New Objective) that was self-packed with 30 cm of Reprosil-Pur C18-AQ (3-µm bead diameter, Dr. Maisch) mounted in an in-house constructed microspray source and placed in line with a Waters Nanoacquity binary UPLC pump plus autosampler. Peptides were eluted off the column using a gradient of 2-35% acetonitrile in 0.1% formic acid over 120 minutes, followed by 35-60% acetonitrile over 10 minutes at a flow rate of 250 nL/min.

The Q-Exactive mass spectrometer was operated using data dependent acquisition (DDA) where a maximum of twenty MS/MS spectra were acquired per MS spectrum (scan range of m/z 400 to 1600). The resolution for MS and MS/MS was 60,000 and 15,000, respectively, at m/z 200. The automatic gain control (AGC) targets for MS and MS/MS were set to 3e6 and 1e5, respectively, and the maximum fill times were 50 and 25 msec, respectively. The MS/MS spectra were acquired using an isolation width of 1.6 m/z and a normalized collision energy (NCE) of 27. The underfill ratio was set to 10% and the intensity threshold set to 4e5. MS/MS acquisitions were prevented for unassigned, +1, +6 and greater precursor charge states. Dynamic exclusion (including all isotope peaks) was set for 5 or 10 seconds. The Q-Exactive HF was operated similarly.

Analysis of mass spectrometry data

Mass spectra were converted into mzML using msconvert from ProteoWizard (Chambers *et al.*, 2012). All proteins detectable were identified by searching high-resolution MS/MS spectra against whole proteome databases using Comet (Eng *et al.*, 2013). A variable modification of 79.966331 on S, T or Y was included in the search to identify phospho-peptides. Peptide identifications were processed with Percolator (Käll *et al.*, 2007) and MSDaPl was used to

visually inspect the results (Sharma *et al.*, 2012) and confirm the assignment of phosphorylated residues.

Results

C-terminally TAP-tagged Spc97 increases the yield of spindle pole bodies

Previous studies have shown that spindle pole bodies from *S. cerevisiae* co-purify with a TAP-tag on a nuclear pore component, Mpl2 (Niepel *et al.*, 2005). In an effort to increase the yield of purified spindle pole bodies, TAP tags were introduced on several spindle pole body components to determine viability and yield of purified spindle pole bodies, using the protocol described in Chapter 2 (Table 4.3). Spc42-TAP was not viable in our strain background. Strains were constructed with Bbp1-TAP, TAP-Cnm67, Mlp2-TAP, Nbp1-TAP, Spc72-TAP, Spc97-TAP, and Spc110-TAP and spindle pole body purification yield was determined by western blot analysis. Several protein constructs (Bbp1-TAP, Mlp2-TAP, Nbp1-TAP, and Spc72-TAP) bound weakly to IgG beads, resulting in a low yield of spindle pole bodies. Others, (TAP-Cnm67 and Spc110-TAP) showed relatively strong binding to IgG beads, but TEV cleavage failed to remove the purified spindle pole bodies from the beads, again resulting in low yields. A C-terminal TAP tag on Spc97 was shown to not only bind the strongest to IgG beads, but to also have efficient TEV cleavage from the beads, resulting in the highest, most reproducible yield of purified spindle pole bodies.

The addition of glycerol in purification buffers stabilizes intact purified spindle pole bodies

Initial results from the spindle pole body purification protocol suffered from dissociation of spindle pole body components, resulting in a large fraction of components present in the soluble fractions of the sucrose gradient (fractions 1-8). It was found that the addition of 5% glycerol to all purification buffers greatly increased the yield of intact spindle pole bodies, with

approximately 90% of α-Spc110 western blot signal reproducibly falling in the intact spindle pole body fractions (fractions 9-11) (Figure 4.1).

One advantage in the development of this purification method was improving the visualization of spindle pole bodies. Previous purification techniques could only visualize spindle pole bodies by electron microscopy (Byers *et al.*, 1978; Hyams and Borisy, 1978; Rout and Kilmartin, 1990; Bullitt *et al.*, 1997). The addition of fluorescent markers in our purification protocol allowed for fluorescent visualization and quantification of spindle pole bodies. Fluorescence analysis of spindle pole bodies also verified that glycerol in purification buffers maintained the size of purified spindle pole bodies and resulted in the retention of the γ-tubulin small complex when compared to spindle pole bodies in live cells (Figure 4.2). Spindle pole bodies containing Spc42-GFP or Tub4-GFP were purified with and without glycerol in the purification buffers. The spindle pole bodies were fluorescently imaged and compared to the fluorescence of live cells of the strain from which the spindle pole bodies were purified. Spc42-GFP spindle pole bodies purified in the presence of glycerol had the same fluorescence intensity as spindle pole bodies in live cells (Figure 4.2.a; BGY68-16A). The Tub4-GFP fluorescence showed that glycerol increased the retention of the γ-tubulin small complex at the spindle pole body (Figure 4.2.b; BGY74-17B) Spindle pole bodies purified in the presence of glycerol retained 88% of the γ-tubulin small complex compared to live cells, while the spindle pole bodies purified without glycerol only retained 40% of the γ-tubulin small complex.

Immunofluorescence shows spindle pole bodies are purified with native yeast tubulin

In electron micrographs of prior spindle pole body purifications, microtubules are evident on the purified spindle pole bodies. Immunofluorescence assays were used to determine if the

spindle pole bodies purified by this method also contained native yeast tubulin. The spindle pole bodies, containing Spc42 tagged with mCherry were probed for α-tubulin with DM1α-FITC (Sigma Aldrich), then imaged. Fluorescence analysis showed that 95%-100% of spindle pole bodies have yeast α-tubulin associated after purification (Figure 4.3.a.). The presence of yeast α- and β-tubulin was further verified by mass spectrometry.

It has been previously reported that soluble polymers such as polycationic DEAE-dextran or polyanionic heparin are effective in solubilizing chromatin and fractionating the nucleus (Bornens, 1973). Further, treating spindle pole bodies with DEAE-dextran was shown to remove microtubules, but maintain the gross morphology of the spindle pole body (Rout and Kilmartin, 1990). Purified spindle pole bodies were incubated with DEAE-dextran (40 mg/ml) for 1 hour before probing for α-tubulin by immunofluorescence. While DEAE-dextran had no effect on the core of the spindle pole body (Figure 4.3.b), immunofluorescence showed an 85% reduction in native α-tubulin associated with spindle pole bodies after treatment with DEAE-dextran (Figure 4.3.c). Similar treatment of spindle pole bodies with nocodazole and epothilone B did not show a reduction in tubulin immunofluorescence.

High resolution mass spectrometry data identified phosphorylation sites of the spindle pole body at different cell cycle stages

Phosphorylation data was collected for the purified spindle pole bodies. All eighteen proteins of the spindle pole body were present with high protein coverage in most of the mass spectrometry runs (Table 4.4). Comet was used to search sequence databases to assign peptides and proteins to mass spectra (Eng *et al.*, 2013, 2015). As a subsequent step, Percolator analyzed the matches made in Comet and provides statistics such as the q-value for each peptide spectrum

match (Käll *et al.*, 2007, 2008a, 2008b). The assigned q-value for a given peptide spectrum match in the data set represents the minimum false discovery rate. A q-value of ≤0.01 was used for all MS/MS spectra and peptide spectrum matches, which means 1% is the minimal false discovery rate threshold at which the MS/MS spectrum or peptide spectrum match would be included in the data set. Of the spectra collected, 5.9-47.6% had a q-value of ≤0.01. Of the peptide spectrum matches, 39.0-65.9% of the spectrum matches had a q-value of ≤0.01.

All identified phosphorylation sites were further verified manually to identify any ambiguous or unsubstantiated assignments. In this new data set, 179 phosphorylation sites were reported across asynchronous cells, mitotic cells, and G1 cells (Figure 4.4.c and Table 4.5).

Spindle pole bodies purified from cdc4-1 temperature sensitive cells provides a novel data set in the yeast cell cycle phosphoproteome

The Keck *et al*, 2011 data used alpha factor arrest to arrest the cells in G1 before harvesting spindle pole bodies. The new data set of G1 spindle pole bodies was arrested in G1/S with a *cdc4-1* temperature sensitive arrest. These two G1 arrests differ greatly in the cellular environment. In an alpha factor arrest, the spindle pole bodies are not duplicated and Clb-Cdc28 is inhibited (Peter and Herskowitz, 1994; Gartner *et al.*, 1998; Jeoung *et al.*, 1998). In contrast, in a *cdc4-1* arrest, the spindle pole bodies are duplicated but not separated (Byers and Goetsch, 1974; Pereira *et al.*, 1998) and there are high levels of Cln-Cdc28 and low levels of Clb-Cdc28 (Duncker *et al.*, 1999; Blondel *et al.*, 2000). The *cdc4-1* shift to the restrictive temperature arrests spindle pole bodies at the point in the cell cycle where nucleation first occurs, suggesting that the phosphorylation profile at this arrest is conducive to high nucleation activity.

Cdc4-1 spindle pole bodies were harvested after a shift to the restrictive temperature and analyzed by mass spectrometry, resulting in a novel data set describing the centrosome phosphoproteome in G1/S (Table 4.5; KFY332-12C).

Reanalysis of previously published phosphoproteomic data reduces the data set based on statistical quality cutoffs

The new phosphoproteome data set reported 179 phosphorylation sites while the previously published data set reported 298 phosphorylation sites. To determine if the difference between the data sets was due to analysis of the mass spectra, we reanalyzed the raw data from Keck *et al.*, 2011 using Comet and Percolator, the same algorithms used for the new data set.

The reanalysis of the Keck *et al*, 2011 raw data set resulted in a reduction from 298 published phosphorylation sites to 171 phosphorylation sites (Figure 4.4.a, b and Table 4.6). Many of the ambiguous assignments were removed from the data set by imposing statistical cutoffs for spectra included in the data set. Using Percolator, only spectra and peptide spectrum matches (PSMs) with a q-value of ≤0.01 were included in the reanalysis data set. (Figure 4.5). For the published data sets, 0.1-6.4% of the total MS/MS spectra had a q-value of ≤0.01, and 0.1-8.2% of the peptide spectrum matches had a q-value of ≤0.01. Under these strict statistical cutoffs, many of the unique G1 phosphorylation sites were eliminated from the data set.

Comparison of phosphoproteome data sets identified a subset of high confidence phosphorylation assignments

Comparison of the original published Keck *et al*, 2011 data, the reanalyzed Keck *et al*, 2011 data, and the newly collected high resolution data set showed agreement for approximately 20% of the identified phosphorylation sites in asynchronous cells and mitotic cells. (Figure 4.6,

Table 4.7). Comparison of the *cdc4-1* G1/S phosphoproteomic profile to the alpha factor phosphoproteomic profile showed low agreement of 10% (Figure 4.6.d), suggesting that these two data set describe distinct states in the spindle pole body cell cycle.

A specific example comparing these three data sets can be seen when examining the asynchronous N-terminal phosphorylation sites of Spc110 (Figure 4.6.e). The shaded light yellow and green show the peptide coverage of the protein. With changes to the data collection protocol, the newest data set had higher coverage of the entire protein. The N-terminus of Spc110 contains a prime example of the ambiguity of phosphorylation assignments. In Spc110, S30, S36, and S38 always fall on the same tryptic peptide. With low resolution data, it is possible to determine that a phosphorylation event is present on the peptide, but precise localization of the event can be difficult. Keck *et al*, 2011 reported all three sites, due to this ambiguity. Reanalysis of the Keck *et al*, 2011 data set showed that there was no high quality data supporting a phosphorylation site on S30. The new high resolution data set also found no evidence of S30 phosphorylation.

Phosphoblocking mutations of both Spc97 mitotic sites S208 and S209 is lethal and Tub4 phosphomimicking mutations alter tubulin distribution in metaphase spindles

In the previous phosphoproteomic data, Spc97 was found to have two sites unique to mitosis, S208 and S209 (Keck *et al.*, 2011). Spc98 had four sites (S109, S136, S524, and S531), and Tub4 had five sites (S42, S360, Y362, S444, and Y445) (Keck *et al.*, 2011). Phosphomimetic mutations and phosphoblocking mutations were made for all mitotic phosphorylation sites in these three proteins (List of strains in Table 4.1). The mutations were integrated into yeast strains. For Spc98, yeast strains were viable when all four sites were

mutated to phosphomimetics (S109D/S136D/S524D/S531D) as well as when they were mutated to phosphoblocks (S109A/S136A/S524A/S531A). Tub4 strains were also viable when all five sites were mutated to block phosphorylation (S42A/S360A/Y362F/S444A/Y445F) and Spc97 strains were viable when mimicking phosphorylation (S208D/S209D). However, the phosphomimicking mutations in Tub4 (S42D/S360D/Y362E/S444D/Y445E) and the phosphoblocking mutations in Spc97 (S208A/S209A) were lethal (Figure 4.7).

The Tub4 phosphomimetics and the Spc97 phosphoblocks were made individually and integrated into yeast strains. It was found that Spc97 S208A or Spc97 S209A are viable individually, with normal growth rates, morphologically wild type spindles and wild type tubulin distributions across metaphase spindles (Figure 4.8.a). The location of the Spc97 mitotic phosphorylation sites suggests that this region may be involved in interactions with Spc110. Disruption of the interface between Spc97 and Spc110 may impede n may be involved in interactions with Spc110. Disruption of the interface between Spc97 and Spc110 may impede γ-tubulin ring complex formation or establishment of a proper microtubule template.

In contrast, some of the Tub4 mitotic phosphomimicking mutations had phenotypes when mutated alone or in smaller subsets. The lethality of all mitotic Tub4 mutations is attributed to S360D, which was previously shown to be lethal (Vogel *et al.*, 2001). Tub4 mutants S42D, Y445E, and the combination of S444D and Y445E had slower growth rates when compared to wild type. Furthermore, these three mutant strains showed differences in tubulin distribution across the metaphase spindle (Figure 4.8.b). The mutation in Y445 also resulted in abnormal spindle morphologies, including multipolar spindles and defects in microtubule bundling, when alone or in combination with S444D. S444 and Y445 fall on the outside of Tub4, in a region that may interact with Spc110. As with the phosphorylation mutants of Spc97, these two

phosphorylation mutations in Tub4 may affect γ-tubulin small complex interaction with Spc110, which could ultimately disrupt γ-tubulin ring complex formation.

Discussion

Optimization of spindle pole body purification has enabled in vitro analysis of fluorescently labeled spindle pole bodies and genetic mutant spindle pole bodies

To investigate the function and regulation of spindle pole bodies *in vitro*, we developed a highly reproducible purification protocol to purify fluorescently labeled spindle pole bodies from *Saccharomyces cerevisiae.* The fluorescence intensities of spindle pole bodies *in vitro* are comparable to the intensities observed *in vivo,* suggesting the purified spindle pole bodies are intact and stable. The genetic flexibility of this technique has allowed us to arrest cells and study spindle pole bodies at particular stages of the cell cycle. Cells were arrested in mitosis through Cdc20 depletion and arrested in G1/S with the temperature sensitive *cdc4-1* allele. Spindle pole bodies were harvested under these arrests to study the centrosome phosphoproteome throughout the cell cycle.

Comparison of phosphoproteomic data sets identified a subset of high confidence phosphorylation sites

Phosphorylation data for the yeast centrosome was previously published (Keck *et al.*, 2011). Changes in the data collection protocol made this new data set orthogonal to the published data set. The previous phosphorylation data sets were collected from samples enriched for phosphopeptides on a titanium dioxide column, which enriches for rare phosphorylation sites, but does not ensure complete coverage of all proteins (Keck *et al.*, 2011). As an alternative approach, the recent data set was collected on the entire purified spindle pole body.

One of the major limitations of low resolution data sets is that there are many ambiguous assignments. For completeness, Keck *et al*, 2011 reported all possible phosphorylation sites.

Sites that always fall in the same tryptic peptide fragment could not be differentiated in this data set, so all possible sites were reported. In this study, we have collected new high resolution cell cycle data for purified spindle pole bodies. The high resolution data set identified more peaks in the MS/MS spectra, which enabled us to make confident assignments and differentiate among phosphorylation sites on the same tryptic peptide. We have also reanalyzed the published raw data with new search algorithms and stringent statistical cutoffs to reduce ambiguity and improve confidence in phosphorylation assignments. Reanalysis of the data and new quality cutoffs reduced the published data set of 298 phosphorylation sites to 171 phosphorylation sites. Comparison of the published Keck *et al*, 2011 data, the reanalysis of the Keck *et al*, 2011 data, and the new data showed agreement among all three data set for 51 asynchronous phosphorylation sites and 43 mitotic phosphorylation sites. There are also 28 phosphorylation sites that were identified in alpha factor arrest by both the published and reanalyzed data of Keck *et al*, 2011 (Table 4.7).

New cdc4-1 phosphorylation data describes a novel phosphorylation state of the spindle pole body requiring further investigation

In addition to condensing the published phosphoproteome to the most confident phosphorylation assignments, this research has added a novel data set to the phosphoproteome. Rather than using alpha factor to arrest cells in G1, we have chosen to use a *cdc4-1* arrest for G1/S spindle pole bodies. In the *cdc4-1* arrest, spindle pole bodies are duplicated but not separated, capturing spindle pole bodies at the stage of the cell cycle when nucleation first occurs. The comparison of the phosphorylation sites identified by the alpha factor arrest and the

cdc4-1 arrest resulted in very low overlap (10%) between the two conditions, suggesting that these are distinct phosphorylation states of the spindle pole body.

The collection of the *cdc4-1* phosphorylation data set could provide insights into the state of the spindle pole body when it initiates nucleation. The unique phosphorylation sites from this study could provide previously unpublished sites that may be essential for the regulation of microtubule nucleation. Further work needs to be completed to study individual *cdc4-1* phosphorylation sites *in vivo*, similar to the study of mitotic sites in Spc97, Spc98, and Tub4 presented in this chapter.

In the alpha factor arrest, there was very little phosphorylation identified on the γ-tubulin small complex (Spc97, Spc98 and Tub4) or the linker proteins that bind the γ-tubulin small complex to the core of the spindle pole body (Spc72 and Spc110). The γ-tubulin small complex is essential for nucleation, so phosphorylation sites on these three proteins are of great interest in understanding how microtubule nucleation is regulated. In contrast, the *cdc4-1* arrested spindle pole bodies exhibited many phosphorylation sites on the γ-tubulin small complex as well as the linker proteins. The phosphorylation sites on Spc97, Spc98, and Tub4 that are unique to *cdc4-1* arrest would be the top priority for further *in vivo* study. Phosphoblocking mutations may result in nucleation deficiencies that could manifest as broken spindles, monopolar spindles, or even lethality. Phosphomimicking mutations could have nucleation activating effects at other times during the cell cycle.

Acknowledgements

Development of the spindle pole body purification protocol and fluorescence analysis was done in close collaboration with Beth Graczyk. The mass spectrometry sample preparation, data collection and data analysis were completed by Alex Zelter and Michael Riffle. Fluorescence analyses of Spc97 and Tub4 phosphorylation mutants were done with the aid of Jill Hoyt.

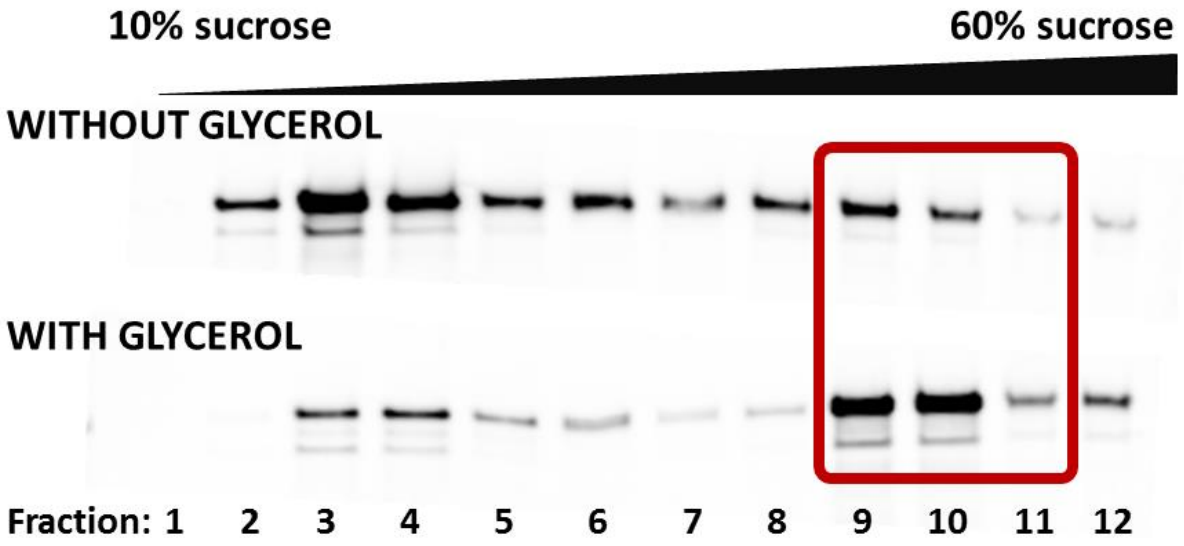

Figure 4.1. Western blot analysis of velocity sedimentation of spindle pole bodies purified in the presence or absence of 5% glycerol.
Sucrose gradient fractions, increasing from left (10%) to right (60%) were probed for Spc110. In the presence of glycerol, the percentage of Spc110 signal present in fractions 9-11 is reproducibly over 90%.

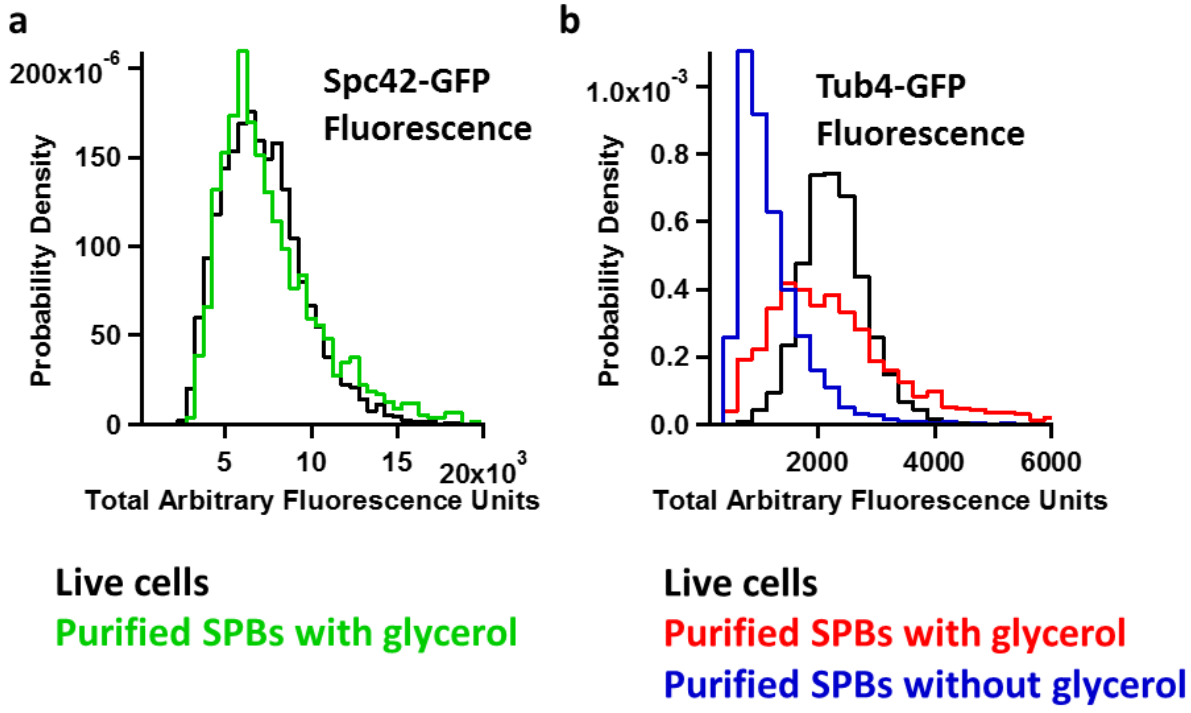

Figure 4.2. Fluorescence profile of purified spindle pole bodies and live cells.
a. Histogram of Spc42-GFP fluorescence for live cells (in black) and spindle pole bodies purified in the presence of glycerol (in green) b. Histogram of Tub4-GFP fluorescence for live cells (in black), spindle pole bodies purified in the presence of glycerol (in red), and spindle pole bodies purified without glycerol (in blue).

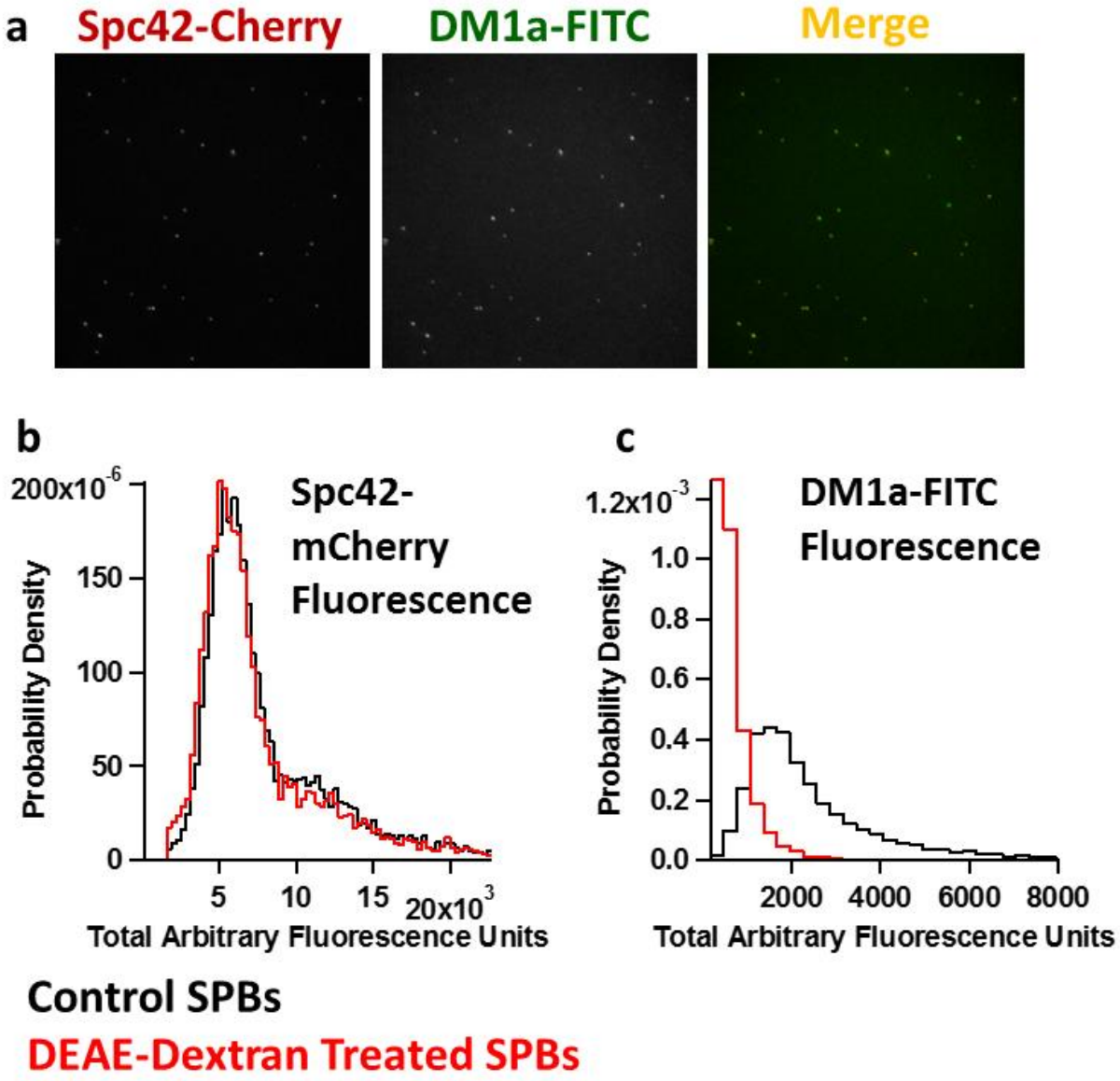

Figure 4.3. DEAE-Dextran treatment of SPBs removes tubulin.
a. Immunofluorescence analysis shows purified spindle pole bodies contain tubulin. Spindle pole bodies were purified and immunofluorescence analysis using an antibody against α-tubulin (DM1a-FITC) showed >95% of spindle pole bodies contained yeast α-tubulin. b. Histogram of Spc42-mCherry fluorescence and c. DM1a-FITC fluorescence for control SPBs (in black) and DEAE-dextran treated SPBs (in red).

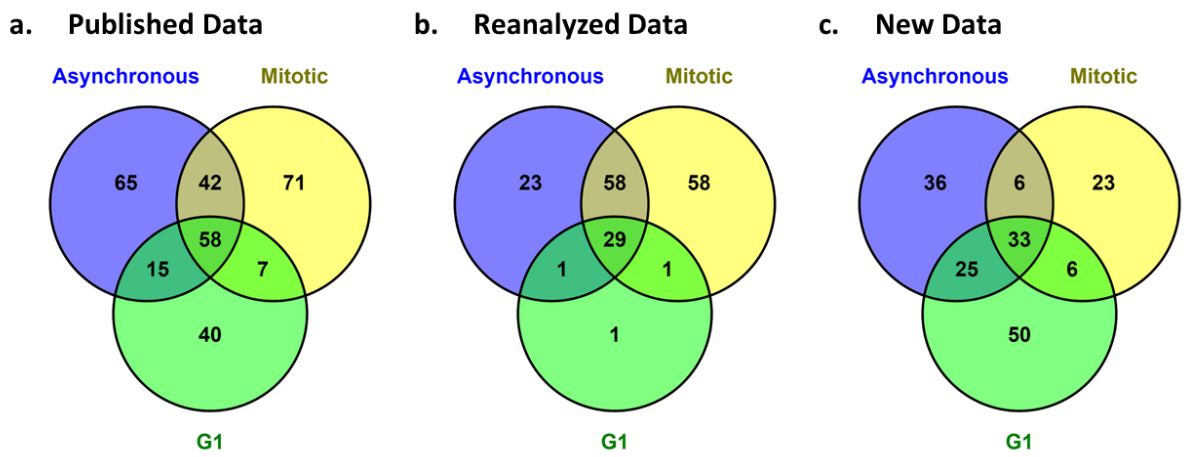

Figure 4.4. Three cell cycle phosphoproteome data sets.
Reanalysis of Keck *et al*, 2011 phosphoproteomic data reduces the number of sites to the most confident assignments. a. Venn diagram of the published phosphorylation sites observed under various cell cycle conditions (298 published sites). b. Reanalysis with Comet and Percolator have reduced the phosphorylation data set to the most confident assignments (171 sites). c. New data set reported in this chapter (179 sites). Figures created with Venny, 2.1.0, Oliveros, 2007.

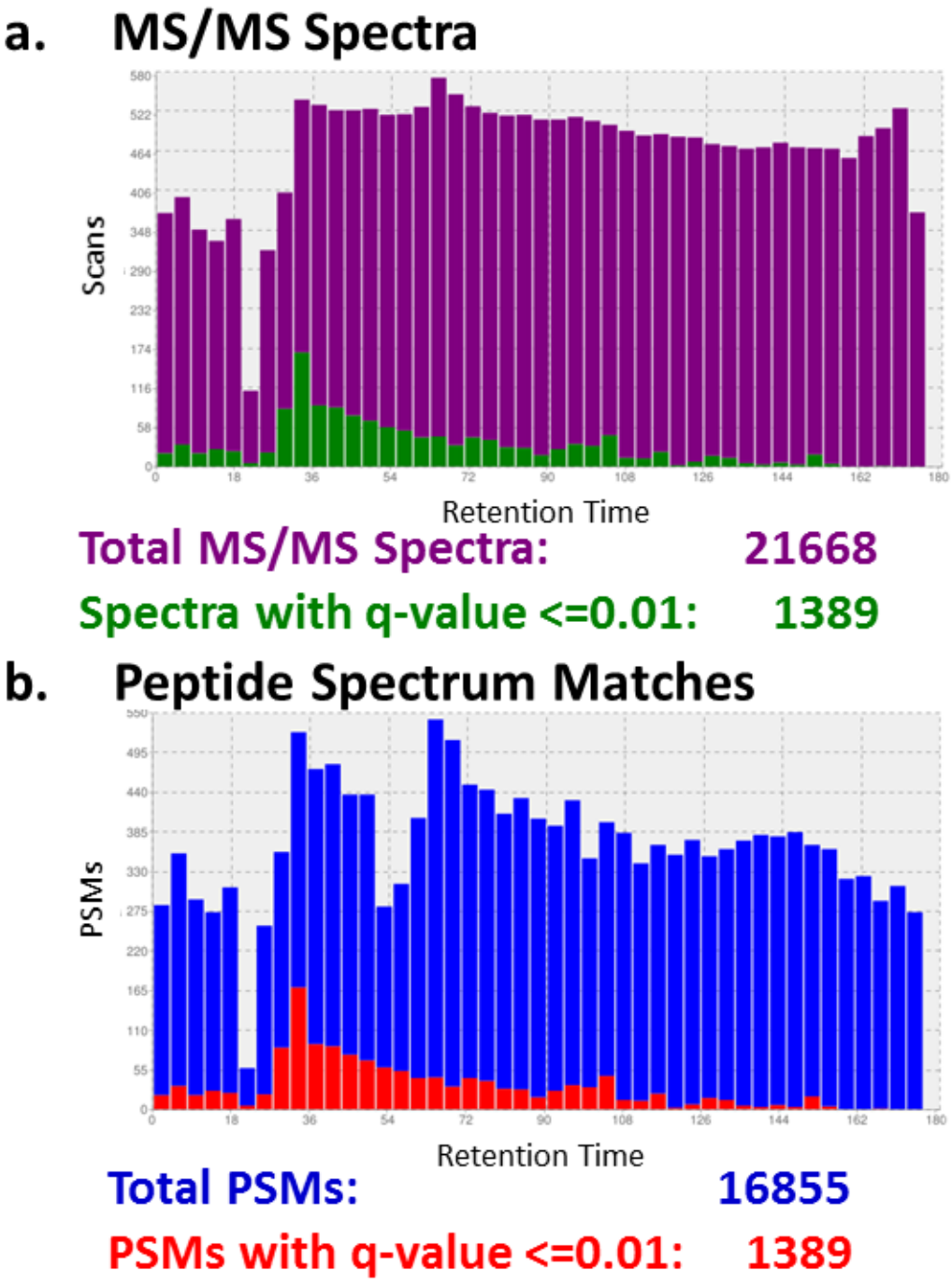

Figure 4.5 Representative Percolator quality plots from reanalysis of published data. For a given mass spectrometry run, Percolator outputs two quality plots. a. Total number of MS/MS spectra collected for a given run as a function of retention time shown in purple and the spectra with a q-value of ≤0.01 shown in green. b. Total number of peptide spectrum matches collected for a given run as a function of retention time shown in blue and the peptide spectrum matches with a q-value of ≤0.01 shown in red.

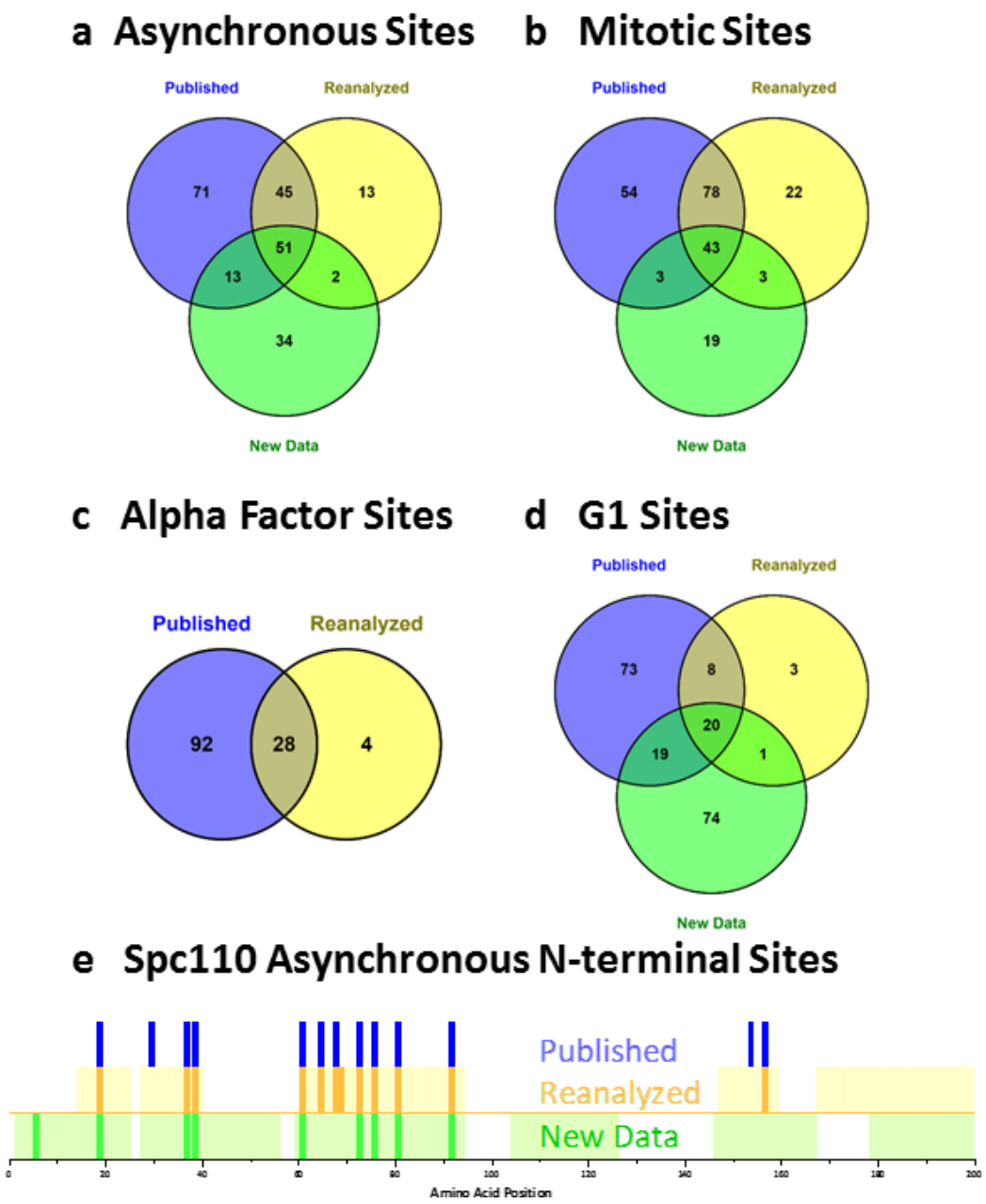

Figure 4.6. Comparison of all phosphoproteomic data sets.
Comparison among the published Keck *et al*, 2011 data set, the reanalysis of the Keck *et al*, 2011 data set, and the novel data set for a. asynchronous spindle pole bodies, b. mitotic spindle pole bodies, and c. the two data sets that examined alpha factor arrested spindle pole bodies. d. Comparison of the two type of G1 arrest, where the published and reanalyzed data used alpha factor and the Davis lab data used a *cdc4-1* temperature arrest. e. Comparison of asynchronous N-terminal sites of Spc110 (1-200aa). Peptide coverage of the reanalyzed data set and the Davis lab data set are shown in the light yellow and green shadings. Identified phosphorylation sites are indicated by the dark blue, yellow, and green bars. Figures created with Venny, 2.1.0, from Oliveros, 2007.

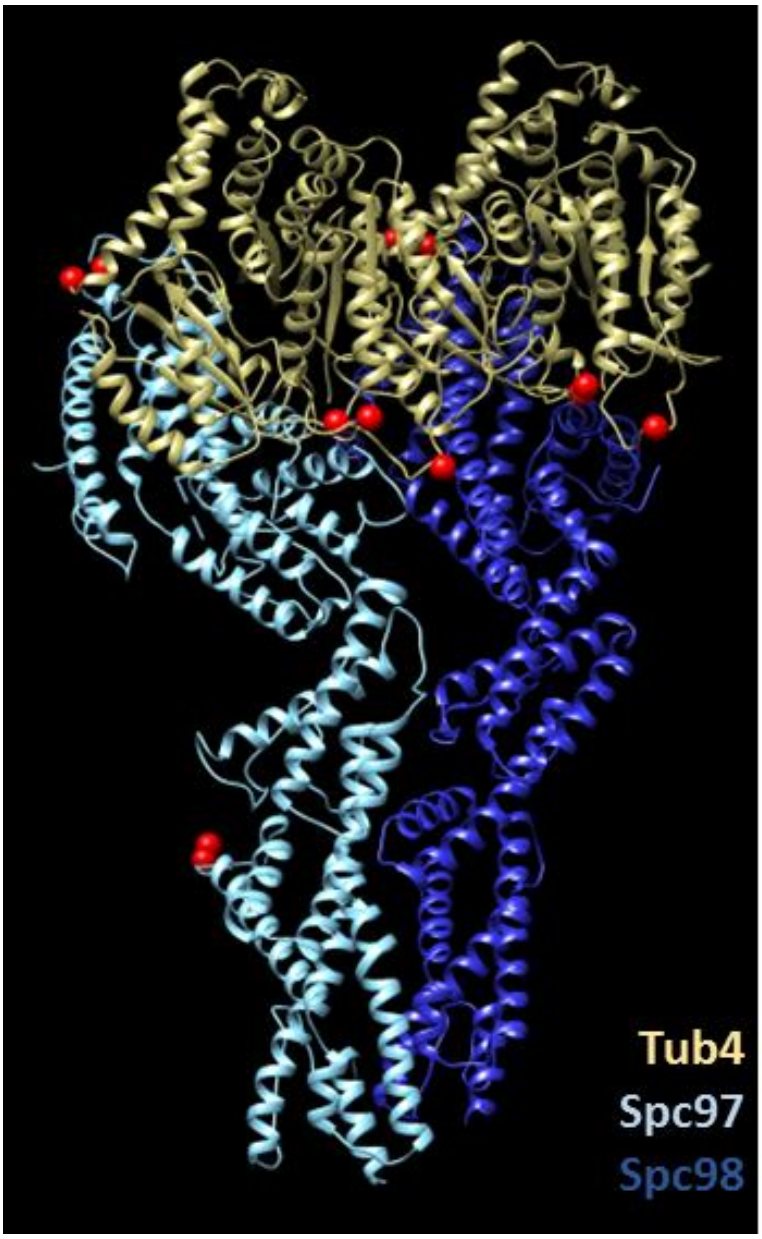

Figure 4.7. Mitotic phosphorylation mutants of the γ-tubulin small complex.
Mitotic phosphorylation sites (in red) have been mapped onto the pseudo-atomic structures of Spc97 and Tub4 as approximated by the crystal structure of GCP4 and human γ-tubulin. γ-tubulin structure adapted from Aldaz *et al.*, 2005; GCP4 structure adapted from Guillet *et al.*, 2011.

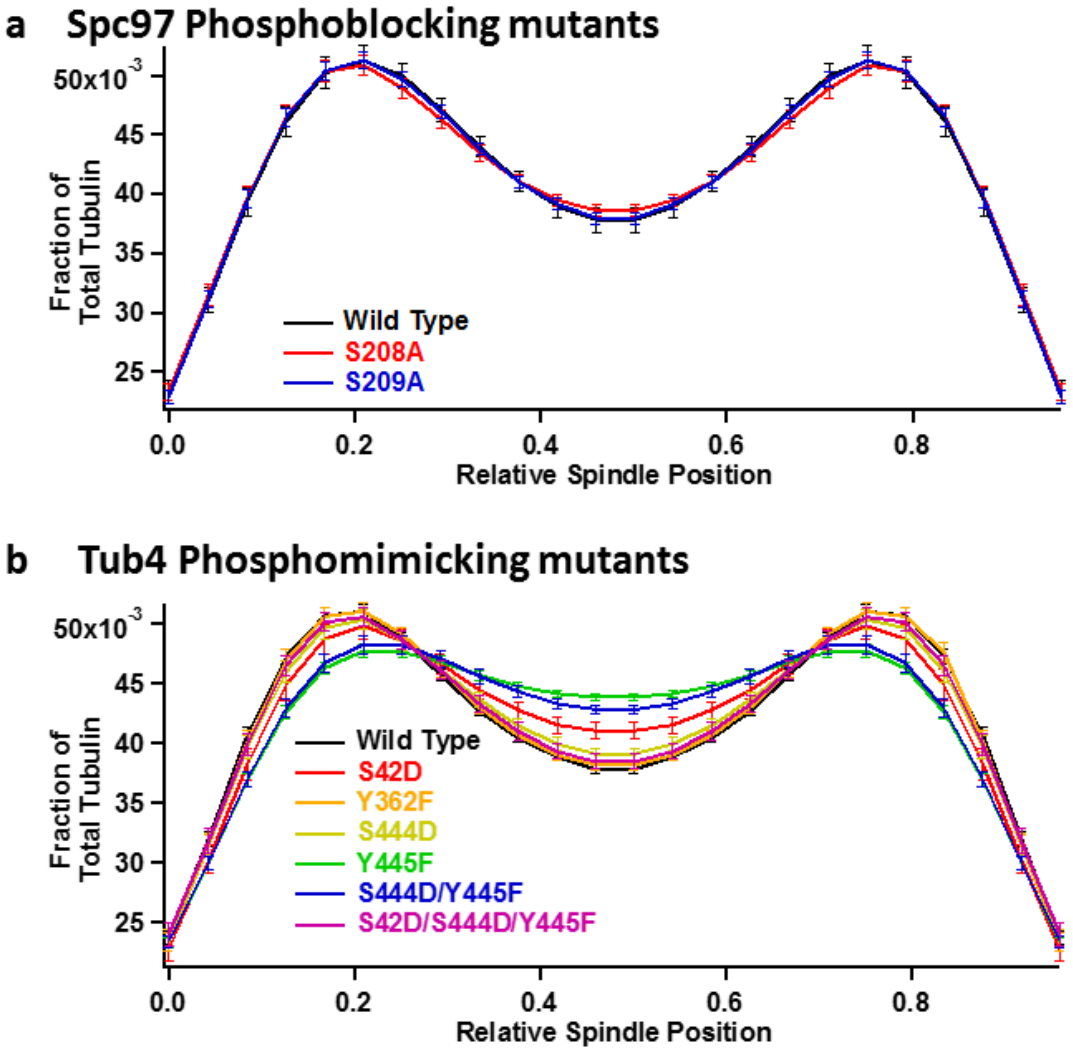

Figure 4.8. **Distribution of tubulin fluorescence across a metaphase spindle.** Metaphase spindles were identified as spindles 1.28-1.59 μm (20-25 pixels) between spindle poles. Tubulin fluorescence was measured across the length of the half spindle, then mirrored to complete the distribution.

Table 4.1. Strains used in this study.

Strain	Genotype	Reference
W303	*ade2-1oc can1-100 his3-11, 15 leu2-3,112 trp1-1 ura3-1*	
KGY315	*MATa/MATα ade2-1oc/ade2-1oc ADE3/ade3Δ-100 can1-100/can1-100 CYH2s/cyh2r his3-11,15/his3-11,15 leu2-3,112/leu2-3,112 trp1-1/trp1-1 ura3-1/ura3-1*	Greenland *et al.*, 2010
LAY57-1B	*MATα SPC110-TAP::kanMX*	Luther Arms
BGY64-1B	*MATa SPC72-TAP::kanMX*	Beth Graczyk
BGY68-16A	*MATa SPC42-GFP::kanMX SPC97-TAP::kanMX*	Beth Graczyk
BGY69-1B	*MATα NBP1-TAP::kanMX*	Beth Graczyk
BGY70-2B	*MATa BBP1-TAP::kanMX*	Beth Graczyk
BGY72-8A	*MATa SPC42-mCherry::hphMX SPC97-TAP::kanMX*	Fong *et al.*, 2016
BGY74-17B	*MATα SPC42-mCherry::hphMX SPC97-TAP::kanMX TUB4-GFP::kanMX*	Fong *et al.*, 2016
TAP-CNM67	*MATa TAP-CNM67::kanMX*	Beth Graczyk
SPC97-TAP	*MATa SPC97-TAP::kanMX*	Beth Graczyk
KFY37-4C	*MATa ade3Δ-100 LEU2::GFP-TUB1 lys2Δ::HIS3 SPC42-mCherry::hphMX spc98Δ::kanMX* pKF12	This study
KFY38-5C	*MATa ade3Δ-100 LEU2::GFP-TUB1 lys2Δ::HIS3 SPC42-mCherry::hphMX spc97Δ::TRP1* pTN25	This study
KFY75	*MATa ade3Δ-100 LEU2::GFP-TUB1 lys2Δ::HIS3 SPC42-mCherry::hphMX spc98(S109A)*	This study
KFY76	*MATa ade3Δ-100 LEU2::GFP-TUB1 lys2Δ::HIS3 SPC42-mCherry::hphMX spc98(S124A)*	This study
KFY77	*MATa ade3Δ-100 LEU2::GFP-TUB1 lys2Δ::HIS3 SPC42-mCherry::hphMX spc98(S136A)*	This study
KFY78	*MATa ade3Δ-100 LEU2::GFP-TUB1 lys2Δ::HIS3 SPC42-mCherry::hphMX spc98(S144A)*	This study
KFY79	*MATa ade3Δ-100 LEU2::GFP-TUB1 lys2Δ::HIS3 SPC42-mCherry::hphMX spc98(S159A)*	This study
KFY80	*MATa ade3Δ-100 LEU2::GFP-TUB1 lys2Δ::HIS3 SPC42-mCherry::hphMX spc98(Y438F)*	This study
KFY81	*MATa ade3Δ-100 LEU2::GFP-TUB1 lys2Δ::HIS3 SPC42-mCherry::hphMX spc98(Y510F)*	This study
KFY82	*MATa ade3Δ-100 LEU2::GFP-TUB1 lys2Δ::HIS3 SPC42-mCherry::hphMX spc98(S524A)*	This study
KFY83	*MATa ade3Δ-100 LEU2::GFP-TUB1 lys2Δ::HIS3 SPC42-mCherry::hphMX spc98(S531A)*	This study
KFY84	*MATa ade3Δ-100 LEU2::GFP-TUB1 lys2Δ::HIS3 SPC42-mCherry::hphMX spc98(S705A)*	This study
KFY85	*MATa ade3Δ-100 LEU2::GFP-TUB1 lys2Δ::HIS3 SPC42-mCherry::hphMX spc98(S109A/S136A)*	This study

KFY86	*MATa ade3Δ-100 LEU2::GFP-TUB1 lys2Δ::HIS3 SPC42-mCherry::hphMX spc98(S109A/S136A/S524A)*	This study
KFY87	*MATa ade3Δ-100 LEU2::GFP-TUB1 lys2Δ::HIS3 SPC42-mCherry::hphMX spc98(S109A/S136A/S524A/S531A)*	This study
KFY194	*MATa ade3Δ-100 LEU2::GFP-TUB1 lys2Δ::HIS3 SPC42-mCherry::hphMX spc97(S208A/S209A)::URA3* pTN25	This study
KFY196	*MATa ade3Δ-100 LEU2::GFP-TUB1 lys2Δ::HIS3 SPC42-mCherry::hphMX spc97(S208D/S209D)::URA3*	This study
KFY198	*MATa ade3Δ-100 LEU2::GFP-TUB1 lys2Δ::HIS3 SPC42-mCherry::hphMX spc98(S109A/S136A/S524A/S531A)::URA3*	This study
KFY200	*MATa ade3Δ-100 LEU2::GFP-TUB1 lys2Δ::HIS3 SPC42-mCherry::hphMX spc98(S109D/S136D/S524D/S531D)::URA3*	This study
KFY220-1A	*MATα ade3Δ-100 LEU2::GFP-TUB1 lys2Δ::HIS3 SPC42-mCherry::hphMX tub4Δ::kanMX* pLA6	This study
KFY229	*MATa ade3Δ-100 LEU2::GFP-TUB1 lys2Δ::HIS3 SPC42-mCherry::hphMX spc97(S208A)::URA3*	This study
KFY230	*MATa ade3Δ-100 LEU2::GFP-TUB1 lys2Δ::HIS3 SPC42-mCherry::hphMX spc97(S209A)::URA3*	This study
KFY232	*MATα ade3Δ-100 LEU2::GFP-TUB1 lys2Δ::HIS3 SPC42-mCherry::hphMX tub4(S42D)::URA3*	This study
KFY233	*MATα ade3Δ-100 LEU2::GFP-TUB1 lys2Δ::HIS3 SPC42-mCherry::hphMX tub4(S360D)::URA3*	This study
KFY235	*MATα ade3Δ-100 LEU2::GFP-TUB1 lys2Δ::HIS3 SPC42-mCherry::hphMX tub4(S444D/Y445E)::URA3*	This study
KFY236	*MATα ade3Δ-100 LEU2::GFP-TUB1 lys2Δ::HIS3 SPC42-mCherry::hphMX tub4(S42D/Y362E/S444D)::URA3*	This study
KFY237	*MATα ade3Δ-100 LEU2::GFP-TUB1 lys2Δ::HIS3 SPC42-mCherry::hphMX tub4(S444D)::URA3*	This study
KFY238	*MATα ade3Δ-100 LEU2::GFP-TUB1 lys2Δ::HIS3 SPC42-mCherry::hphMX tub4(Y445E)::URA3*	This study
KFY313-33D	*MATa CDC20-AID::kanMX PDS1-myc18::LEU2 ura3::pADH1-OsTIR1-9myc::URA3 SPC42-mCherry::hphMX SPC97-TAP::kanMX*	This study
KFY332-12C	*cdc4-1 SPC42-mCherry::hphMX SPC97-TAP::kanMX*	This study
TNY65-2B	*MATa ade3Δ-100 lys2Δ::HIS3 spc97Δ::TRP1* pTN25	Thu Nguyen

Table 4.2. Plasmids used in this study.

Plasmid	Relevant Markers	Reference
pRS316	*CEN6 ARSH4 URA3 Amp^r* f1 origin	Sikorski and Hieter, 1989
pRS306	*URA3* f1 origin	Sikorski and Hieter, 1989
pKF12	*SPC98 ADE3 LYS2* 2µm origin	This study
pKF33	*SPC98* in pRS306	This study
pKF35	*SPC98* in pRS316	This study
pKF56	*SPC97* in pRS316	This study
pKF64	*spc98(S109A/S136A)* in pRS316	This study
pKF65	*spc98(N423A/E424A)* in pRS316	This study
pKF79	*spc98(S109A)* in pRS316	This study
pKF80	*spc98(S124A)* in pRS316	This study
pKF81	*spc98(S136A)* in pRS316	This study
pKF82	*spc98(S144A)* in pRS316	This study
pKF83	*spc98(S159A)* in pRS316	This study
pKF84	*spc98(Y438F)* in pRS316	This study
pKF85	*spc98(Y510F)* in pRS316	This study
pKF86	*spc98(S524A)* in pRS316	This study
pKF87	*spc98(S531A)* in pRS316	This study
pKF88	*spc98(S705A)* in pRS316	This study
pKF89	*spc98(S109A/S136A/S524A)* in pRS316	This study
pKF90	*spc97(S208A)* in pRS316	This study
pKF91	*spc97(S209A)* in pRS316	This study
pKF92	*spc97(Y429F)* in pRS316	This study
pKF93	*spc97(S510A)* in pRS316	This study
pKF94	*spc97(T540V)* in pRS316	This study
pKF95	*spc97(S208A/S209A)* in pRS316	This study
pKF98	*spc98(S109A/S136A/S524A/S531A)* in pRS316	This study
pKF120	*spc98(S109A)* in pRS306	This study
pKF121	*spc98(S124A)* in pRS306	This study
pKF122	*spc98(S136A)* in pRS306	This study
pKF123	*spc98(S144A)* in pRS306	This study
pKF124	*spc98(S159A)* in pRS306	This study
pKF125	*spc98(Y438F)* in pRS306	This study
pKF126	*spc98(Y510F)* in pRS306	This study
pKF127	*spc98(S524A)* in pRS306	This study
pKF128	*spc98(S531A)* in pRS306	This study
pKF129	*spc98(S705A)* in pRS306	This study
pKF130	*spc98(S109A/S136A)* in pRS306	This study
pKF131	*spc98(S109A/S136A/S524A)* in pRS306	This study
pKF134	*spc97(Y429F)* in pRS306	This study
pKF135	*spc97(S510A)* in pRS306	This study
pKF136	*spc97(T540V)* in pRS306	This study

pKF137	*spc97(S208A/S209A)* in pRS306	This study
pKF138	*spc98(S109A/S136A/S524A/S531A)* in pRS306	This study
pKF139	*spc98(S109A/S136A/S531A)* in pRS306	This study
pKF140	*spc98(S109A/S136A/S531A)* in pRS316	This study
pKF159	*spc98(S109D/S136D/S524D)* in pRS306	This study
pKF160	*spc98(S109D/S136D/S524D)* in pRS316	This study
pKF161	*spc97(S208D/S209D)* in pRS316	This study
pKF162	*tub4(S42A/S360A/Y362F/S444A/Y445F) in pRS315*	This study
pKF163	*spc98(S109D/S136D/S524D/S531D)* in pRS306	This study
pKF164	*spc98(S109D/S136D/S524D/S531D)* in pRS316	This study
pKF169	*tub4(S42A/S360A/Y362F/S444A/Y445F) in pRS306*	This study
pKF170	*tub4(S42D/S360D/Y362E/S444D/Y445E) in pRS306*	This study
pKF191	*spc97(S208A) in pRS306*	This study
pKF192	*spc97(S209A) in pRS306*	This study
pKF193	*tub4(S42A) in pRS306*	This study
pKF194	*tub4(S42D) in pRS306*	This study
pKF195	*tub4(S360A) in pRS306*	This study
pKF196	*tub4(S360D) in pRS306*	This study
pKF197	*tub4(Y362F) in pRS306*	This study
pKF198	*tub4(Y362E) in pRS306*	This study
pKF199	*tub4(S444D) in pRS306*	This study
pKF200	*tub4(Y445E) in pRS306*	This study
pKF201	*tub4(S444A/Y445F) in pRS306*	This study
pKF202	*tub4(S444D/Y445E) in pRS306*	This study
pKF203	*tub4(S42D/Y362E/S444D) in pRS306*	This study
pLA6	*TUB4 ADE3 LYS2* 2μm origin	Luther Arms
pSB2065	*3V5-IAA7-kanMX Amp^r* f1 origin	Sue Biggins
pTN25	*SPC97 ADE3* 2μm origin	Thu Nguyen

Table 4.3. Strain Purification Summary.

TAP-tagged Protein	Viability	SPBs Bind to Beads	SPBs Cleave from Beads	SPB Yield
Bbp1-TAP	+	+	-	Low
TAP-Cnm67	+	++	+	Low
Mlp2-TAP	+	+	+	Low
Nbp1-TAP	+	-	-	Low
Spc42-TAP	-	N/A	N/A	N/A
Spc72-TAP	+	+	+	Low
Spc97-TAP	+	+++	+++	High
Spc110-TAP	+	++	+	Low

Table 4.4. Protein coverages (%) for new phosphoproteome data set.

	Asynchronous SPBs			Cdc20-AID SPBs		*cdc4-1* SPBs	
Bbp1	66.75	52.21	0.00	40.52	17.66	78.44	69.87
Cdc31	71.43	52.17	44.10	51.55	46.58	72.05	73.91
Cmd1	63.27	49.66	33.33	49.66	46.94	63.27	63.27
Cnm67	70.74	57.49	45.78	54.73	70.74	74.35	69.02
Kar1	62.59	40.18	0.00	29.33	29.10	68.59	60.74
Mps2	48.84	38.76	0.00	31.27	6.98	68.73	58.91
Mps3	48.97	28.74	2.05	23.90	19.79	59.38	51.32
Nbp1	52.66	39.81	0.00	32.29	21.00	53.29	51.72
Ndc1	34.66	20.15	0.00	16.79	18.63	54.66	37.56
Nud1	49.35	35.96	27.85	28.08	61.57	74.5	56.99
Sfi1	40.80	22.73	0.00	14.69	6.66	39.53	31.4
Spc29	75.89	49.41	13.83	59.68	68.77	75.89	68.38
Spc42	76.58	51.52	27.00	56.47	69.42	81.82	79.34
Spc72	57.72	40.03	42.28	31.51	66.88	69.45	61.25
Spc97	51.52	41.07	45.44	35.24	72.78	72.17	62.33
Spc98	42.20	34.52	28.72	28.96	52.36	60.99	49.17
Spc110	69.28	57.84	31.36	54.03	57.42	74.79	71.61
Tub4	46.30	9.94	19.87	20.51	62.16	68.08	51.59

Table 4.5. Phosphorylation sites determined by new data set.
("?" denote ambiguous assignments)

Centrosome protein	Site	Asynchronous SPBs	Mitotic (Cdc20-AID) SPBs	G1 (cdc4-1) SPBs
Bbp1	T7			+
	S(P)29	+		+
	S54	+		+
	S73	+		+
	S112	+		
	S(P)115	+	+	+
	S148 or S150	+		+
	S(P)194	+		+
	T309	+		
Cdc31	T128 or T130			+
Cmd1				
Cnm67	S(P)17	+	+	+
	S20	+	+	+
	S61		+	
	S66		+	
	Y67			+
	S(P)72	+		+
	S74	+		
	S85	+	+	+
	S89	+	+	+
	S(P)103	+	+	+
	S120	+	+	+
	T(P)121	+	+	+
	S138			+
	T142, T146 or S147		+	+
	S151		+	
Kar1	T4			+
	S5			+
	S35			+
	T119			+
	S130	+		+
	T(P)149	+		
	S(P)216	+		+

	S221 or T222			+
	S284			+
	S293	+		
Mps2	S121 or S123			+
	S140	+	?	?
	T(P)141	?	?	+
	S(P)149	+		
	S(P)232	+		+
Mps3	S70	+	+	+
	Y403			+
	S404			+
	T615			+
	T634			+
Nbp1	S97	+		+
	T107			+
	S119		+	
	S219 or S220	+		
	S234			
	S(P)151	+		
	S169		+	+
	S234			+
	S260	+	+	
	S264	+	+	?
	S(P)287	+		
	T(P)292	+		+
Ndc1	S(P)401	+		+
	S412	+		+
Nud1	T5	+		+
	S11 or S12			+
	S42		?	
	S49		+	
	S52		?	
	S77	+		
	S109		+	
	T121		+	+
	S140	+	+	+
	T145	+		
	T169	+		
	S171	+		+
	S213	+		?

	S240	+	+	+
	S352	+		
	S385 or T(P)388	+	+	+
	T(P)392	+	+	+
	S417	+	+	+
	S419	+	+	+
	S421	+		
	S443		?	?
	S445		+	
	S450	+	+	+
	S(P)469	+	+	+
	T(P)806		+	
	T814 or S815		+	
	T(P)843		+	
Sfi1	S10	+		
	T30	+		
	S42	+		?
	S109	+		+
	T(P)816	+		
	S920	+		
Spc29	Y3 or S4		+	
	T18	+	+	+
	S40	+		?
	T42	+	+	+
	S43	+		+
	S58	+	+	+
	S(P)59	+	+	+
	S(P)65	+		
	S(P)77	+	+	+
	S(P)121			+
	S187			+
	S189		+	+
	S191	+		
	S230			+
	S231			+
	T240	+	+	+
	S249		+	
	S250	+	+	
Spc42	T(P)32	+		

	S43	+		+
	S130	+		?
	T131	+		+
	S151	+	+	+
	Y154			+
	S204	?		+
	S(P)213	+	+	+
	S(P)217	+	+	?
	S284	+	+	+
	S294			+
	S(P)326	+	+	+
	S326, S328, or S329		+	+
	S352	+		+
	T354	+		?
	T(P)357	+	+	+
	T(P)359	+		
Spc72	S47 or S48	+	+	+
	S231			+
	S232			+
	S236			+
	T291		+	+
	T294	+	+	+
	S348, S349, or S350		+	+
	S350		+	
	S368	+		
	S370	+		
	S413		+	?
	S430		+	+
	S618	+		
Spc97	S84			+
	T88			+
	S130	+		
	S208	+	?	+
	S209	+	+	+
Spc98	S109		+	
	S(P)124	+	+	+
	S130	+		
	T133			+
	S136	+	+	+

	S148		+	
	S151 or S152		+	+
Spc110	S5	+		+
	T(P)18	+	+	
	S(P)36	+		+
	T38	+		+
	S60	+	+	+
	S72	+		+
	S75	+		+
	S80	+	+	
	S(P)91	+	+	+
	T182		+	+
	Y186			+
	T188			+
Tub4	S37		+	
	S42, S43, or T44			+
	S71			+
	S373			+
	S378 or S381			+
	Y407			+
	S415			+

Table 4.6. Phosphorylation sites determined by reanalysis of Keck *et al*, 2011 published data.

Centrosome protein	Site	Asynchronous SPBs	Mitotic (Cdc20 depleted) SPBs	G1 (α factor) SPBs
Bbp1	S29	+	+	
	S51		+	
	S54	+	+	
	S71	+		
	S112		+	
	S(P)115	+	+	+
	S(P)194	+	+	
	T309		+	
	S310		+	
	S375	+	+	
	S378	+	+	
Cdc31	S6 or S7	+	+ (S7)	+ (S6)
Cmd1	S(P)43 or S45	+		
Cnm67	T2		+	
	S(P)17	+	+	+
	S20	+	+	+
	S61	+	+	
	S66	+	+	
	S(P)72	+	+	+
	S74	+	+	
	T84	+	?	
	S85		+	
	Y86		+	
	S(P)89	+	+	+
	S(P)103	+	+	
	S120		+	
	T(P)121	+	+	+
	S126		+	
	T142	+		
	T146	+	+	
	S(P)147	+	+	
	S151	+	+	
Kar1	S130	+	+	
	T(P)149		+	
	S(P)216	+		

	S219		+	
Mps2	S123	+		
	S(P)121 or S123		+	
	T(P)141	+	+	+
	S228	+		
	S(P)232)	+		
Mps3				
Nbp1	S119		+	
	S220	+	+	
	S225		+	
	S(P)251		+	
	S(P)253		+	
	S260	+	+	
	S(P)265	+	+	
	S(P)287		+	
	T(P)292	+	+	
Ndc1	S412	+	+	
Nud1	S42	+	+	
	S49		+	
	T52		+	
	S53		+	
	S63		+	
	S77		+	
	T78		+	
	S88	+		
	S94		+	
	S109	+	+	
	S133		+	
	S140	+	+	
	S145		+	
	T147		+	
	T169		+	
	S171		+	
	S187		+	
	S189	+	+	
	S192	+	+	
	S194	+	+	
	S222	+	+	
	S240	+	+	
	T259 or S260	+		

	S262	+		
	S385	+	+	
	T(P)388	+	+	+
	T(P)392	+	+	+
	T400	+		
	S417	+	?	
	S419	+	+	
	T442	+	+	
	S443	+	+	
	S445	+	+	
	T449	+	+	
	S450	+	+	+
	T454	+	+	
	S(P)469	+	+	+
	T(P)806		+	
	T(P)843		+	
Sfi1	S(P)24	+	+	
	T26	+	+	
	T30	+	+	
	S42	+		
	S109	+		
	S(P)923	+		
Spc29	T18	+	+	
	S39		+	
	S40		+	
	T42	+	+	+
	S43		+	
	S58 or S(P)59		+	
	S(P)65		+	
	S(P)77	+	+	
	S120		+	
	S121		+	
	S167	+		
	S187		+	
	S189		+	
	S191	+		
	T195	+		
	S217	+		
	S230 or S231		+	
	S239	+	+	+
	T240	+	+	+

	S250	+	+	
Spc42	S29	+	+	
	T(P)32	+	+	+
	T131	+	+	
	S151	+	+	+
	T168		+	
	S195	+	+	+
	S204	+	+	
	S(P)213	+	+	+
	S(P)217	+	+	+
	T221	+	+	+
	S246	+		
	S284	+	+	+
	S294	+	+	
	S319	+		
	S321	+	+	
	S322		+	
	T325 or S(P)326	+	+	+
	S328	+	+	
	S329	+	+	+
	S352	+	+	+
	T354	+	+	
	T(P)357	+	+	+
	T(P)359	+	+	+
Spc72	S29		+	
	S48		+ (S48)	
	S231		+	
	S(P)232	+	+	
	T291	+	+	
	T294	+	+	
	S349		+	
	S350		+	
	S413		+	
	S430		+	
	S618	+	+	
Spc97	S208		+	+
	S209		+	
Spc98	S136		+	
Spc110	T(P)18	+	+	
	T30		+	

	T32		+	
	S(P)36	+	+	
	T38	+	+	+
	S60	+	+	+
	T64	+		+
	S67	+		
	T68	+		
	S72	+	+	
	S75	+	+	
	S80	+	+	
	S(P)91	+	+	+
	S153		+	
	S156	+	+	
	S261		+	
	S639		?	
	Y869		+	
	S871		+	
Tub4				

Table 4.7. Phosphorylation sites common among all data sets.

Asynchronous	Mitotic	Alpha Factor	Cdc4-1 Arrest
Bbp1 S(P)29	Bbp1 S(P)115	Bbp1 S(P)115	Bbp1 T7
Bbp1 S54	Cnm67 S(P)17	Cnm67 S(P)17	Bbp1 S(P)29
Bbp1 S(P)115	Cnm67 S20	Cnm67 S20	Bbp1 S54
Bbp1 S(P)194	Cnm67 S61	Cnm67 S(P)72	Bbp1 S73
Cnm67 S(P)17	Cnm67 S66	Cnm67 S(P)89	Bbp1 S(P)115
Cnm67 S20	Cnm67 S85	Cnm67 T(P)121	Bbp1 S150
Cnm67 S(P)72	Cnm67 S(P)89	Mps2 T(P)141	Bbp1 S(P)194
Cnm67 S74	Cnm67 S(P)103	Nud1 T(P)388	Bbp1 S29
Cnm67 S(P)89	Cnm67 T(P)121	Nud1 T(P)392	Cnm67 S(P)17
Cnm67 S(P)103	Cnm67 S151	Nud1 S450	Cnm67 S20
Cnm67 T(P)121	Nbp1 S260	Nud1 S(P)469	Cnm67 Y67
Kar1 S130	Nud1 S49	Spc29 T42	Cnm67 S(P)72
Kar1 S(P)216	Nud1 S109	Spc29 S239	Cnm67 S85
Mps2 S(P)232	Nud1 S140	Spc29 T240	Cnm67 S(P)89
Nbp1 S260	Nud1 S240	Spc42 T(P)32	Cnm67 S(P)103
Nbp1 T(P)292	Nud1 T(P)392	Spc42 S151	Cnm67 S120
Ndc1 S412	Nud1 S419	Spc42 S(P)213	Cnm67 T(P)121
Nud1 S140	Nud1 S445	Spc42 S(P)217	Cnm67 S138
Nud1 S240	Nud1 S450	Spc42 T221	Cnm67 T146
Nud1 T(P)392	Nud1 S(P)469	Spc42 S284	Cnm67 S(P)147
Nud1 S417	Nud1 T(P)806	Spc42 S329	Cnm67 T146
Nud1 S450	Nud1 T(P)843	Spc42 S352	Kar1 T4
Nud1 S(P)469	Spc29 T18	Spc42 T(P)357	Kar1 S5
Sfi1 T30	Spc29 T42	Spc42 T(P)359	Kar1 S35
Sfi1 S109	Spc29 S(P)77	Spc110 T38	Kar1 T119
Spc29 T18	Spc29 S189	Spc110 S60	Kar1 S130
Spc29 T42	Spc29 T240	Spc110 T64	Kar1 S(P)216
Spc29 S(P)77	Spc29 S250	Spc110 S(P)91	Kar1 S221
Spc29 S191	Spc42 S151		Kar1 S284
Spc29 T240	Spc42 S(P)213		Kar1 S221 or T224
Spc29 S250	Spc42 S(P)217		Kar1 T119
Spc42 T(P)32	Spc42 S284		Mps2 S(P)121
Spc42 T131	Spc42 T(P)357		Mps2 T(P)141
Spc42 S151	Spc72 T291		Mps2 S(P)232
Spc42 S(P)213	Spc72 S350		Mps2 S232
Spc42 S(P)217	Spc72 S413		Mps3 S70
Spc42 S284	Spc72 S430		Mps3 Y403

Spc42 S352	Spc97 S209		Mps3 S404
Spc42 T354	Spc98 S136		Mps3 T615
Spc42 T(P)357	Spc110 T(P)18		Mps3 T634
Spc42 T(P)359	Spc110 S60		Nbp1 S97
Spc72 T294	Spc110 S80		Nbp1 T107
Spc72 S618	Spc110 S(P)91		Nbp1 S169
Spc110 T(P)18			Nbp1 S234
Spc110 S(P)36			Nbp1 S(P)265
Spc110 T38			Nbp1 T(P)292
Spc110 S60			Ndc1 S(P)401
Spc110 S72			Ndc1 S412
Spc110 S75			Nud1 T5
Spc110 S80			Nud1 S11 or S12
Spc110 S(P)91			Nud1 T121
			Nud1 S140
			Nud1 S171
			Nud1 S240
			Nud1 S385
			Nud1 T(P)388
			Nud1 T(P)392
			Nud1 S417
			Nud1 S419
			Nud1 S450
			Nud1 S(P)469
			Sfi1 S109
			Spc29 T18
			Spc29 T42
			Spc29 S43
			Spc29 S58
			Spc29 S(P)59
			Spc29 S(P)77
			Spc29 S(P)121
			Spc29 S187
			Spc29 S189
			Spc29 S230
			Spc29 S231
			Spc29 T240
			Spc29 S58
			Spc42 S43
			Spc42 T131

			Spc42 S151
			Spc42 Y154
			Spc42 S204
			Spc42 S(P)213
			Spc42 S284
			Spc42 S294
			Spc42 S(P)326
			Spc42 S352
			Spc42 T(P)357
			Spc42 S204
			Spc42 S352
			Spc72 S47 or S48
			Spc72 S231
			Spc72 S(P)232
			Spc72 S236
			Spc72 T291
			Spc72 T294
			Spc72 S350
			Spc72 S430
			Spc72 S231 or S236
			Spc97 S84
			Spc97 T88
			Spc97 S208
			Spc97 S209
			Spc97 S219
			Spc98 S(P)124
			Spc98 T133
			Spc98 S136
			Spc98 S151
			Spc98 S(P)152
			Spc110 S5
			Spc110 S(P)36
			Spc110 T38
			Spc110 S60
			Spc110 S72
			Spc110 S75
			Spc110 S(P)91
			Spc110 T182
			Spc110 Y186

			Spc110 T188
			Tub4 S71
			Tub4 S373
			Tub4 S378 or S381
			Tub4 Y407
			Tub4 S415

Chapter 5

Biophysical measurements of microtubule attachment strength to yeast spindle pole bodies

Introduction

Centrosomes must sustain mechanical loads exerted on them by nucleated microtubules of the mitotic spindle. In budding yeast, the centrosome equivalent is the spindle pole body, which experiences tension on both the nuclear face and the cytoplasmic face. Within the nucleus, interpolar microtubules are organized by molecular motors to maintain the length and structural integrity of the spindle by sliding microtubules in relation to one another (Dumont and Mitchison, 2009; Goshima and Scholey, 2010; Cross and McAinsh, 2014; van Heesbeen *et al.*, 2014; Shimamoto *et al.*, 2015). The kinetochore microtubules from opposite poles attach to sister centromeres to biorient the chromosomes, resulting in tension at the kinetochore (Liu and Lampson, 2009; Umbreit and Davis, 2012). In the cytoplasm, microtubules extend towards the cell cortex, where dynein and kinesins exert force on the microtubule to position the nucleus in the bud neck (Morris, 2000; Laan *et al.*, 2012; Nicholas *et al.*, 2015). Not only is the balance of these forces necessary for high fidelity in chromosome segregation, these forces might also serve as signals for progression through the cell cycle, thereby making the spindle pole body a possible site of mechano-regulation. While the forces sustained by yeast kinetochore attachments to microtubules have been well studied *in vitro* (Powers *et al.*, 2009; Akiyoshi *et al.*, 2010; Franck *et al.*, 2010; Tien *et al.*, 2010; Umbreit *et al.*, 2012; Sarangapani *et al.*, 2014), the mechanics of spindle pole body-microtubule attachments remains largely unstudied.

The budding yeast spindle pole body is the microtubule organizing center of the cell, responsible for the nucleation of microtubules and the organization of the bioriented mitotic spindle. The spindle pole body is a cylindrical structure embedded in the nuclear envelope throughout the cell cycle, comprised of three layers: the inner plaque in the nucleus, the central plaque embedded in the nuclear envelope and the outer plaque in the cytoplasm. The essential microtubule nucleation complex, the γ-tubulin small complex, is anchored to the core of the spindle pole body via interactions with Spc110 on the nuclear face and Spc72 on the cytoplasmic face (Knop and Schiebel, 1997, 1998; Sundberg and Davis, 1997; Nguyen *et al.*, 1998; Souès and Adams, 1998). Because Spc110 plays such an integral role in attaching nuclear microtubules to the spindle pole body, it has been studied extensively, generating many mutants with diverse mitotic defects related to spindle integrity. Many of these mutant phenotypes also allude to perturbations in the force balance of the spindle (Geiser *et al.*, 1993; Kilmartin *et al.*, 1993; Spang *et al.*, 1996b; Stirling and Stark, 1996; Sundberg and Davis, 1997; Nguyen *et al.*, 1998; Yoder *et al.*, 2005).

Two temperature sensitive mutant alleles of *SPC110*, *spc110-221* and *spc110-226*, were identified in a PCR mutagenesis screen mapping to two distinct functional regions of *SPC110* (Sundberg and Davis, 1997). Even though they are alleles of the same gene, *spc110-221* and *spc110-226* complement each other suggesting that they induce different phenotypes at the spindle pole body. The N-terminal allele, *spc110-221*, contains nine mutations between amino acids 1 and 163 and inhibits interaction between Spc110 N-terminus and the γ-tubulin small complex (Sundberg and Davis, 1997; Nguyen *et al.*, 1998). The C-terminal mutant allele, *spc110-226*, contains five mutations between amino acids 772 and 836 of Spc110, a region important for cell viability (Geiser *et al.*, 1993; Kilmartin *et al.*, 1993; Sundberg and Davis,

1997). This allele disrupts interactions between Spc110 and the other components of the central plaque, Spc29 and Spc42, and increases the susceptibility pole to increased tension caused by kinetochore mutation *dam1-765* (Sundberg and Davis, 1997; Yoder *et al.*, 2005; Shimogawa *et al.*, 2006). Calmodulin is required for assembly of the spindle pole body but how it contributes to its strength is unknown. Another mutant allele of *SPC110, spc110-407,* is a truncation that eliminates the calmodulin binding site of Spc110 and relieves the requirement for calmodulin in assembly of the spindle pole body (Geiser *et al.*, 1993). This allele provides a way to measure whether calmodulin also contributes to the strength of the spindle pole body.

With the adaptation of laser trapping experiments to study the attachment strength of a microtubule to the spindle pole body, we present the first measurements of forces sustained at the centrosome. Since tension across the mitotic spindle is thought to play a role in signaling the spindle assembly checkpoint (Liu and Lampson, 2009; Umbreit and Davis, 2012; Wang *et al.*, 2014), we wanted to determine if mutant alleles of *SPC110* affected forces sustained at the spindle pole body. The three Spc110 mutants each have a distinct phenotype, but all suggest that Spc110 plays an integral role in force transduction through the spindle pole body. Here, we study the forces each mutant can withstand and provide physical measurements to explain the *in vivo* phenotypes.

Materials and methods

Strains, plasmids, and media

All of the strains used in this study are derived from W303 and are listed in Table 5.1. C-terminally tagged Spc97-TAP was created by PCR amplifying the *TAP-kanMX* cassette from the plasmid TAP-2xPA using primers that shared homology with the flanking sequences of the stop codon. C-terminal Spc42-mCherry was created by PCR amplification of the *mCherry-hphMX3* cassette from pBS35 (gift from the Yeast Resource Center, University of Washington, Seattle, WA). For the Spc72-AID strain, the auxin degron IAA7 was PCR amplified from pSB2065 (gift from Sue Biggins, Fred Hutchinson Cancer Research Center, Seattle, WA) with primers that shared homology with the flanking DNA of the stop codon. The above cassettes were each integrated into a diploid strain, KGY315, and verified by PCR. Diploids were sporulated and dissected for haploids containing the tagged copy of the gene. YPD media is as described (Burke *et al.*, 2000).

TAP purification and velocity sedimentation

Spindle pole bodies were purified by a TAP-tag on Spc97, as previously described (Chapter 2). Sucrose gradients were generated by allowing five steps of sucrose solutions (200 µl each of 10%, 20%, 30%, 40%, 2.5 M sucrose in 10 mM Bis-Tris, pH 6.5, 0.1 mM $MgCl_2$) to equilibrate at 4^{o}C for 2 hours. The TEV eluate was then applied to the sucrose gradient and spun at 50,000 rpm for 5 hours at 4^{o}C in a TLS55 rotor (Beckman Coulter). Fractions (90 µl) were removed from the top of the gradient with wide-bore tips. The presence of SPBs was determined by western blot analysis, probing for Spc110 and Spc97.

For *spc110-221* and *spc110-226* spindle pole bodies grown at the permissive temperature, cells were grown at 25°C to 150 Klett units before harvesting. For *spc110-221* and *spc110-226* spindle pole bodies grown at the restrictive temperature, cells were grown at 25°C to 60 Klett units and shifted to the restrictive temperature of 37°C for three hours before harvesting at 160 Klett units. The cells grown at the restrictive temperature were arrested as large budded cells for both strains. Spc72-AID cells were grown to 100 Klett units. Auxin (indole-3-acetic acid; IAA) in DMSO was added to a final concentration of 1 mM. Spc72 was depleted for 1.5 generations before cells were harvested. In Spc72 depleted cells, ≥98% of cells were multibudded with multipolar spindles, as determined by fluorescence microscopy.

Laser trap instrument

The laser trap has been described previously (Akiyoshi *et al.*, 2010; Franck *et al.*, 2010; Sarangapani *et al.*, 2014). Position sensor response was mapped using the piezo stage to raster-scan a stuck bead through the beam, and trap stiffness was calibrated along the two principle axes using the drag force, equipartition, and power spectrum methods. Force feedback was implemented with custom LabView software. During rupture force measurements, bead-trap separation was sampled at 40 kHz while stage position was updated at 50 Hz to maintain the desired tension (force-clamp assay) or ramp-rate (force-ramp assay). Bead and stage position data were decimated to 200 Hz before storing to disk.

Kinesin purification

An N-terminal derivative of the *Drosophila melanogaster* kinesin heavy chain, DmK401, was purified as previously described (Asbury *et al.*, 2003). DmK401 consisted of a homodimer of the N-terminal 401 amino acids of the kinesin heavy chain with a hexa-histidine tag on the C-

terminus. DmK401 was expressed in BL21 Star (DE3) cells (Invitrogen). The cultures were grown at 20°C for 2 hours upon 1 mM IPTG induction. Rifampicin was added to a final concentration of 200 μM and cultures were grown overnight at 20°C. Cells were pelleted and resuspended in an equivalent volume of lysis buffer (250 mM potassium phosphate, pH 7.6, 10 mM imidazole, pH 7.0, 1 mM β-mercaptoethanol, 4 mM $MgCl_2$, Complete protease inhibitors (Roche)), lysed with a French Press, and clarified by ultracentrifugation at 50,000 rpm for 40 minutes at 4°C. The clarified lysate was mixed with an equivalent volume of glycerol and stored at -20°C.

Coverslip preparation for laser trap experiment

Streptavidin-coated polystyrene beads (0.44 μm in diameter, Spherotech) were functionalized with biotinylated anti-His_5 antibodies (Qiagen) and stored with continuous rotation at 4 °C in BRB80 (80 mM PIPES, 1 mM $MgCl_2$, and 1 mM EGTA, pH 6.9) supplemented with 8 mg/mL BSA for up to 3 months. Prior to each experiment, beads were decorated with kinesin by incubating 6 pM anti-His_5 beads for 60 min at 4°C with 20 μl of cleared lysate from the kinesin expression cells for one hour at 4°C, diluted in assay buffer (BRB80, concentration as above, 5 mg/ml BSA, 11.5 μM taxol and 1 mM DTT).

Flow chambers (~10 μL volume) were made using glass slides, double-stick tape, and KOH-cleaned coverslips. Briefly, two lengths of double-stick tape were placed across a microscope slide to create an inverted channel. A KOH-cleaned coverslip was placed over the inverted channel and sealed with pressure. It was then functionalized in the following manner. An aliquot of purified spindle pole bodies was diluted with 5X BRB80 (400 mM PIPES, 5 mM $MgCl_2$, and 5 mM EGTA), 40 mg/ml BSA, and 2.67 M KCl to a final concentration of BRB80, 8

mg/ml BSA and 500 mM KCl. The diluted spindle pole bodies were introduced into the flow chamber and allowed to nonspecifically adhere to the coverslip for 30 minutes. The spindle pole bodies were washed thoroughly by flowing in BRB80. Bovine brain tubulin, purified as previously described (Castoldi and Popov, 2003), was cleared of aggregates by ultracentrifugation at 90,000 rpm for 10 minutes at 4°C in a TLA100 rotor (Beckman Coulter). The tubulin polymerization buffer (BRB80, 1 mg/mg κ-casein, 5 mg/ml BSA, 2 μM taxol, 1 mM GTP, 1 mM DTT, and 20 μM cleared tubulin) was added to the flow cell and microtubules were allowed to nucleate at room temperature for several minutes. Free tubulin was washed out of the chamber with wash buffer (BRB80, 1 mg/ml κ-casein, 5 mg/ml BSA, 11.5 μM taxol, and 1 mM DTT). Kinesin-coated beads (described above) were then flowed in along with an oxygen scavenging system (500 μg/mL glucose oxidase, 60 μg/mL catalase, and 25 mM glucose). The edges of the flow chamber were sealed to prevent evaporation. All laser trap experiments were performed in temperature-controlled rooms, maintained at 23 °C.

For kinetochore rupture force experiments, mitotic kinetochore particles were isolated from budding yeast by affinity-purifying Dsn1–6His–3Flag protein, as previously described (Akiyoshi *et al.*, 2010) and linked to anti-His_5 antibody-functionalized polystyrene beads as previously described (Akiyoshi *et al.*, 2010; Sarangapani *et al.*, 2013, 2014). Briefly, prior to each experiment, beads were decorated with kinetochore particles by incubating 6 pM anti-His_5 beads for 60 min at 4°C with purified kinetochore material, corresponding to Dsn1-His-Flag concentrations of 6 nM. Finally, kinetochore particle-coated beads were introduced at an eight-fold dilution from the incubation mix in a solution of growth buffer containing 1.5 mg/ml purified bovine brain tubulin and an oxygen scavenging system, as described above.

Rupture force assay

Spindle pole body puncta were identified using the DIC imaging module (part of the laser trap set-up) and those that had microtubules emanating from them were specifically chosen for pulling experiments. Many of these microtubules had pre-bound beads (i.e. beads that were already associated with the spindle pole body-associated microtubule), but if no bead was bound to the microtubule, free beads from solution were trapped and allowed to bind to these microtubules. The beads were initially subjected to a preload force of ~ 5 pN. After a brief preload period, the laser trap was programmed to ramp the force at a constant rate of 5 pN/s until the microtubule detached from the spindle pole body punctum, the bead broke from the microtubule, or the load limit of the trap was reached (70-90 pN). Only those events that had a break at the spindle pole body-microtubule interface were used in the distributions or the calculated mean rupture force values.

For kinetochore rupture force experiments, the laser trap was used to place individual free beads close to the ends of growing microtubules to allow binding. Upon binding, the attachments were preloaded with a constant force of ~ 5 pN. After a brief preload period, during which we verified that the beads were moving at a rate consistent with that of microtubule growth, the laser trap was programmed to ramp the force at a constant rate (5 pN/s) until the linkage ruptured. Rupture events were recorded and analyzed to compute the mean rupture force of the kinetochore-microtubule attachments.

The *p*-values for comparison of mean rupture forces were computed by single-factor ANOVA. We employed the criterion that $p > 0.1$ indicates lack of statistical significance while $p < 0.05$ indicates a statistically significant difference between the compared means.

Results

Rupture force laser trapping assay was adapted to investigate spindle pole body-microtubule attachments

Laser trapping has been used extensively in the study of kinetochore attachments to microtubules (Powers *et al.*, 2009; Akiyoshi *et al.*, 2010; Franck *et al.*, 2010; Tien *et al.*, 2010; Umbreit *et al.*, 2012; Sarangapani *et al.*, 2014). The coverslip preparation was adapted for the nucleation of microtubules off of spindle pole bodies and the use of beads attached to the microtubule to exert force. Briefly, a flow chamber was constructed with a KOH-cleaned coverslip, double-stick tape, and a glass slide. Spindle pole bodies were allowed to nonspecifically adhere to the coverslip. Free tubulin was flowed in and allowed to nucleate off of spindle pole bodies in the presence of taxol. Unpolymerized tubulin was washed out and kinesin-decorated beads were flowed into the chamber and attached to taxol-stabilized microtubules (Figure 5.1.a). Puncta with nucleated microtubules were identified by DIC. Simultaneous imaging with total internal reflection fluorescence (TIRF) confirmed that the puncta were spindle pole bodies with Spc42-mCherry fluorescence and a microtubule, labeled with AlexaFluor 488 (ThermoFisher), was emanating from the spindle pole bodies (Figure 5.1.b).

Because microtubules are made of α- and β-tubulin heterodimers, microtubules have an intrinsic polarity. In cells, the minus end of the microtubule is attached to the spindle pole body and does not exhibit any dynamics. The plus end of the microtubule extends towards the chromosomes or the cell cortex and undergoes stochastic periods of polymerization and depolymerization, defined as dynamic instability (Mitchison and Kirschner, 1984). To confirm

that the microtubules were nucleated from spindle pole bodies and oriented in the correct manner, kinesin-decorated beads were allowed to walk along the microtubule. With the addition of ATP to the buffer as an energy source, the plus-end directed kinesin motors walked away from the spindle pole body for 97% of microtubules tested (n = 97), verifying that the minus ends of the microtubules were embedded in the spindle pole bodies.

There were three possible outcomes for these rupture force experiments: the spindle pole body-microtubule interface ruptured, the bead attachment to the microtubule ruptured, or the maximum force of the trap was exceeded. These three outcomes were tracked and recorded for each spindle pole body type, but only spindle pole body-microtubule breaks were used to calculate mean rupture forces (Table 5.2-Table 5.8). On average, 40.0% of rupture force experiments ended with a spindle pole body-microtubule break, 26.1% ended with a bead-microtubule break, and 33.8% ended by exceeding the load limit of the laser trap, referred to as escapes. The mean rupture force for the escapes was consistent throughout all experiments, averaging 65.3 pN ± 0.4 pN (Figure 5.2).

The attachment of microtubules to the nuclear face of wild type spindle pole bodies is stronger than the attachment of kinetochores to microtubules

Wild type spindle pole bodies were purified as described in Chapter 2. Measurement of wild type spindle pole body-microtubule attachment strength found that the mean rupture force was 45.4 pN ± 1.5 pN. When kinetochore attachments to microtubules were tested using the same ramp rate of 5 pN/s, the mean rupture force was determined to be 21.1 pN ± 2.1 pN, only half the strength of the spindle pole body attachment (Figure 5.3 and Tables 5.2 and 5.3).

Yeast cells undergo closed mitosis, that is, the nuclear envelope does not break down during mitosis. This means that the nuclear and the cytoplasmic microtubules are compartmentalized and distinct throughout the entire cell cycle (Jaspersen and Winey, 2004; Kilmartin, 2014). Because the purified spindle pole bodies were allowed to adhere nonspecifically to the coverslip, we did not know what orientation the spindle pole bodies favored, or whether we were studying microtubules emanating from the nuclear face, the cytoplasmic face, or a combination of both. To answer this question, we purified spindle pole bodies from cells expressing Spc72 tagged with an auxin inducible degron (AID). Spc72 is the linker protein that localizes the cytoplasmic γ-tubulin small complex to the outer plaque of the spindle pole body (Knop and Schiebel, 1998; Souès and Adams, 1998; Usui *et al.*, 2003). . Spc72-depleted spindle pole bodies were purified and microtubule attachments were measured by laser trap. The rate of nucleation was similar to that seen with wild type spindle pole bodies and the rupture force was not significantly different from wild type spindle pole bodies (42.8 pN ± 2.8 pN) (Figure 5.3 and Tables 5.4 and 5.9). Because the rate of nucleation did not change and the mean rupture force did not change with the depletion of Spc72, we believed that the majority of microtubules that we observed were emanating from the nuclear face of the spindle pole body.

The C-terminus of Spc110 and calmodulin directly contribute to spindle pole body structural integrity

Spc110-407 encodes a C-terminal truncation of Spc110, which results in an absence of calmodulin in the core of the spindle pole body (Geiser *et al.*, 1993). Aside from suppression of a *cmd1-1* phenotype, *spc110-407* cells do not exhibit any notable phenotypic changes. However, preliminary studies suggest that this mutation is synthetic lethal with *dam1-765*, a mutation at the

kinetochore identified in a synthetic lethal screen with *spc110-226* due to increases in stress at the spindle pole body (Shimogawa *et al.*, 2006). While the localization of calmodulin is required at the spindle pole body, the role that calmodulin plays at the spindle pole body is not yet understood. It is possible that the lack of calmodulin localization in Spc110-407 spindle pole bodies may compromise the mechanical integrity of the spindle pole body. In support of this hypothesis, microtubules nucleated off of Spc110-407 spindle pole bodies showed a statistically significant reduction in rupture force (25.8 pN ± 2.3 pN) (Figure 5.4 and Table 5.5). In fact, Spc110-407 spindle pole bodies had the weakest mean rupture force of all mutants tested, approaching the strength of a kinetochore attachment to microtubules.

Temperature sensitive mutations in Spc110 weaken spindle pole body integrity and microtubule attachments

Spc110 links the γ-tubulin small complex to the inner plaque of the spindle pole body. The essential role of Spc110 in attaching the nuclear microtubules to the core of the spindle pole body has made it the subject of several mutagenesis studies. Because our evidence suggests that we are measuring the rupture force of nuclear microtubules, we purified spindle pole bodies expressing one of two previously characterized temperature sensitive mutations in Spc110. *Spc110-221* cells have an N-terminal mutant of Spc110 that has been shown to induce a Mad1-dependent mitotic arrest at the restrictive temperature. The mutations have been shown to also affect the interaction between Spc110 and the γ-tubulin small complex (Sundberg and Davis, 1997; Nguyen *et al.*, 1998). The temperature sensitive allele *spc110-226* encodes a C-terminal mutant of Spc110 in which the inner plaque delaminates from the spindle pole body at the restrictive temperature (Sundberg and Davis, 1997; Yoder *et al.*, 2005). These phenotypes

apparently result from mechanical failure of the spindle pole bodies to sustain the high tensile forces that are presumably exerted on them during mitosis (Shimogawa *et al.*, 2006).

Spindle pole bodies were purified from strains expressing the mutant Spc110 and grown at the permissive temperature of 25°C. Microtubules nucleated off of Spc110-221 and Spc110-226 spindle pole bodies showed statistically significant reductions in attachment strengths (36.9 pN ± 1.6 pN and 34.6 pN ± 1.9 pN, respectively) (Figure 5.5 and Tables 5.6, 5.7, and 5.9). The histograms of rupture force distributions for these two mutants were bimodal. The stronger peak for both mutants were approximately 45 pN, while the weaker peaks were around 20 pN. The bimodality was more pronounced in the Spc110-226 mutant, which also exhibits a more pronounced and irreversible phenotype *in vivo*.

We hypothesized that the bimodality was due to incomplete penetrance of the temperature-sensitive mutation in cells grown at permissive temperature. To test this hypothesis we purified SPBs from cells grown at the restrictive temperature of 37°C. By western blot analysis, Spc110-226 spindle pole bodies lacked Spc110, and by DIC, little to no nucleation was observed for these spindle pole bodies. We posit that these spindle pole bodies were so weak that they were delaminated during the purification process. Spc110-221 spindle pole bodies at the restrictive temperature did nucleate, and were shown to be even weaker than Spc110-221 spindle pole bodies at the permissive temperature (mean rupture force 27.5 pN ± 2.9 pN). In support of our hypothesis, the bimodality observed in Spc110-221 rupture forces measured at the permissive temperature was absent in rupture forces measured at the restrictive temperature (Figure 5.6 and Table 5.8).

Discussion

Laser trapping experiments have been adapted for the application of force to a single microtubule nucleated from a purified spindle pole body. This has enabled the first measurements of forces sustained by the centrosome. We have shown that a wild type spindle pole body can withstand forces twice that of a kinetochore. We have also measured the strength of spindle pole bodies expressing mutants of Spc110, all three of which significantly reduced the force at which the microtubule was pulled from the spindle pole body.

We showed that localization of calmodulin to the spindle pole body directly contributes to the mechanical strength of the spindle pole body. We know that calmodulin acts at the spindle pole body in a manner independent of its calcium binding properties (Geiser *et al.*, 1991; Brockerhoff and Davis, 1992) and that the calmodulin binding site within the spindle pole body localizes to the C-terminus of Spc110 (Geiser *et al.*, 1993; Stirling *et al.*, 1994). FRET data and computational modeling of spindle pole body organization have localized calmodulin to the central plaque of the spindle pole body, in close proximity to Spc29, Spc42, and Spc110 (Muller *et al.*, 2005). Because calmodulin is embedded in the core of the spindle pole body organization, we hypothesized that calmodulin contributed to the structural integrity of the spindle pole body. The *in vitro* rupture force experiments afforded the first opportunity to test this hypothesis. The statistically significant decrease in rupture forces withstood by spindle pole bodies lacking calmodulin strongly suggested that calmodulin plays a structural role in the core of the spindle pole body.

We also showed that mutations in either the N-terminus or C-terminus of Spc110 weaken the attachment strength of the microtubule to the spindle pole body. N-terminal mutations in Spc110, as seen in *spc110-221*, disrupt the interface between the γ-tubulin small complex and

Spc110 (Sundberg and Davis, 1997; Nguyen *et al.*, 1998) and induce a mitotic arrest at the restrictive temperature. Based on the *in vivo* phenotype, we hypothesized that the N-terminal interface of Spc110 would be significantly weaker when tested *in vitro* with our rupture force experiment. With the C-terminal mutations, *spc110-226, in vivo* evidence suggested weakening of the Spc110 C-terminal interfaces with the other spindle pole components of the central plaque (Sundberg and Davis, 1997; Yoder *et al.*, 2005). For both of these temperature sensitive mutations, we saw a statistically significant decrease in mean rupture force compared to wild type spindle pole bodies. While the *in vitro* measurements support the *in vivo* phenotypes, we don't yet have the resolution *in vitro* to definitively determine which molecular interface within the spindle pole body is rupturing.

The experiments presented here did not differentiate among different rupture interfaces within the spindle pole body. The mutations in Spc110 were localized to either the N- or C-terminus, presumably weakening the molecular interactions at the nearest terminus. At this point, we cannot determine whether the type of molecular interface that ruptures affects the magnitude of the rupture forces we have measured in this study, but it presents an interesting question for further studies. Where does the spindle pole body-microtubule attachment fail? Future experiments plan to address this question through simultaneous laser trap and TIRF imaging. Labeling either the γ-tubulin small complex or Spc110 with GFP will tell us which proteins are associated with the microtubule when it is pulled from the spindle pole body. Microtubules will be captured by the laser trap as before, but the rupture would simultaneously be monitored by TIRF microscopy to determine if GFP fluorescence is associated with the end of the rupture microtubule.

As a first step in the measurement of forces sustained at the centrosome, we have developed an *in vitro* platform to physically characterize purified spindle pole bodies. Analysis of the mutant spindle pole bodies showed a shift in rupture force towards kinetochore-like strengths. We propose that during mitosis, the spindle is undergoing a tug-of-war. With wild type spindle pole bodies, the spindle pole is twice as strong as kinetochores. However, our observations showed that spindle pole body-microtubule interaction strength is sensitive to specific perturbations in the composition of the spindle pole body. As the mutant spindle pole bodies shift towards kinetochore-like strengths, it is more likely that the kinetochore would win the tug-of-war, pulling the microtubule from the spindle pole body and arresting the cell at metaphase. This suggests that weakening spindle pole body-microtubule attachments disrupts the balance of forces across the spindle, thereby delaying or even preventing anaphase.

Acknowledgements

Erik Yusko and Krishna Sarangapani from Chip Asbury's lab were instrumental in development of the assay, data collection, and analysis. Yi Deng assisted with the simultaneous DIC and TIRF imaging.

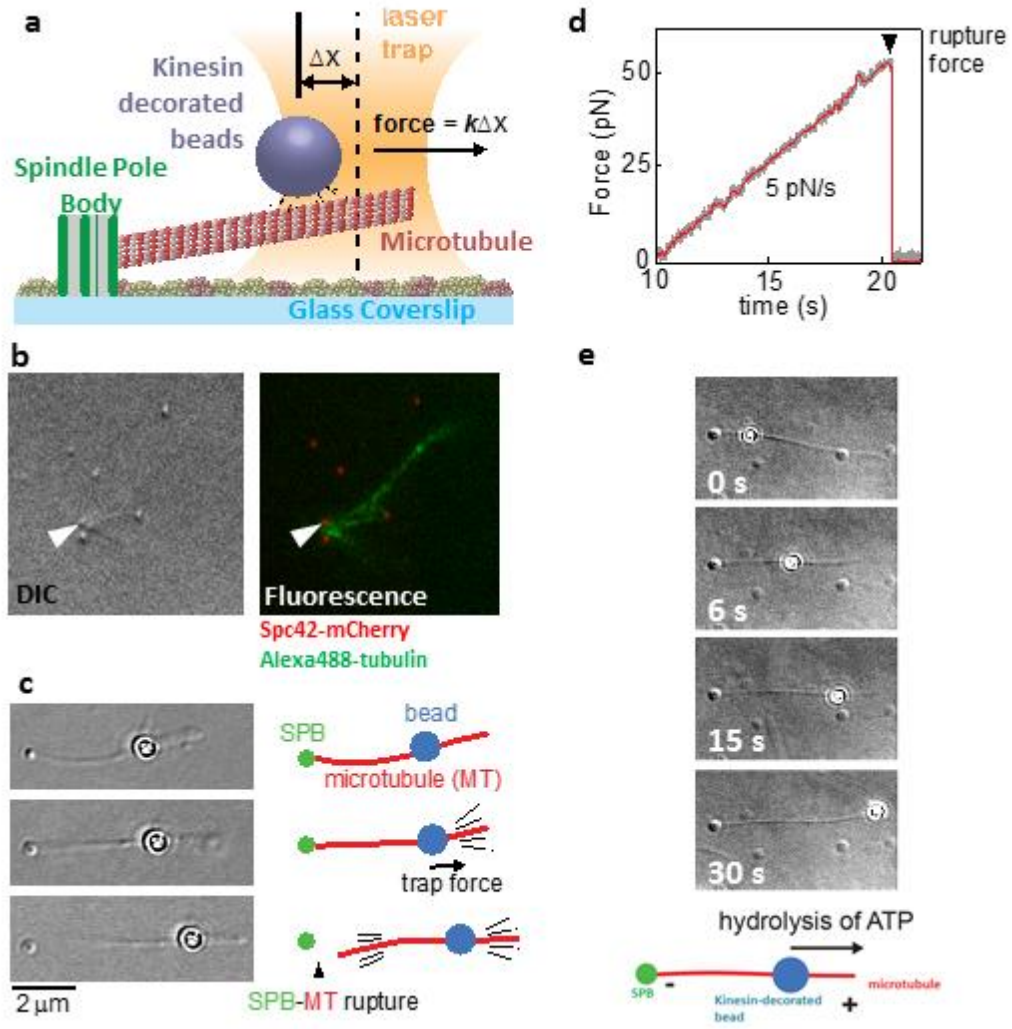

Figure 5.1. The laser trap rupture force assay applies force to a single microtubule nucleated off of a spindle pole body.
a. Schematic of laser trap assay. Spindle pole bodies nonspecifically adhere to a glass coverslip. Microtubules are nucleated off of the spindle pole bodies and kinesin decorated beads bind to the microtubules. The laser trap captures the bead and exerts a force on the spindle pole body-microtubule attachment. b. Simultaneous differential interference contrast (DIC) and total internal reflection fluorescence (TIRF) microscopy. Spindle pole bodies, labeled with Spc42-mCherry and tubulin was labeled with Alexa488 dye. c. Example of a spindle pole body-microtubule attachment rupture. For the rupture force experiment, a kinesin-decorated bead bound to a nucleated microtubule was captured by the laser trap and a force was applied along the length of the microtubule and away from the spindle pole body. The force was then ramped at 5 pN/s until the spindle pole body-microtubule interface ruptured, as observed by DIC. d. Example of a rupture force trace. Force is ramped at 5 pN/s until the attachment ruptures. e. Microtubules exhibit the correct polarity for nucleation off of spindle pole bodies. Kinesin decorated beads walk toward the plus end of the microtubule with the addition of ATP.

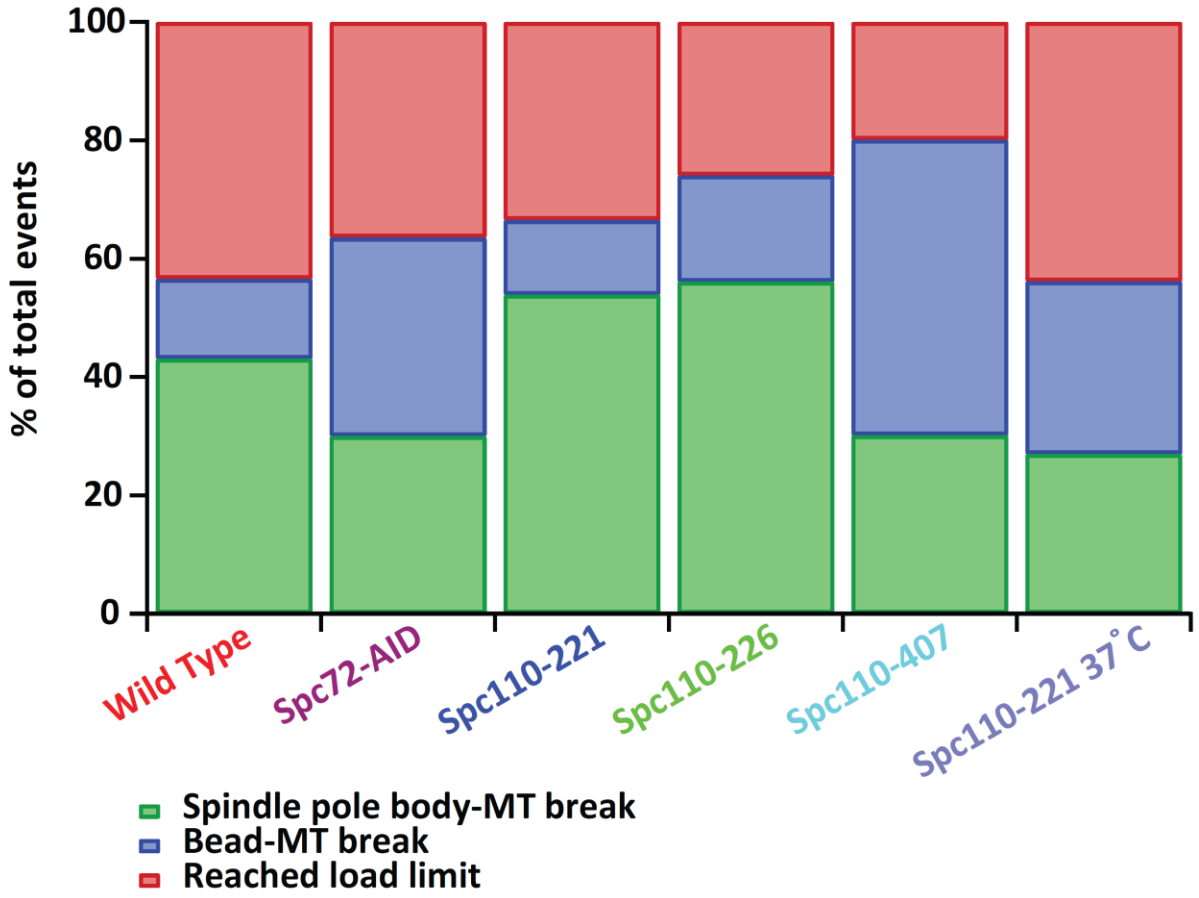

Figure 5.2. Distribution of rupture force events.
Rupture force experiments could end with three different outcomes: the microtubule (MT) could break from the spindle pole body, the bead could break from the microtubule, or the load limit of the trap could be exceeded. These three outcomes were tracked for each spindle pole body type and is presented as percentages.

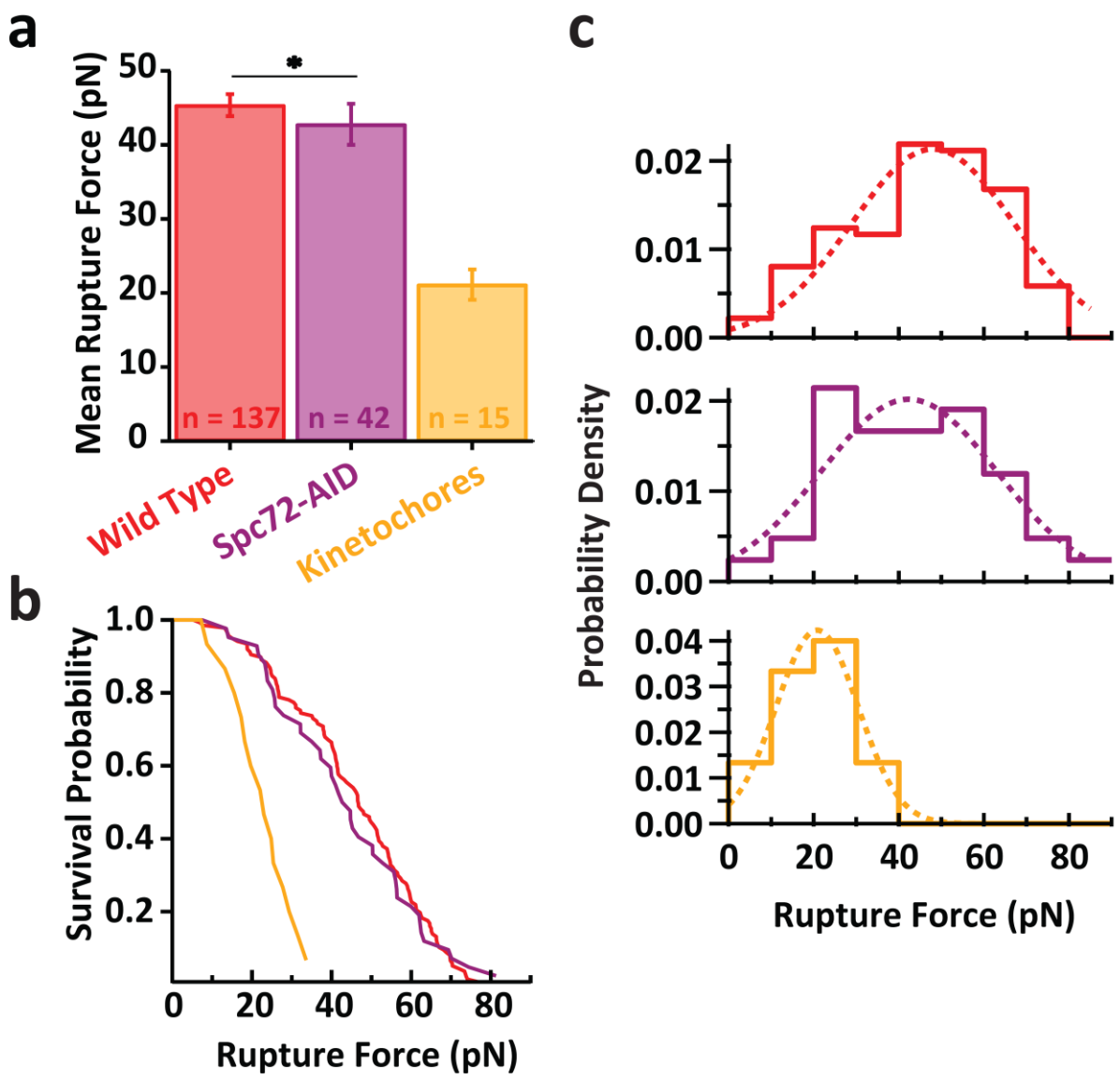

Figure 5.3. Attachment of nuclear microtubules from wild type spindle pole bodies is stronger than kinetochore attachment to microtubules.
a. Mean rupture force ± sem. * p = 0.403 b. Distribution of rupture force values. c. Normalized histograms of rupture force values.

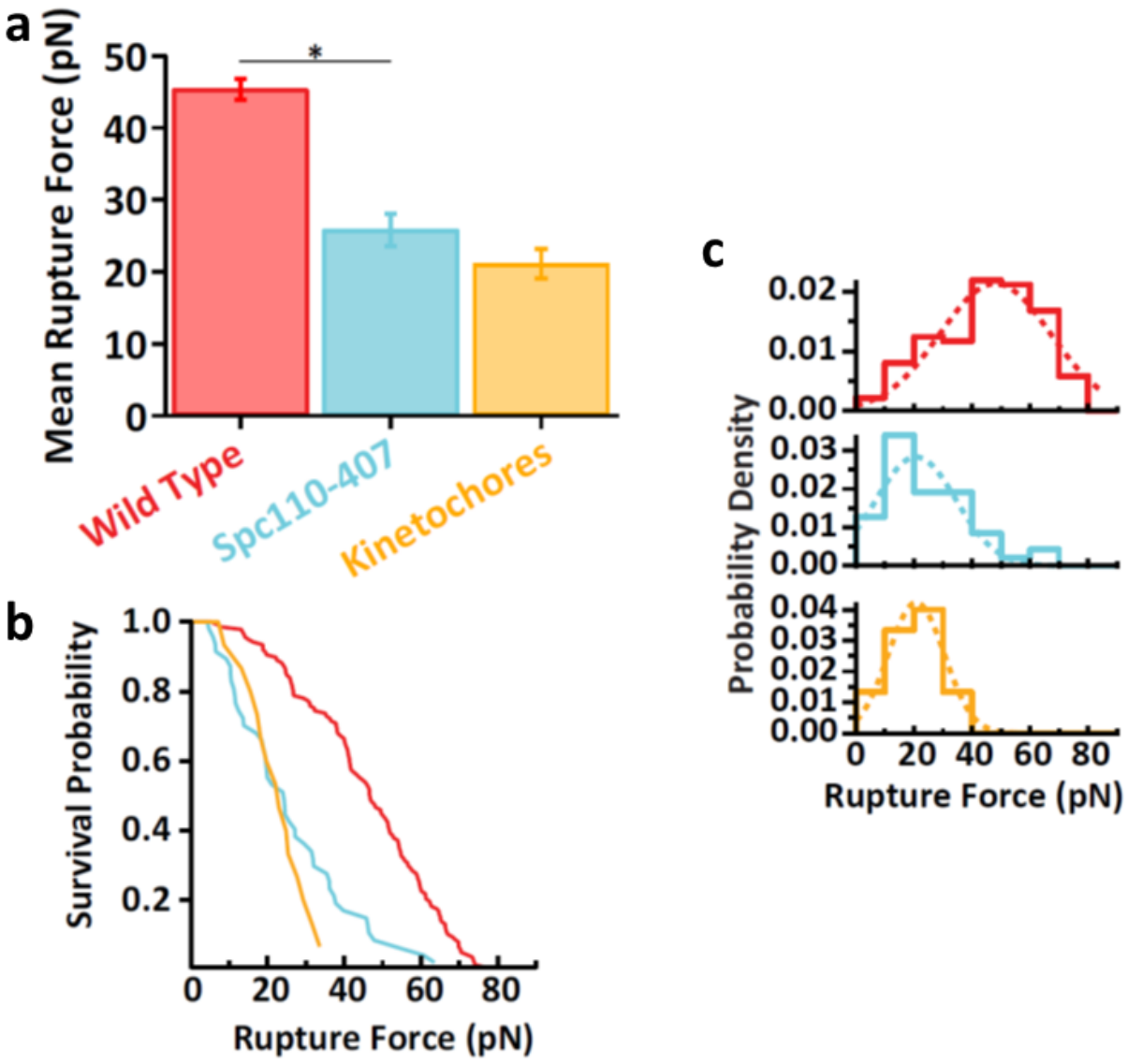

Figure 5.4. The C-terminus of Spc110 and calmodulin directly contribute to spindle pole body structural integrity.
a. Mean rupture force ± sem. * $p = 3.0 \times 10^{-11}$ b. Distribution of rupture force values. c. Normalized histograms of rupture force values.

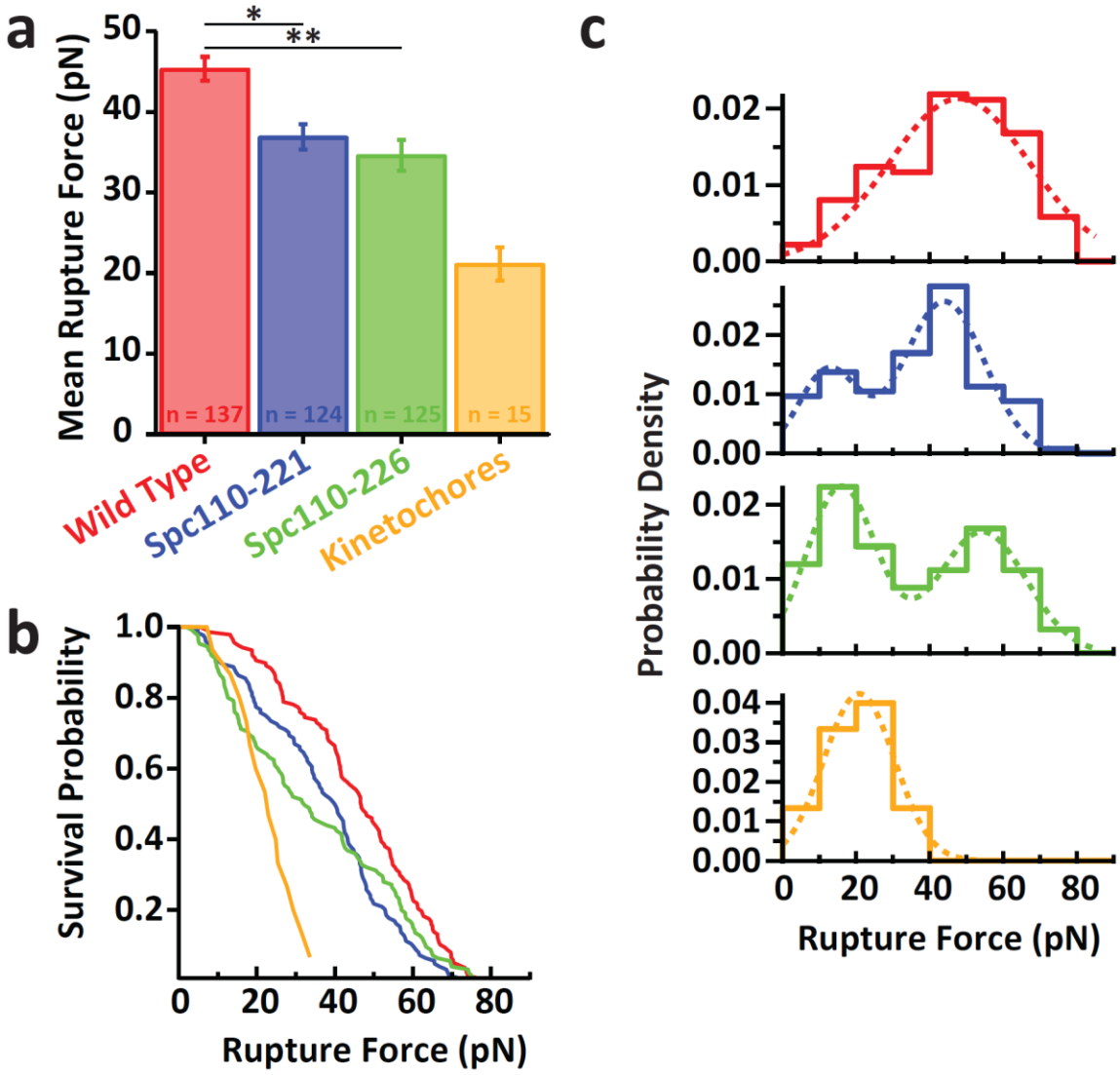

Figure 5.5. Temperature sensitive mutants of Spc110 result in weakened spindle pole body-microtubule attachments.
a. Mean rupture force ± sem. * p = 0.0001, ** p = 9.9 x $^{10\text{-}6}$ b. Distribution of rupture force values. c. Normalized histograms of rupture force values.

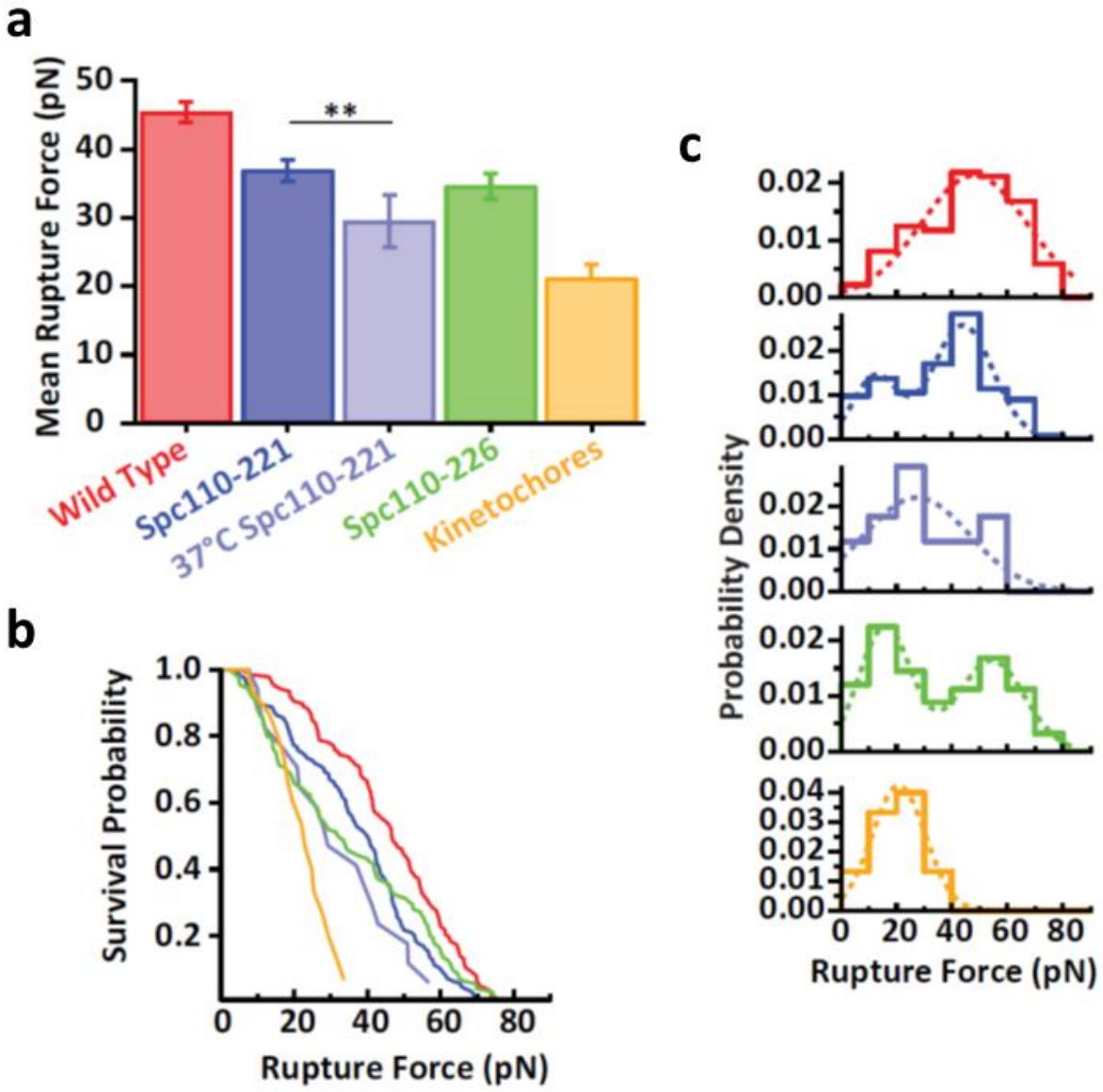

Figure 5.6. Spc110-221 spindle pole bodies harvested at the restrictive temperature do not exhibit a bimodality in rupture force distributions and are weaker than spindle pole bodies at the permissive temperature

a. Mean rupture force ± sem. ** p = 0.0142 b. Distribution of rupture force values. c. Normalized histograms of rupture force values.

Table 5.1. Strains used in this study.

Strain	Genotype	Reference
W303	*ade2-1oc can1-100 his3-11, 15 leu2-3,112 trp1-1 ura3-1*	
BGY72-8A	*MATa SPC42-mCherry::hphMX SPC97-TAP::kanMX*	Fong *et al*., 2016
BGY75-1D	*MATa SPC42-mCherry::hphMX SPC97-TAP::kanMX spc110-226*	Beth Graczyk
BGY82-3A	*MATa SPC42-mCherry::hphMX SPC97-TAP::kanMX spc110-221*	Beth Graczyk
KFY304-2D	*MATa SPC42-mCherry::hphMX SPC97-TAP::kanMX spc110-407*	This study
KFY329-24B	*MATα ade3Δ-100 ura3-1::pADH1-OsTIR1-9myc::URA3 SPC42-mCherry::hphMX SPC72-V5-AID::kanMX SPC97-TAP::kanMX*	This study
KGY315	*MATa/MATα ade2-1oc/ade2-1oc ADE3/ade3Δ-100 can1-100/can1-100 CYH2s/cyh2r his3-11,15/his3-11,15 leu2-3,112/leu2-3,112 trp1-1/trp1-1 ura3-1/ura3-1*	Greenland *et al*., 2010

Table 5.2. Rupture force measurements for wild type spindle pole bodies (pN).

Spindle pole-MT break	Bead-MT break	Reached load limit
54.31	48.21	74.93
26.40	29.57	68.72
56.52	71.10	61.37
65.34	28.20	60.93
59.44	48.24	61.92
46.25	18.91	55.55
25.79	49.43	61.18
24.06	43.85	69.42
69.84	28.97	61.30
73.62	61.51	59.50
68.86	30.22	56.65
54.73	33.57	67.14
59.02	44.41	72.35
38.09	37.85	72.15
69.77	23.71	69.33
41.69	22.02	73.99
25.04	25.37	65.19
51.87	49.51	55.85
49.51	20.69	49.77
39.10	36.77	62.27
40.77	61.41	59.84
51.33	34.99	65.35
57.30	36.95	71.98
51.43	40.26	66.36
65.02	63.26	65.34
66.99	21.59	74.84
69.74	29.94	70.43
35.28	20.60	72.90
26.13	15.45	72.00
44.55	18.67	70.15
73.39	26.96	55.21
53.92	24.15	68.76
14.14	26.35	77.71
41.15	15.37	58.57
64.14	60.08	70.04
13.51	42.98	80.65

52.85	47.79	67.40
59.71	25.35	67.35
49.92	48.12	62.37
58.67	33.37	66.95
40.23	17.95	74.95
6.90	52.49	71.32
31.00	40.80	75.15
32.16		54.64
40.06		74.33
46.55		67.55
41.35		73.98
24.71		62.96
46.54		67.77
66.30		77.87
26.73		68.87
59.87		70.36
74.11		70.98
55.38		71.34
35.04		63.78
47.94		71.80
54.24		68.45
18.76		66.34
66.45		73.13
26.47		66.05
62.70		71.44
22.22		62.84
71.94		71.76
39.97		68.59
42.27		72.26
68.15		77.35
55.78		68.05
36.51		72.03
41.01		72.35
18.83		70.15
46.52		72.02
7.74		62.86
26.00		71.61
76.77		70.98
51.75		71.97
54.79		66.17

40.48		69.85
62.43		68.03
32.25		69.60
43.14		76.25
41.57		71.44
24.50		69.32
57.70		57.88
29.23		68.30
61.09		72.23
31.00		67.50
59.60		68.21
16.31		61.67
5.21		62.57
18.79		67.13
38.11		59.75
26.77		63.84
64.69		75.54
15.11		72.96
54.09		52.31
56.64		56.74
26.65		63.52
38.35		74.19
45.86		54.85
70.35		78.00
62.23		73.13
51.54		60.39
36.23		71.42
50.49		69.24
73.82		68.67
23.56		62.53
47.26		54.38
66.65		65.47
30.49		77.55
59.15		85.36
48.12		65.71
46.79		67.04
65.07		61.55
54.56		65.87
46.72		74.03
70.30		72.25

	19.72		66.53
	22.35		70.18
	49.47		58.64
	60.08		66.21
	37.87		46.14
	40.93		83.03
	64.64		39.23
	50.94		65.04
	13.88		78.11
	19.49		70.49
	66.31		76.11
	13.17		72.24
	24.76		68.19
	45.37		71.62
	52.54		70.69
	41.36		72.25
	37.88		68.54
	61.21		60.48
	61.28		77.74
	41.53		71.11
	43.74		61.43
			58.96
Mean	**45.36**	**36.21**	**67.59**
σ	17.37	14.53	7.11
s.e.m	1.48	2.22	0.61
n	137	43	138

Table 5.3. Rupture force measurements for kinetochores (pN).

	Bead-MT Break
	22.96
	29.33
	15.52
	8.67
	7.18
	17.27
	24.82
	31.54
	27.73
	19.67
	25.36
	18.17
	33.61
	13.18
	22.04
Mean	**21.14**
σ	7.93
s.e.m	2.05
n	15

Table 5.4. Rupture force measurements for Spc72-AID spindle pole bodies (pN).

Spindle pole-MT break	Bead-MT break	Reached load limit
59.93	38.94	37.13
25.87	31.07	55.55
44.75	25.12	56.07
34.97	34.33	61.70
56.34	21.10	61.08
74.47	28.04	57.27
81.31	42.79	55.75
62.24	48.26	64.75
42.66	40.75	44.86
14.06	39.98	41.69
27.92	57.27	65.28
21.62	51.46	57.66
7.47	19.35	72.91
25.15	31.31	48.03
41.76	69.53	34.00
23.61	16.87	38.67
69.34	17.28	43.58
61.97	21.99	53.04
37.32	48.72	79.09
32.21	6.56	62.06
37.08	21.52	75.75
21.22	56.96	68.02
39.98	18.96	82.25
62.50	19.62	66.93
46.72	35.46	81.35
39.75	44.97	65.64
55.62	17.57	49.27
23.23	51.28	47.02
63.23	34.41	66.50
56.43	36.72	48.20
25.66	59.93	54.36
40.97	40.76	51.27
52.82	8.04	54.53
32.15	21.51	55.98
50.32	16.39	46.50
13.53	28.69	61.12

	23.87	48.25	57.66
	70.14	11.30	57.68
	56.08	13.37	50.65
	44.70	32.75	64.51
	45.24	14.11	69.30
	50.26	41.75	57.14
		14.46	57.55
		34.37	60.74
		50.81	61.75
		54.06	50.80
		37.58	35.95
			56.47
			59.52
			62.40
			66.55
Mean	**42.77**	**33.11**	**57.52**
σ	17.92	15.49	11.06
s.e.m	2.77	2.26	1.55
n	42	47	51

Table 5.5. Rupture force measurements for Spc110-407 spindle pole bodies (pN).

Spindle pole-MT break	Bead-MT break	Reached load limit
23.96	28.28	58.47
46.14	36.29	55.30
10.35	48.65	61.95
27.12	45.63	58.65
32.01	44.83	62.67
11.17	45.58	57.45
63.50	33.80	70.73
47.79	32.94	63.11
10.32	43.85	73.97
24.30	43.55	47.48
31.47	37.44	43.39
54.02	43.36	60.35
31.82	20.62	70.76
21.14	21.29	61.52
13.61	36.06	60.78
60.56	38.80	58.62
11.66	25.96	62.60
19.76	14.13	59.18
46.38	10.59	42.35
36.14	14.56	45.61
18.88	31.95	63.58
4.77	22.88	79.73
39.77	30.40	54.85
6.47	13.62	61.53
45.78	47.46	65.41
5.77	32.44	65.34
36.09	36.92	58.65
37.30	22.12	66.28
37.77	19.55	55.97
27.20	13.12	55.34
24.48	55.77	58.88
13.81	39.48	
24.54	16.09	
6.38	23.93	
19.35	19.45	
11.48	43.37	

19.93	41.65	
25.64	22.40	
9.23	22.92	
10.52	56.91	
12.46	15.27	
35.42	70.89	
17.00	47.65	
29.58	10.82	
19.54	39.75	
18.48	21.97	
4.27	30.00	
	25.41	
	39.68	
	58.98	
	17.17	
	19.93	
	15.01	
	23.74	
	24.22	
	18.74	
	32.60	
	27.46	
	33.68	
	20.24	
	25.50	
	17.26	
	10.46	
	6.97	
	63.78	
	60.18	
	44.33	
	12.53	
	42.01	
	25.41	
	13.01	
	11.28	
	53.09	
	39.92	
	40.79	
	71.22	

		50.03	
		37.07	
Mean	**25.22**	**32.01**	**60.02**
σ	15.13	15.21	8.19
s.e.m	2.21	1.72	1.47
n	47	78	31

Table 5.6. Rupture force measurements for Spc110-221 spindle pole bodies at the permissive temperature (pN).

Spindle pole-MT break	Bead-MT break	Reached load limit
18.3	41.35	73.06
30.98	29.68	53.40
32.83	32.08	69.35
13.97	45.58	70.08
25.12	60.33	48.35
36.07	51.86	74.59
11.05	51.25	56.89
9.11	64.24	78.04
18.76	58.12	71.06
9.44	57.98	78.06
36.64	48.13	70.11
35.92	31.36	68.24
9.36	46.46	70.63
42.95	48.24	65.42
36.78	35.50	63.72
59.5	44.37	68.14
52.99	48.57	68.66
7.66	55.91	72.95
42.38	33.22	72.68
29.5	60.22	76.99
42.25	36.61	67.50
46.67	47.76	61.09
53.8	44.22	59.43
47.54	38.93	65.17
49.13	27.32	73.96
45.75	38.40	52.43
34.11	23.25	68.84
22.18	40.27	61.93
17.93	51.73	62.13
57.68		66.17
6.85		61.69
19.63		73.22
46.31		57.60
42.17		62.31
4.8		75.27
7.69		55.72

44.98		67.98
6.33		70.32
28.18		68.48
20.87		64.67
61.42		62.07
25.7		63.07
48.02		78.37
52.84		65.04
47.23		72.15
27.31		63.85
41.1		67.75
18.12		64.30
44.75		51.52
40.31		67.52
2.59		42.08
52.05		62.37
32.33		57.76
49.07		48.50
10.28		69.95
47.85		67.18
68.56		72.55
63.24		70.79
32.94		73.00
55.73		64.77
20.89		63.66
44.08		67.87
18.7		70.67
14.69		65.41
39.29		69.42
15.27		68.06
31.04		69.16
49.93		60.52
14.34		61.66
49.66		62.72
68.9		62.17
40.62		69.89
22.99		61.81
60.72		64.56
43.5		63.49
34.22		57.74

53.12		51.70
40.7		
46.4		
23.57		
48.6		
34.14		
19.13		
19.28		
46.96		
29.44		
56.66		
43.22		
42.1		
33.53		
58.01		
65.42		
46.69		
69.21		
6.76		
61.7		
31.94		
39.91		
46.79		
66.8		
34.6		
4.79		
71.62		
48.04		
65.55		
19.72		
35.32		
55.29		
17.45		
58.17		
56.8		
8.52		
38.63		
60.19		
43.32		
46.24		

	29.61		
	34.70		
	42.54		
	28.22		
	17.01		
	37.56		
	56.92		
	41.63		
Mean	**36.91**	**44.58**	**65.47**
σ	17.42	10.78	7.24
s.e.m	1.56	2.00	0.83
n	124	29	77

Table 5.7. Rupture force measurements for Spc110-226 spindle pole bodies at the permissive temperature (pN).

Spindle pole-MT break	Bead-MT break	Reached load limit
64.81	58.29	63.3
69.92	63.44	73.96
15.37	50.24	71.21
41.59	52.82	65.17
14.13	59.59	72.72
21.42	64.27	67.33
52.18	22.86	61.29
64.55	64.14	68.24
10	49.19	75.22
3.26	72.39	69.22
59.98	61.56	70.5
9.59	25.34	66.62
26.62	26.15	61.12
45.1	26.54	57.54
7.52	52.89	66.18
62.45	61.85	72.01
1.82	23.90	71.21
14.23	30.03	68.86
55.72	13.36	70.53
42.02	23.55	68.86
43.28	27.32	67.36
57.02	19.43	68.5
39.97	30.96	73
15.74	16.35	68.34
63.1	14.00	70.48
34.12	13.72	66.27
32.24	58.12	70.25
28.38	57.98	68.56
25.72	48.13	75.1
33.44	31.36	58.02
13.95	46.46	68.25
12.01	48.24	78.2
56.5	35.50	74.66
52.41	44.37	77.91
58.02	48.57	68.49
69.49	55.91	71.75

11.56	33.22	76.18
74.3	60.22	68.15
9.73	36.61	70.29
59.32	47.76	68.07
15.13	44.22	76.68
50.47	38.93	76.38
19.6	27.32	73.59
46.62	38.40	70.9
24.66	23.25	68.44
26.36	40.27	79.22
65.06	51.73	75.76
56.44		70.05
62.74		53.32
59.88		53.29
37.78		40.69
31.64		49.43
75.36		67.61
27.1		70.09
23.09		67.21
34.76		71.87
18.01		75.55
28.05		70.63
42.55		60.52
48.29		61.66
15		62.72
17.69		62.17
7.42		69.89
46.1		61.81
22.56		64.56
19.74		63.49
60.42		57.74
19.22		51.70
10.25		
55.58		
4.9		
11.59		
10.61		
25.36		
11.69		
24.43		

9.3		
69.72		
12.18		
58.04		
41.86		
12.56		
15.85		
56.71		
9.37		
74.13		
74.93		
45.6		
26.73		
66.32		
5.01		
63.36		
28.91		
14.25		
60.51		
19.03		
57.04		
52.37		
24.39		
34.06		
4.95		
58.27		
26.73		
5.34		
42.26		
14.12		
4.03		
33.6		
36.26		
31.44		
41.79		
51.1		
12.39		
54.65		
8.18		
42.28		

	34.77		
	51.16		
	10.27		
	28.31		
	16.81		
	27.55		
	6.6		
	24.7		
	9.96		
	45.1		
	39.19		
	30.36		
	50.53		
	5.6		
	27.62		
	62.41		
	25.97		
	5.87		
	20.77		
	53.28		
	54.53		
	46.86		
	8.27		
	55.24		
	11.27		
	15.40		
	40.41		
	29.19		
	61.78		
	20.25		
	51.79		
Mean	**34.01**	**41.29**	**67.59**
σ	20.57	16.20	7.22
s.e.m	1.70	2.36	0.88
n	147	47	68

Table 5.8. Rupture force measurements for Spc110-221 spindle pole bodies at the restrictive temperature (pN).

Spindle pole-MT break	Bead-MT break	Reached load limit
16.91	25.32	57.78
50.92	55.82	67.57
27.91	58.16	73.21
41.17	67.04	79.33
36.94	25.52	60.64
21.32	49.06	63.42
56.81	44.60	78.25
39.00	26.73	59.72
7.52	51.45	68.64
12.12	23.71	82.30
42.92	59.04	64.74
10.52	60.54	58.29
9.99	9.47	71.23
20.84	28.09	80.81
51.15	47.80	58.38
25.93	37.88	72.90
29.22	43.38	54.81
19.74	47.55	63.69
8.42	43.92	59.73
26.16	64.85	67.86
33.55	68.37	72.86
26.00	33.11	66.12
20.93	60.28	66.01
24.86	45.34	60.94
	48.12	64.27
	19.57	64.04
		65.52
		69.5
		63.37
		59.12
		59.48
		65.81
		48.90
		70.42
		75.31
		70.72

			74.77
			76.72
			82.72
Mean	**27.54**	**44.03**	**67.18**
σ	14.08	15.99	7.97
s.e.m	2.87	3.14	1.28
n	24	26	39

Table 5.9. Statistical t-test *p* value comparison by spindle pole body types.
Green numbers are statistically significant and red numbers are not statistically significant. Spc110-226 spindle pole body rupture forces could not be measured when harvested at the restrictive temperature, so *p* values could not be determined.

Spindle Pole Type → ↓	Wild Type	Spc110-221 (Permissive)	Spc110-226 (Permissive)	Spc110-407	Spc72-AID	Spc110-221 (Restrictive)	Spc110-226 (Restrictive)
Wild Type		1.0×10^{-4}	9.9×10^{-6}	3.0×10^{-11}	0.40	4.4×10^{-6}	N/A
Spc110-221 (Permissive)			0.35	7.6×10^{-5}	0.063	0.014	N/A
Spc110-226 (Permissive)				5.7×10^{-3}	0.026	0.12	N/A
Spc110-407					2.8×10^{-6}	0.53	N/A
Spc72-AID						7.0×10^{-4}	N/A
Spc110-221 (Restrictive)							N/A
Spc110-226 (Restrictive)							

Chapter 6
Conclusions and future directions

Regions essential for Spc97 and Spc98 structure and function have been mapped by linker scanning mutagenesis

The γ-tubulin small complex is a heterotetrameric complex that is highly conserved and essential for microtubule nucleation. Cryo-electron microscopy structures of the yeast γ-tubulin small complex and of the γ-tubulin ring complexes from several species (Moritz *et al.*, 1995, 2000; Oegema *et al.*, 1999; Kollman *et al.*, 2008, 2010, 2011, 2015; Choy *et al.*, 2009) have provided strong evidence that the γ-tubulin small complex establishes thirteen-fold symmetry observed in microtubules and serves as a template for nucleation. What is still unknown, however, is how the γ-tubulin small complex is activated for nucleation. In yeast, Spc97 and Spc98 are a part of the heterotetrameric complex, along with two molecules of Tub4. However, we do not know how Spc97 and Spc98 are regulated to facilitate the activation of nucleation. Here, I described a comprehensive mutagenesis approach combining linker scanning mutagenesis with a plasmid shuffle screen in yeast, and high-throughput DNA sequencing to identify regions of Spc97 and Spc98 essential for structure and function. Based on sequencing of the transposition library, I know the screen was comprehensive, making insertions across the entirety of both genes, and affecting 98.3% of codons in *SPC97* and 97.3% of codons in *SPC98.* Lethal mutations identified regions of the two proteins that affected γ-tubulin small complex formation, interaction with Spc110, interaction with Spc72, and localization to the spindle pole body. Identification of three temperature sensitive mutations in the N-terminus of Spc98 with

unique nucleation phenotypes suggest that the N-terminus of Spc98 is a highly tunable region that is integral for correct microtubule nucleation.

Presented here is initial characterization of representative lethal mutations and temperature sensitive mutations. Unfortunately, the mechanisms by which these mutations act have not been explicitly defined by the experiments described here. Future studies will continue to explore these mutations and narrow down the possible causes for the observed phenotypes. Unresolved questions for these mutations include: Do these mutations affect inter-complex interactions or intra-complex interactions? Is the structure of the γ-tubulin small complex or higher-order ring complex locked into a conformation that explains the *in vivo* phenotype? Are the phenotypes of the mutation related to cell cycle checkpoints? Are there changes to absolute protein copy numbers at the spindle pole bodies of cells expressing these mutations? Not only would answers to these questions better define the mechanism of action for the lethal and temperature sensitive mutants specifically, they would also provide insights into microtubule nucleation and its regulation as a whole.

The yeast cell cycle phosphoproteome data set has been amended to include only high confidence phosphorylation sites

With improvements made to spindle pole body purification protocols, we have increased the yield, purity, and reproducibility of spindle pole bodies purified out of *Saccharomyces cerevisiae*. Because spindle pole bodies are now purified out of the well-characterized model organism, genetic tools for cell cycle arrest, introduction of genetic mutations, and inclusion of fluorescent labels have expanded the possibilities of spindle pole body experimentation. In the work presented here, spindle pole bodies were purified out of asynchronous cells, cells arrested

in mitosis by Cdc20 depletion, and, most importantly, cells arrested in G1/S with a Cdc4 temperature sensitive allele. Characterization of the G1/S phosphoproteome resulted in a novel data set that describes the state of spindle pole bodies at a stage of the cell cycle when nucleation is first initiated. These spindle pole bodies were analyzed by high resolution mass spectrometry to identify phosphorylation sites at each cell cycle state with high confidence. This data set was compared to a previously published data set of 298 phosphorylation sites (Keck *et al.*, 2011). Agreement among the data sets, as well as more stringent spectrum quality cutoffs, has narrowed the phosphoproteome to 51 asynchronous sites, 43 mitotic sites, 28 alpha factor arrest sites, and 114 cdc4-1 G1/S sites. This reduced data set highlights the individual sites that would be of highest priority for individual study. This study also examined a few of the high confidence phosphorylation sites identified by mass spectrometry. The mitotic sites for Spc97, Spc98, and Tub4 were mutated individually or in combination to look for changes to mitotic spindle structure. It was observed the mutation of two mitotic sites in Spc97, S208A and S209A, were lethal, while the individual sites were not. It was also observed that several of the mitotic phosphorylation sites in Tub4, including S42D, S444D/Y445F, and Y445F, had measurable effects on tubulin distribution throughout the mitotic spindle.

Future studies would continue to examine the effects of specific phosphorylation sites throughout the cell cycle, in the hopes of drafting a model for how phosphorylation affects the spindle pole body and microtubule nucleation throughout the cell cycle. To better understand how these sites affect the regulation of spindle processes, we can examine how individual sites or group of sites affect spindle pole body biology. Specifically, unique phosphorylation sites on the γ-tubulin small complex from the new *cdc4-1* phosphorylation data set could provide insight into the role phosphorylation signals play at the onset of microtubule nucleation.

There are many outstanding questions in the field of spindle pole body regulation. Analysis of the phosphorylation mutants may address questions regarding spindle pole body organization, kinase involvement in spindle pole body regulation throughout the cell cycle, interactions between proteins of the spindle pole body, and conservation of phosphorylation sites and mechanisms between yeast and higher eukaryotes. With the simplification of spindle pole body purification, it would also be possible to start exploring other post-translational modifications of spindle pole body proteins, including ubiquitination, acetylation, and sumoylation.

Mutations in Spc110 have been shown by biophysical measurement to weaken microtubule attachment to the spindle pole body

The improvements made to spindle pole body purifications also allowed for novel *in vitro* spindle pole body assays. Here we described the first experiments measuring the strength of a microtubule attachment to spindle pole bodies and the integrity of the spindle pole body. Previously published laser trap experimental setups were modified for nucleating microtubules off of spindle pole bodies and applying a force directly to the microtubule (Franck *et al.*, 2010). We determined that microtubules nucleated off of wild type spindle pole bodies can withstand forces of 45.4 ± 1.5 pN before rupturing. The strength of this attachment is much stronger than that of a kinetochore attached to a microtubule, which ruptures at 21.1 ± 2.1 pN. In the Davis lab, three mutants of Spc110 had been characterized *in vivo,* and displayed defects in cell cycle progression and spindle pole body integrity. These Spc110 mutations were introduced into purified spindle pole bodies and rupture forces were measured. It was found that the three mutations weakened the attachment of microtubules to spindle pole bodies to values approaching

kinetochore-like strengths. This led to the hypothesis that spindle pole bodies and kinetochores are locked in a tug-of-war on either side of the microtubule. When the spindle pole body strength is compromised by mutations, the kinetochore will win the tug-of-war, pulling the microtubule from the spindle pole body and arresting the cell in mitosis.

Now that the assay has been developed, there are several questions that can be examined with the laser trap. We do not yet know which interface in the spindle pole body is rupturing. We can tag proteins within the spindle pole body with fluorescent tags and monitor by simultaneous total internal reflection fluorescence (TIRF) during the rupture force experiment to track which molecules are pulled out with the microtubule. Another area that can be addressed by this assay is determining how the force is transmitted through the core of the spindle pole body. Only mutants of Spc110 have been studied, but mutations in Spc29 and Spc42 could be studied to see how mutations in the core affect the integrity and function of the entire spindle pole body. In addition, different types of spindle pole bodies can be purified to determine what effect they have on spindle strength, including cell cycle arrested spindle pole bodies and spindle pole bodies treated with various microtubule or mitotic drugs.

BIBLIOGRAPHY

Adams, I. R., and Kilmartin, J. V (1999). Localization of Core Spindle Pole Body (SPB) Components during SPB Duplication in Saccharomyces cerevisiae. J. Cell Biol. *145*, 809–823.

Akiyoshi, B., Sarangapani, K. K., Powers, A. F., Nelson, C. R., Reichow, S. L., Arellano-Santoyo, H., Gonen, T., Ranish, J. A., Asbury, C. L., and Biggins, S. (2010). Tension directly stabilizes reconstituted kinetochore- microtubule attachments. Nature *468*, 576–579.

Aldaz, H., Rice, L. M., Stearns, T., and Agard, D. A. (2005). Insights into microtubule nucleation from the crystal structure of human γ-tubulin. Nature *435*, 523–527.

Alvarado-Kristensson, M., Rodríguez, M. J., Silió, V., Valpuesta, J. M., and Carrera, A. C. (2009). SADB phosphorylation of gamma-tubulin regulates centrosome duplication. Nat. Cell Biol. *11*, 1081–1092.

Asbury, C. L., Fehr, A. N., and Block, S. M. (2003). Kinesin moves by an asymmetric hand-over-hand mechanism. Science *302*, 2130–2134.

Bähler, J., Wu, J.-Q., Longtine, M. S., Shah, N. G., McKenzie, A., Steever, A. B., Wach, A., Philippsen, P., and Pringle, J. R. (1998). Heterologous modules for efficient and versatile PCR-based gene targeting in Schizosaccharomyces pombe. Yeast *14*, 943–951.

Basto, R., and Pines, J. (2007). The Centrosome Opens the Way to Mitosis. Dev. Cell *12*, 475–477.

Bayley, P. M., Butler, F. M. M., and Manser, E. J. (1986). Control of nucleation in microtubule self-assembly. Fed. Eur. Biochem. Soc. *205*, 230–234.

Bechstedt, S., and Brouhard, G. J. (2012). Doublecortin Recognizes the 13-Protofilament Microtubule Cooperatively and Tracks Microtubule Ends. Dev. Cell *23*, 181–192.

Bender, A., and Pringle, J. R. (1991). Use of a screen for synthetic lethal and multicopy suppressee mutants to identify two new genes involved in morphogenesis in Saccharomyces cerevisiae. Mol. Cell. Biol. *11*, 1295–1305.

Biggins, S. (2013). The composition, functions, and regulation of the budding yeast kinetochore. Genetics *194*, 817–846.

Blondel, M., Galan, J. M., Chi, Y., Lafourcade, C., Longaretti, C., Deshaies, R. J., and Peter, M. (2000). Nuclear-specific degradation of Far1 is controlled by the localization of the F-box protein Cdc4. EMBO J. *19*, 6085–6097.

Booth, D. G., Cheeseman, L. P., Prior, I. A., and Royle, S. J. (2013). Studying kinetochore-fiber

ultrastructure using correlative light-electron microscopy. Methods Cell Biol. *115*, 327–342.

Bornens, M. (1973). Letter: Action of heparin on nuclei: solubilization of chromatin enabling the isolation of nuclear membranes. Nature *244*, 28–30.

Brockerhoff, S. E., and Davis, T. N. (1992). Calmodulin Concentrates at Regions of Cell Growth in Saccharomyces cerevisiae. J. Cell Biol. *118*, 619–629.

Bullitt, E., Rout, M. P., Kilmartin, J. V, and Akey, C. W. (1997). The yeast spindle pole body is assembled around a central crystal of Spc42p. Cell *89*, 1077–1086.

Burke, D. J., Dawson, D., and Stearns, T. (2000). Methods in Yeast Genetics: A Cold Spring Harbor Laboratory Course Manual.

Burns, S., Avena, J. S., Unruh, J. R., Yu, Z., Smith, S. E., Slaughter, B. D., Winey, M., and Jaspersen, S. L. (2015). Structured illumination with particle averaging reveals novel roles for yeast centrosome components during duplication. Elife *4*, 4:e08586.

Byers, B., and Goetsch, L. (1974). Duplication of Spindle Plaques and Integration of the Yeast Cell Cycle. Cold Spring Harb. Symp. Quant. Biol. *38*, 123–131.

Byers, B., and Goetsch, L. (1975). Behavior of spindles and spindles plaques in the cell cyle and conjugation of saccharomyces cerevisiae. J. Bacteriol. *124*, 511–523.

Byers, B., Shriver, K., and Goetsch, L. (1978). The role of spindle pole bodies and modified microtubule ends in the initiation of microtubule assembly in Saccharomyces cerevisiae. J. Cell Sci. *30*, 331–352.

Casenghi, M., Barr, F. A., and Nigg, E. A. (2005). Phosphorylation of Nlp by Plk1 negatively regulates its dynein-dynactin-dependent targeting to the centrosome. J. Cell Sci. *118*, 5101–5108.

Castillo, A. R., Meehl, J. B., Morgan, G., Schutz-Geschwender, A., and Winey, M. (2002). The yeast protein kinase Mps1p is required for assembly of the integral spindle pole body component Spc42p. J. Cell Biol. *156*, 453–465.

Castoldi, M., and Popov, A. V. (2003). Purification of brain tubulin through two cycles of polymerization- depolymerization in a high-molarity buffer. Protein Expr. Purif. *32*, 83–88.

Cha, H., Hancock, C., Dangi, S., Maiguel, D., Carrier, F., and Shapiro, P. (2004). Phosphorylation regulates nucleophosmin targeting to the centrosome during mitosis as detected by cross-reactive phosphorylation-specific MKK1/MKK2 antibodies. Biochem. J. *378*, 857–865.

Chambers, M. C. *et al.* (2012). A cross-platform toolkit for mass spectrometry and proteomics.

Nat. Biotechnol. *30*, 918–920.

Chi, Y. H., and Jeang, K. T. (2007). Aneuploidy and cancer. J. Cell. Biochem. *102*, 531–538.

Choy, R. M., Kollman, J. M., Zelter, A., Davis, T. N., and Agard, D. A. (2009). Localization and orientation of the γ-Tubulin Small Complex components using protein tags as labels for single particle EM. J. Struct. Biol. *168*, 571–574.

Cross, R. a., and McAinsh, A. (2014). Prime movers: the mechanochemistry of mitotic kinesins. Nat. Rev. Mol. Cell Biol. *15*, 257–271.

Deshaies, R. J., and Ferrell Jr., J. E. (2001). Multisite Phosphorylation and the Countdown to S Phase. Cell *107*, 819–822.

Donaldson, A. D., and Kilmartin, J. V (1996). Spc42p: a phosphorylated component of the S. cerevisiae spindle pole body (SPB) with an essential function during SPB duplication. J. Cell Biol. *132*, 887–901.

Dumont, S., and Mitchison, T. J. (2009). Force and Length in the Mitotic Spindle. Curr. Biol. *19*, R749–R761.

Duncker, B. P., Pasero, P., Braguglia, D., Heun, P., Weinreich, M., and Gasser, S. M. (1999). Cyclin B-Cdk1 kinase stimulates ORC- and Cdc6-independent steps of semiconservative plasmid replication in yeast nuclear extracts. Mol. Cell. Biol. *19*, 1226–1241.

Dutertre, S. *et al.* (2004). Phosphorylation of CDC25B by Aurora-A at the centrosome contributes to the G2-M transition. J. Cell Sci. *117*, 2523–2531.

Eng, J. K., Hoopmann, M. R., Jahan, T. A., Egertson, J. D., Noble, W. S., and MacCoss, M. J. (2015). A Deeper Look into Comet—Implementation and Features. J. Am. Soc. Mass Spectrom. *26*, 1865–1874.

Eng, J. K., Jahan, T. A., and Hoopmann, M. R. (2013). Comet: An open-source MS/MS sequence database search tool. Proteomics *13*, 22–24.

Erickson, H. P. (2000). Gamma-tubulin nucleation: template or protofilament? Nat. Cell Biol. *2*, E93–E96.

Evans, L., Mitchison, T., and Kirschner, M. (1985). Influence of the centrosome on the structure of nucleated microtubules. J. Cell Biol. *100*, 1185–1191.

Flemming, W. (1882). Zellsubstanz, kern und zelltheilung, Leipzig: Verlag Vogel.

Fong, K.K., Graczyk, B., and Davis, T.N. (*In press*). Purification of fluorescently labeled Saccharomyces cerevisiae Spindle Pole Bodies. *The Mitotic Spindle: Methods and Protocols*. Humana Press.

Franck, A. D., Powers, A. F., Gestaut, D. R., Davis, T. N., and Asbury, C. L. (2010). Direct physical study of kinetochore–microtubule interactions by reconstitution and interrogation with an optical force clamp. Methods *51*, 242–250.

Friedman, D. B. *et al.* (2001). Yeast Mps1p Phosphorylates the Spindle Pole Component Spc110p in the N-terminal Domain. J. Biol. Chem. *276*, 17958–17967.

Friedman, D. B., Sundberg, H. A., Huang, E. Y., and Davis, T. N. (1996). The 110-kD spindle pole body component of Saccharomyces cerevisiae is a phosphoprotein that is modified in a cell cycle-dependent manner. J. Cell Biol. *132*, 903–914.

Gartner, A., Jovanović, A., Jeoung, D. I., Bourlat, S., Cross, F. R., and Ammerer, G. (1998). Pheromone-dependent G1 cell cycle arrest requires Far1 phosphorylation, but may not involve inhibition of Cdc28-Cln2 kinase, in vivo. Mol. Cell. Biol. *18*, 3681–3691.

Geiser, J. R., Sundberg, H. A., Chang, B. H., Muller, E. G. D., and Davis, T. N. (1993). The essential mitotic target of calmodulin is the 110-kilodalton component of the spindle pole body in Saccharomyces cerevisiae. Mol. Cell. Biol. *13*, 7913–7924.

Geiser, J. R., van Tuinen, D., Brockerhoff, S. E., Neff, M. M., and Davis, T. N. (1991). Can calmodulin function without binding calcium? Cell *65*, 949–959.

Geissler, S., Pereira, G., Spang, A., Knop, M., Souès, S., Kilmartin, J., and Schiebel, E. (1996). The spindle pole body component Spc98p interacts with the γ-tubulin-like Tub4p of Saccharomyces cerevisiae at the sites of microtubule attachment. EMBO J. *15*, 3899–3911.

Geyer, E. A., Burns, A., Lalonde, B. A., Ye, X., Piedra, F. A., Huffaker, T. C., and Rice, L. M. (2015). A mutation uncouples the tubulin conformational and GTPase cycles, revealing allosteric control of microtubule dynamics. Elife *4*, 4:e10113.

Gonen, S., Akiyoshi, B., Iadanza, M. G., Shi, D., Duggan, N., Biggins, S., and Gonen, T. (2012). The structure of purified kinetochores reveals multiple microtubule-attachment sites. Nat. Struct. Mol. Biol. *19*, 925–929.

Goshima, G., and Scholey, J. M. (2010). Control of Mitotic Spindle Length. Annu. Rev. Cell Dev. Biol. *26*, 21–57.

Greenland, K. B., Ding, H., Costanzo, M., Boone, C., and Davis, T. N. (2010). Identification of Saccharomyces cerevisiae Spindle Pole Body Remodeling Factors. PLoS One *5*, e15426.

Guillet, V. *et al.* (2011). Crystal structure of γ-tubulin complex protein GCP4 provides insight into microtubule nucleation. Nat. Struct. Mol. Biol. *18*, 915–919.

Haase, S. B., Winey, M., and Reed, S. I. (2001). Multi-step control of spindle pole body duplication by cyclin-dependent kinase. Nat. Cell Biol. *3*, 38–42.

Hach, F., Hormozdiari, F., Alkan, C., Hormozdiari, F., Birol, I., Eichler, E. E., and Sahinalp, S. C. (2010). mrsFAST: a cache-oblivious algorithm for short-read mapping. Nat. Methods *7*, 576–577.

Hanahan, D., and Weinberg, R. A. (2011). Hallmarks of cancer: The next generation. Cell *144*, 646–674.

van Heesbeen, R. G. H. P., Tanenbaum, M. E., and Medema, R. H. (2014). Balanced activity of three mitotic motors is required for bipolar spindle assembly and chromosome segregation. Cell Rep. *8*, 948–956.

Holland, A. J., and Cleveland, D. W. (2012). Losing balance: the origin and impact of aneuploidy in cancer. EMBO Rep. *13*, 501–514.

Huisman, S. M., Smeets, M. F. M. A., and Segal, M. (2007). Phosphorylation of Spc110p by Cdc28p-Clb5p kinase contributes to correct spindle morphogenesis in S. cerevisiae. J. Cell Sci. *120*, 435–446.

Hyams, J. S., and Borisy, G. G. (1978). Nucleation of microtubules in vitro by isolated spindle pole bodies of the yeast Saccharomyces cerevisiae. J. Cell Biol. *78*, 401–414.

Hyman, A., and Karsenti, E. (1998). The role of nucleation in patterning microtubule networks. J. Cell Sci. *111*, 2077–2083.

Jackson, M. B., and Berkowitz, S. A. (1980). Nucleation and the kinetics of microtubule assembly. Proc. Natl. Acad. Sci. *77*, 7302–7305.

Jacobs, C. W., Adams, A. E. M., Szaniszlo, P. J., and Pringle, J. R. (1988). Functions of microtubules in the Saccharomyces cerevisiae cell cycle. J. Cell Biol. *107*, 1409–1426.

Jaspersen, S. L., and Winey, M. (2004). The Budding Yeast Spindle Pole Body: Structure, Duplication, and Function. Annu. Rev. Cell Dev. Biol. *20*, 1–28.

Jeoung, D. I., Oehlen, L. J., and Cross, F. R. (1998). Cln3-associated kinase activity in Saccharomyces cerevisiae is regulated by the mating factor pathway. Mol. Cell. Biol. *18*, 433–441.

Jiang, N., Wang, X., Jhanwar-Uniyal, M., Darzynkiewicz, Z., and Dai, W. (2006). Polo box domain of Plk3 functions as a centrosome localization signal, overexpression of which causes mitotic arrest, cytokinesis defects, and apoptosis. J. Biol. Chem. *281*, 10577–10582.

Joshi, H. C., Palacios, M. J., McNamara, L., and Cleveland, D. W. (1992). γ-tubulin is a centrosomal protein required for cell cycle-dependent microtubule nucleation. Nature *356*, 80–83.

Jung, M. K., Prigozhina, N., Oakley, C. E., Nogales, E., and Oakley, B. R. (2001). Alanine-

scanning mutagenesis of Aspergillus γ-tubulin yields diverse and novel phenotypes. Mol. Biol. Cell *12*, 2119–2136.

Käll, L., Canterbury, J. D., Weston, J., Noble, W. S., and MacCoss, M. J. (2007). Semi-supervised learning for peptide identification from shotgun proteomics datasets. Nat. Methods *4*, 923–925.

Käll, L., Storey, J. D., MacCoss, M. J., and Noble, W. S. (2008a). Assigning significance to peptides identified by tandem mass spectrometry using decoy databases. J. Proteome Res. *7*, 29–34.

Käll, L., Storey, J. D., and Noble, W. S. (2008b). Non-parametric estimation of posterior error probabilities associated with peptides identified by tandem mass spectrometry. Bioinformatics *24*, 42–48.

Keating, T. J., and Borisy, G. G. (2000). Immunostructural evidence for the template mechanism of microtubule nucleation. Nat. Cell Biol. *2*, 352–357.

Keck, J. M. *et al.* (2011). A Cell Cycle Phosphoproteome of the Yeast Centrosome. Science *332*, 1557–1561.

Kikkawa, M., Ishikawa, T., Nakata, T., Wakabayashi, T., and Hirokawa, N. (1994). Direct visualization of the microtubule lattice seam both in vitro and in vivo. J. Cell Biol. *127*, 1965–1971.

Kilmartin, J. V. (2014). Lessons from yeast : the spindle pole body and the centrosome Lessons from yeast : the spindle pole body and the centrosome. Philos. Trans. R. Soc. Lond. B. Biol. Sci. *369*, 20130456.

Kilmartin, J. V., and Adams, A. E. M. (1984). Structural rearrangements of tubulin and actin during the cell cycle of the yeast Saccharomyces. J. Cell Biol. *98*, 922–933.

Kilmartin, J. V., Dyos, S. L., Kershaw, D., and Finch, J. T. (1993). A spacer protein in the Saccharomyces cerevisiae spindle pole body whose transcription is cell-cycle regulated. J Cell Biol. *123*, 1175–1184.

Kinoshita, K., Noetzel, T. L., Pelletier, L., Mechtler, K., Dreschsel, D. N., Schwager, A., Lee, M., Raff, J. W., and Hyman, A. A. (2005). Aurora A phosphorylation of TACC3/maskin is required for centrosome-dependent microtubule assembly in mitosis. J. Cell Biol. *170*, 1047–1055.

Knop, M., Pereira, G., Geissler, S., Grein, K., and Schiebel, E. (1997). The spindle pole body component Spc97p interacts with the γ-tubulin of Saccharomyces cerevisiae and functions in microtubule organization and spindle pole body duplication. EMBO J. *16*, 1550–1564.

Knop, M., and Schiebel, E. (1997). Spc98p and Spc97p of the yeast γ-tubulin complex mediate

binding to the spindle pole body via their interaction with Spc110p. EMBO J. *16*, 6985–6995.

Knop, M., and Schiebel, E. (1998). Receptors determine the cellular localization of a γ-tubulin complex and thereby the site of microtubule formation. EMBO J. *17*, 3952–3967.

Kollman, J. M. *et al.* (2015). Ring closure activates yeast γTuRC for species-specific microtubule nucleation. Nat. Struct. Mol. Biol. *22*, 132–137.

Kollman, J. M., Merdes, A., Mourey, L., and Agard, D. A. (2011). Microtubule nucleation by γ-tubulin complexes. Nat. Rev. Mol. Cell Biol. *12*, 709–721.

Kollman, J. M., Polka, J. K., Zelter, A., Davis, T. N., and Agard, D. A. (2010). Microtubule nucleating γ-TuSC assembles structures with 13-fold microtubule-like symmetry. Nature *466*, 879–882.

Kollman, J. M., Zelter, A., Muller, E. G. D., Fox, B., Rice, L. M., Davis, T. N., and Agard, D. A. (2008). The structure of the γ-tubulin small complex: implications of its architecture and flexibility for microtubule nucleation. Mol. Biol. Cell *19*, 207–215.

Laan, L., Roth, S., and Dogterom, M. (2012). End-on microtubule-dynein interactions and pulling-based positioning of microtubule organizing centers. Cell Cycle *11*, 3750–3757.

Lange, B. M. H. (2002). Integration of the centrosome in cell cycle control, stress response and signal transduction pathways. Curr. Opin. Cell Biol. *14*, 35–43.

Langford, G. M. (1980). Arrangement of subunits in microtubules with 14 profilaments. J. Cell Biol. *87*, 521–526.

Lin, T., Gombos, L., Neuner, A., Sebastian, D., Olsen, J. V., Hrle, A., Benda, C., and Schiebel, E. (2011). Phosphorylation of the Yeast γ-Tubulin Tub4 Regulates Microtubule Function. PLoS One *6*, e19700.

Liu, D., and Lampson, M. a (2009). Regulation of kinetochore-microtubule attachments by Aurora B kinase. Biochem. Soc. Trans. *37*, 976–980.

Machin, N. A., Lee, J. M., and Barnes, G. (1995). Microtubule stability in budding yeast: characterization and dosage suppression of a benomyl-dependent tubulin mutant. Mol. Biol. Cell *6*, 1241–1259.

Machin, N. A., Lee, J. M., Chamany, K., and Barnes, G. (1996). Dosage suppressors of a benomyl-dependent tubulin mutant: Evidence for a link between microtubule stability and cellular metabolism. Genetics *144*, 1363–1373.

Maddox, P. S., Bloom, K. S., and Salmon, E. D. (2000). The polarity and dynamics of microtubule assembly in the budding yeast Saccharomyces cerevisiae. Nat. Cell Biol. *2*, 36–41.

Marschall, L. G., Jeng, R. L., Mulholland, J., and Stearns, T. (1996). Analysis of Tub4p, a yeast γ-tubulin-like protein: Implications for microtubule-organizing center function. J. Cell Biol. *134*, 443–454.

McEwen, B., and Edelstein, S. J. (1977). Evidence for a mixed lattice in microtubules reassembled in vitro. J. Mol. Biol. *139*, 123–145.

Metoz, F., Arnal, I., and Wade, R. H. (1997). Tomography without tilt: three-dimensional imaging of microtubule/motor complexes. J. Struct. Biol. *118*, 159–168.

Milutinovich, M., Ünal, E., Ward, C., Skibbens, R. V., and Koshland, D. (2007). A Multi-Step Pathway for the Establishment of Sister Chromatid Cohesion. PLoS Genet. *3*, e12.

Mitchison, T., and Kirschner, M. (1984). Dynamic instability of microtubule growth. Nature *312*, 237–242.

Moens, P. B., and Rapport, E. (1971). Spindles, spindle plaques, and meiosis in the yeast Saccharomyces cerevisiae (Hansen). J. Cell Biol. *50*, 344–361.

Moritz, M., Braunfeld, M. B., Guénebaut, V., Heuser, J., and Agard, D. a (2000). Structure of the γ-tubulin ring complex: a template for microtubule nucleation. Nat. Cell Biol. *2*, 365–370.

Moritz, M., Braunfeld, M. B., Sedat, J. W., Alberts, B., and Agard, D. A. (1995). Microtubule nucleation by γ-tubulin-containing rings in the centrosome. Nature *378*, 638–640.

Moritz, M., Zheng, Y., Alberts, B. M., and Oegema, K. (1998). Recruitment of the γ-tubulin ring complex to Drosophila salt-stripped centrosome scaffolds. J. Cell Biol. *142*, 775–786.

Morris, N. R. (2000). Nuclear migration. From fungi to the mammalian brain. J. Cell Biol. *148*, 1097–1101.

Muller, E. G. D., Snydsman, B. E., Novik, I., Hailey, D. W., Gestaut, D. R., Niemann, C. A., O'Toole, E. T., Giddings, T. H., Sundin, B. A., and Davis, T. N. (2005). The organization of the core proteins of the yeast spindle pole body. Mol. Biol. Cell *16*, 3341–3352.

Nguyen, T., Vinh, D. B. N., Crawford, D. K., and Davis, T. N. (1998). A genetic analysis of interactions with Spc110p reveals distinct functions of Spc97p and Spc98p, components of the yeast γ-tubulin complex. Mol. Biol. Cell *9*, 2201–2216.

Nicholas, M. P., Höök, P., Brenner, S., Wynne, C. L., Vallee, R. B., and Gennerich, A. (2015). Control of cytoplasmic dynein force production and processivity by its C-terminal domain. Nat. Commun. *6*, 7206.

Niepel, M., Strambio-de-Castillia, C., Fasolo, J., Chait, B. T., and Rout, M. P. (2005). The nuclear pore complex-associated protein, Mlp2p, binds to the yeast spindle pole body and promotes its efficient assembly. J. Cell Biol. *170*, 225–235.

Nogales, E., and Zhang, R. (2016). Visualizing microtubule structural transitions and interactions with associated proteins. Curr. Opin. Struct. Biol. *37*, 90–96.

O'Toole, E. T., Mastronarde, D. N., Giddings Jr., T. H., Winey, M., Burke, D. J., and McIntosh, J. R. (1997). Three-dimensional analysis and ultrastructural design of mitotic spindles from the cdc20 mutant of Saccharomyces cerevisiae. Mol. Biol. Cell *8*, 1–11.

Oakley, B. R., Oakley, C. E., Yoon, Y., and Jung, M. K. (1990). γ-tubulin is a component of the spindle pole body that is essential for microtubule function in Aspergillus nidulans. Cell *61*, 1289–1301.

Oakley, C. E., and Oakley, B. R. (1989). Identification of gamma-tubulin, a new member of the tubulin superfamily encoded by mipA gene of Aspergillus nidulans. Nature *338*, 662–664.

Oegema, K., Wiese, C., Martin, O. C., Milligan, R. A., Iwamatsu, A., Mitchison, T. J., and Zheng, Y. (1999). Characterization of two related Drosophila γ-tubulin complexes that differ in their ability to nucleate microtubules. J. Cell Biol. *144*, 721–733.

Oliveros, J. C. (2007). VENNY. An interactive tool for comparing lists with Venn Diagrams.

Page, B. D., and Haven, N. (1992). CIK1: a developmentally regulated spindle pole body-associated protein important for microtubule functions in Saccharomyces cerevisiae. Genes Dev. *6*, 1414–1429.

Pajunen, M., Poussu, E., Turakainen, H., and Savilahti, H. (2009). Application of Mu in vitro transposition for high-precision mapping of protein–protein interfaces on a yeast two-hybrid platform. Methods *49*, 255–262.

Pajunen, M., Turakainen, H., Poussu, E., Peranen, J., Vihinen, M., and Savilahti, H. (2007). High-precision mapping of protein protein interfaces: an integrated genetic strategy combining en masse mutagenesis and DNA-level parallel analysis on a yeast two-hybrid platform. Nucleic Acids Res. *35*, e103.

Pereira, G., Knop, M., and Schiebel, E. (1998). Spc98p directs the yeast γ-tubulin complex into the nucleus and is subject to cell cycle-dependent phosphorylation on the nuclear side of the spindle pole body. Mol. Biol. Cell *9*, 775–793.

Peter, M., and Herskowitz, I. (1994). Direct inhibition of the yeast cyclin-dependent kinase Cdc28-Cln by Far1. Science (80-.). *265*, 1228–1231.

Peterson, J. B., and Ris, H. (1976). Electron-microscopic study of the spindle and chromosome movement in the yeast Saccharomyces cerevisiae. J. Cell Sci. *22*, 219–242.

Petyuk, V., McDermott, J., Cook, M., and Sauer, B. (2004). Functional Mapping of Cre Recombinase by Pentapeptide Insertional Mutagenesis. J. Biol. Chem. *279*, 37040–37048.

Pierson, G. B., Burton, P. R., and Himes, R. H. (1978). Alterations in number of protofilaments in microtubules assembled in vitro. J. Cell Biol. *76*, 223–228.

Powers, A. F., Franck, A. D., Gestaut, D. R., Cooper, J., Gracyzk, B., Wei, R. R., Wordeman, L., Davis, T. N., and Asbury, C. L. (2009). The Ndc80 Kinetochore Complex Forms Load-Bearing Attachments to Dynamic Microtubule Tips via Biased Diffusion. Cell *136*, 865–875.

Prein, B., Natter, K., and Kohlwein, S. D. (2000). A novel strategy for constructing N-terminal chromosomal fusions to green fluorescent protein in the yeast Saccharomyces cerevisiae. FEBS Lett. *485*, 29–34.

Rieder, C. L. (1982). The Formation, Structure, and Composition of the Mammalian Kinetochore and Kinetochore Fiber. Int. Rev. Cytol. *79*, 1–58.

Rieder, C. L. (2005). Kinetochore fiber formation in animal somatic cells: Dueling mechanisms come to a draw. Chromosoma *114*, 310–318.

Rieder, C. L., Faruki, S., and Khodjakov, A. (2001). The centrosome in vertebrates: more than a microtubule-organizing center. Trends Cell Biol. *11*, 413–419.

Rout, M. P., and Kilmartin, J. V. (1990). Components of the yeast spindle and spindle pole body. J. Cell Biol. *111*, 1913–1927.

Sarangapani, K. K. *et al.* (2014). Sister kinetochores are mechanically fused during meiosis I in yeast. Science *346*, 248–251.

Sarangapani, K. K., Akiyoshi, B., Duggan, N. M., Biggins, S., and Asbury, C. L. (2013). Phosphoregulation promotes release of kinetochores from dynamic microtubules via multiple mechanisms. Proc. Natl. Acad. Sci. U. S. A. *110*, 7282–7287.

Scheele, R. B., Bergen, L. G., and Borisy, G. G. (1982). Control of the structural fidelity of microtubules by initiation sites. J. Mol. Biol. *154*, 485–500.

Sharma, V., Eng, J. K., Maccoss, M. J., and Riffle, M. (2012). A mass spectrometry proteomics data management platform. Mol. Cell. Proteomics *11*, 824–831.

Shimamoto, Y., Forth, S., and Kapoor, T. M. (2015). Measuring Pushing and Braking Forces Generated by Ensembles of Kinesin-5 Crosslinking Two Microtubules. Dev. Cell *34*, 669–681.

Shimogawa, M. M. *et al.* (2006). Mps1 phosphorylation of Dam1 couples kinetochores to microtubule plus ends at metaphase. Curr. Biol. *16*, 1489–1501.

Shimogawa, M. M., Widlund, P. O., Riffle, M., Ess, M., and Davis, T. N. (2009). Bir1 is required for the tension checkpoint. Mol. Biol. Cell *20*, 915–923.

Sikorski, R. S., and Hieter, P. (1989). A system of shuttle vectors and yeast host strains designed for efficient manipulation of DNA in Saccharomyces cerevisiae. Genetics *122*, 19–27.

Sobel, S. G., and Snyder, M. (1995). A highly divergent γ-tubulin gene is essential for cell growth and proper microtubule organization in Saccharomyces cerevisiae. J. Cell Biol. *131*, 1775–1788.

Souès, S., and Adams, I. R. (1998). SPC72: a spindle pole component required for spindle orientation in the yeast Saccharomyces cerevisiae. J. Cell Sci. *111*, 2809–2818.

Spang, A., Geissler, S., Grein, K., and Schiebel, E. (1996a). γ-Tubulin-like Tub4p of Saccharomyces cerevisiae is associated with the spindle pole body substructures that organize microtubules and is required for mitotic spindle formation. J. Cell Biol. *134*, 429–441.

Spang, A., Grein, K., and Schiebel, E. (1996b). The spacer protein Spc110p targets calmodulin to the central plaque of the yeast spindle pole body. J. Cell Sci. *109*, 2229–2237.

Stearns, T., Evans, L., and Kirschner, M. (1991). γ-tubulin is a highly conserved component of the centrosome. Cell *65*, 825–836.

Stearns, T., Hoyt, M. A., and Botstein, D. (1990). Yeast mutants sensitive to antimicrotubule drugs define three genes that affect microtubule function. Genetics *124*, 251–262.

Stirling, D. A., and Stark, M. J. (1996). The phosphorylation state of the 110 kDa component of the yeast spindle pole body shows cell cycle dependent regulation. Biochem. Biophys. Res. Commun. *222*, 236–242.

Stirling, D. A., Welch, K. A., and Stark, M. J. (1994). Interaction with calmodulin is required for the function of Spc110p, an essential component of the yeast spindle pole body. EMBO J. *13*, 4329–4342.

Sundberg, H. A., and Davis, T. N. (1997). A mutational analysis identifies three functional regions of the spindle pole component Spc110p in Saccharomyces cerevisiae. Mol. Biol. Cell *8*, 2575–2590.

Sundberg, H. A., Goetsch, L., Byers, B., and Davis, T. N. (1996). Role of calmodulin and Spc110p interaction in the proper assembly of spindle pole body compenents. J. Cell Biol. *133*, 111–124.

Tien, J. F., Fong, K. K., Umbreit, N. T., Payen, C., Zelter, A., Asbury, C. L., Dunham, M. J., and Davis, T. N. (2013). Coupling unbiased mutagenesis to high-throughput DNA sequencing uncovers functional domains in the Ndc80 kinetochore protein of Saccharomyces cerevisiae. Genetics *195*, 159–170.

Tien, J. F., Umbreit, N. T., Gestaut, D. R., Franck, A. D., Cooper, J., Wordeman, L., Gonen, T., Asbury, C. L., and Davis, T. N. (2010). Cooperation of the Dam1 and Ndc80 kinetochore

complexes enhances microtubule coupling and is regulated by aurora B. J. Cell Biol. *189*, 713–723.

Tilney, L. G., Bryan, J., Bush, D. J., Fujiwara, K., Mooseker, M. S., Murphy, D. B., and Snyder, D. H. (1973). Microtubules: evidence for 13 protofilaments. J. Cell Biol. *59*, 267–275.

Torres, E. M., Williams, B. R., and Amon, A. (2008). Aneuploidy: Cells losing their balance. Genetics *179*, 737–746.

Umbreit, N. T., and Davis, T. N. (2012). Mitosis puts sisters in a strained relationship : Force generation at the kinetochore. Exp. Cell Res. *318*, 1361–1366.

Umbreit, N. T., Gestaut, D. R., Tien, J. F., Vollmar, B. S., Gonen, T., Asbury, C. L., and Davis, T. N. (2012). The Ndc80 kinetochore complex directly modulates microtubule dynamics. Proc. Natl. Acad. Sci. U. S. A. *109*, 16113–16118.

Usui, T., Maekawa, H., Pereira, G., and Schiebel, E. (2003). The XMAP215 homologue Stu2 at yeast spindle pole bodies regulates microtubule dynamics and anchorage. EMBO J. *22*, 4779–4793.

Vinh, D. B. N., Kern, J. W., Hancock, W. O., Howard, J., and Davis, T. N. (2002). Reconstitution and characterization of budding yeast γ-tubulin complex. Mol. Biol. Cell *13*, 1144–1157.

Vogel, J., Drapkin, B., Oomen, J., Beach, D., Bloom, K., and Snyder, M. (2001). Phosphorylation of γ-tubulin regulates microtubule organization in budding yeast. Dev. Cell *1*, 621–631.

Voter, W. A., and Erickson, H. P. (1984). The Kinetics of Microtubule Assembly. Evidence for a two-stage nucleation mechanism. J. Biol. Chem. *259*, 10430–10438.

Wang, Y., Jin, F., Higgins, R., and McKnight, K. (2014). The current view for the silencing of the spindle assembly checkpoint. Cell Cycle *13*, 1694–1701.

Wieczorek, M., Bechstedt, S., Chaaban, S., and Brouhard, G. J. (2015). Microtubule-associated proteins control the kinetics of microtubule nucleation. Nat. Cell Biol. *17*, 907–918.

Wiese, C., and Zheng, Y. (2000). A new function for the γ-tubulin ring complex as a microtubule minus-end cap. Nat. Cell Biol. *2*, 358–364.

Wigge, P. A., Jensen, O. N., Holmes, S., Souès, S., Mann, M., and Kilmartin, J. V (1998). Analysis of the Saccharomyces spindle pole by matrix-assisted laser desorption/ionization (MALDI) mass spectrometry. J. Cell Biol. *141*, 967–977.

Winey, M., and Bloom, K. (2012). Mitotic Spindle Form and Function. Genetics *190*, 1197–1224.

Winey, M., Goetsch, L., Baum, P., and Byers, B. (1991). MPS1 and MPS2: novel yeast genes defining distinct steps of spindle pole body duplication. J. Cell Biol. *114*, 745–754.

Winey, M., Mamay, C. L., O'Toole, E. T., Mastronarde, D. N., Giddings, T. H., McDonald, K. L., and McIntosh, J. R. (1995). Three-dimensional ultrastructural analysis of the Saccharomyces cerevisiae mitotic spindle. J. Cell Biol. *129*, 1601–1615.

Wittmann, T., Hyman, A. A., and Desai, A. (2001). The spindle: a dynamic assembly of microtubules and motors. Nat. Cell Biol. *3*, E28–E34.

Yoder, T. J., McElwain, M. A., Francis, S. E., Bagley, J., Muller, E. G. D., Pak, B., Toole, E. T. O., Winey, M., Davis, T. N., and O'Toole, E. T. (2005). Analysis of a spindle pole body mutant reveals a defect in biorientation and illuminates spindle forces. Mol. Biol. Cell *16*, 141–152.

Zheng, Y., Wong, M. L., Alberts, B., and Mitchison, T. (1995). Nucleation of microtubule assembly by a γ-tubulin-containing ring complex. Nature *378*, 578–583.